COGGING TORQUE, TORQUE RIPPLE AND RADIAL FORCE ANALYSIS OF PERMANENT MAGNET SYNCHRONOUS MACHINES

A Dissertation

Presented to

The Graduate Faculty of The University of Akron

In Partial Fulfillment

of the Requirements for the Degree

Doctor of Philosophy

Mohammed Rakibul Islam

May, 2009

COGGING TORQUE, TORQUE RIPPLE AND RADIAL FORCE ANALYSIS OF PERMANENT MAGNET SYNCHRONOUS MACHINES

Mohammed Rakibul Islam

Dissertation

Approved:	Accepted:
Advisor Dr. Iqbal Husain	Department Chair Dr. Alexis De Abreu-Garcia
Committee Member Dr. Tom Hartley	Dean of the College Dr. George K. Haritos
Committee Member Dr. Igor Tsukerman	Dean of the Graduate School Dr. George R. Newkome
Committee Member Dr. Graham Kelley	Date
Committee Member Dr. Kevin Kreider	

ABSTRACT

This dissertation presents a methodology for designing low noise small permanent magnet synchronous motor (PMSM) drives by addressing the issues of cogging torque, torque ripple, acoustic noise and vibration. The methodology incorporates several pole shaping and magnet skew schemes in different motor topologies with similar envelop dimensions and output characteristics intended for an automotive application. The developed methodology is verified with finite element analysis (FEA) and experiments.

A comprehensive design methodology has been developed for obtaining the analytical design of the machine for a given set of output characteristics. Using the FEA, the effects of various magnet shapes and skew arrangements on the machine performances (e.g. cogging torque, torque ripple etc.) have been analyzed. The FEA and experimental results show that for certain magnet designs and configurations the skewing does not necessarily reduce the ripple in the electromagnetic torque, but may cause it to increase. An analytical model to predict radial vibration due to magnetic radial pressure on the motor structure has also been developed. This model is used for predicting the noise power level for several motor topologies designed for similar power level applications.

The predicted noise levels are utilized to develop guidelines for selecting motor configurations, internal dimensions and winding types for a low-noise PMSM.

The selection of low-noise PMSM is not a straightforward one; rather it is a compromise between torque harmonics and radial vibration of the machine. Some PMSM configurations with less radial vibration might posses excessive torque ripples and thereby violate other requirements to be less noisy.

Experiments are conducted to record the torque ripple variation for different magnet shapes and skew in order to validate the results of FE models. The experimental results correlated well with the FE computations.

ACKNOWLEDGEMENTS

My sincere gratitude to Dr. Iqbal Husain without whose ardent initiatives, constant compassionate advice and astute guidance this research work would not have materialized. Also I would like to thank all of the Committee Members for their excellent suggestions for making this research a success. The financial support of The University of Akron during my research period is also highly appreciated. The support of TRW Automotive Sterling Heights Division in fabricating the two PMSM designs used in the experiments is highly appreciated.

I would also like to thank my parents, my wife Ayesha, my son Areeb, my lab mates and my brothers and sisters for their invaluable love and encouragement over the years.

TABLE OF CONTENTS

LIST OF TABLES

LIST OF FIGURES

CHAPTER I

INTRODUCTION

Recent developments in rare earth permanent magnet (PM) materials and power electronics have created new opportunities for the design, construction, and application of permanent magnet synchronous motors (PMSMs). The PMSMs are preferred over other motors used for ac servo drives due to their high efficiency, high torque-to-current and torque-to-volume ratios, compact structure, and fast dynamic response. These motors are adopted in several residential and industrial applications. However, many of such applications require minimum torque ripple, and reduced vibration and acoustic noise.

Servo motor technology has moved in recent years from conventional DC or two-phase AC motor drives to new maintenance–free brushless three phase PMSM drives for motor applications where quick response, light weight, and large continuous and peak torques are required. The torque produced by these machines has a pulsating component, which varies as a function of the rotor position, in addition to the dc component. The torque pulsations are known as torque ripple. The shape of the torque waveform, and thus, the frequency content of the waveform are influenced by several factors related to motor design and construction. A consequence of introducing PMs in the rotor is torque pulsations even in the absence of any stator excitation; this torque is known as cogging torque. The harmonics in the BEMF due to design imperfections also introduce torque pulsations. The torque ripple content in PMSMs must be improved through cogging torque and BEMF harmonics reduction for smooth operation of the motor.

The performance of electrical machines can be improved by optimal design and good control techniques. The developments of digital signal processing technology, vector control theory, and numerous other control algorithms have allowed electrical machines to perform at high performance levels through sophisticated control techniques. There is only limited opportunity to improve noise and vibration in low to medium power PMSMs through control techniques. However, the electromagnetic machine design aspects are yet to be fully explored; the scope for improvement is vast when approached from a design perspective.

1.1 Classification of PM Machines

The motors that use magnets to produce air-gap magnetic flux instead of field coils as in DC commutator machines or magnetizing component of stator currents as in induction machines are the permanent magnet machines. Two types of permanent-magnet AC motor drives, namely PMSM drive and PM brushless DC motor (PM BLDC) drive, are available in the drive industry. The DC commutator motors are the third type of PM machines, although these are not used for high performance drives.

PM machines, like any other machine, can be used either as a motor or as a generator. The machine is more commonly used as a motor in a variety of applications.

However, in many of these applications, four-quadrant or two-quadrant operation is often essential to provide regenerative capability for faster response and higher efficiency. The research emphasis in this dissertation will be on PM motors with regenerative capability.

There are several ways of classifying PM motors, such as based on the direction of magnetic field, the position of the rotor relative to the stator, the shape of BEMF and excitation, the arrangement of the PMs in the rotor, and the presence of stator slot. These various types of PM machines will be discussed next.

Based on the excitation current and BEMF wave shapes, PM motors are classified as:

- PM BLDC and
- PMSM.

In PM BLDC, phase currents switch polarity in synchronism with the passage of alternate N and S magnet poles resulting in square wave type excitation. The BEMF, in this case, is usually trapezoidal. On the other hand, PMSM is excited with sinusoidal phase currents and the BEMFs are also sinusoidal. All three phases of a PMSM carry current all the time whereas in PM BLDC only two phases carry current at a given instant.

PM motors also can be classified based on whether or not slots are present in the stator. These are:

- Motors with conventional slotted stators
- Motors with slotless (surface-wound) stators

Slotless motor can achieve zero cogging torque. For the same motor dimensions and magnet materials, the average torque level in a slotless motor is little less than the average torque in a slotted motor.

The PM motors can be divided into two categories based on the direction of the magnetic field:

- Axial flux motor, and
- Radial flux motor.

Axial flux PM motor is an attractive alternative to the cylindrical radial flux motor due to its pancake shape, compact construction, and high power density. These are designed as a PM BLDC motor in many applications. The design is complicated for the axial flux motor due to the presence of two air gaps, high axial attractive forces and changing dimensions with radius.

Again based on the magnet position or rotor construction, there are three types of PMSMs commonly found in the industry:

- Surface mounted permanent magnet (SPM) motor
- Inset permanent magnet motor
- Interior permanent magnet (IPM) motor

From an electromagnetic point of view, the difference between SPM with the other two types is that the synchronous reactances in the direct and quadrature axes (*i.e.* d-and q-

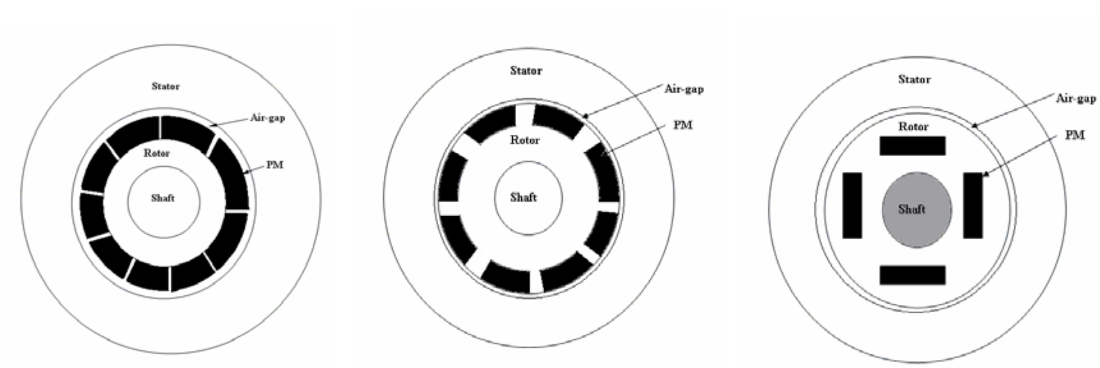

(a) SPM (b) Inset Magnet (c) IPM

Figure 1.1: Three main types of permanent magnet motors.

axes respectively) are practically the same in the first type whereas *q*-axis reactance is higher than *d*-axis reactance in the others. The cross-sectional structures of these three types of PM machines are shown in Fig. 1.1. The structures shown are those of the radial flux topology. The SPM machines can be either sinusoidal or trapezoidal types, while the inset and interior PM machines are usually of sinusoidal types. The focus of this dissertation research is on the sinusoidal type, radial flux SPM motors. The more general term PMSM will be used in reference to these machines in this dissertation.

1.1.1 Common Types of Permanent Magnets

The most suitable magnets for the brushless motors are the ferrites or ceramic magnets, and the high-energy rare-earth and Neodymium-Iron-Boron magnets. All these magnets have straight characteristics throughout the second quadrant, and they are classified as hard magnets because of their high resistance to demagnetization. A typical characteristic curve for permanent magnets is given in Fig. 1.2. Other magnets, particularly Alnico magnets, have a high remnant flux but very low coercive magneto motive force (MMF) and low resistance to demagnetization. These magnets, known as soft PM magnets, have a 'knee' in the second quadrant. In the long history of permanent magnet materials, spanning hundreds or even thousands of years, it is only in the last two decades that truly hard permanent magnet materials have been discovered and perfected. Twenty years ago the 'high coercivity' alloys referred to in the literature was far less resistant to demagnetization than those available today.

The latest addition in permanent magnet industry with improved magnet characteristics is neodymium-iron-boron which has been pioneered by Sumitomo as ‘Neomax’, General Motors as ‘Magnequench’. At room temperature NdFeB has the

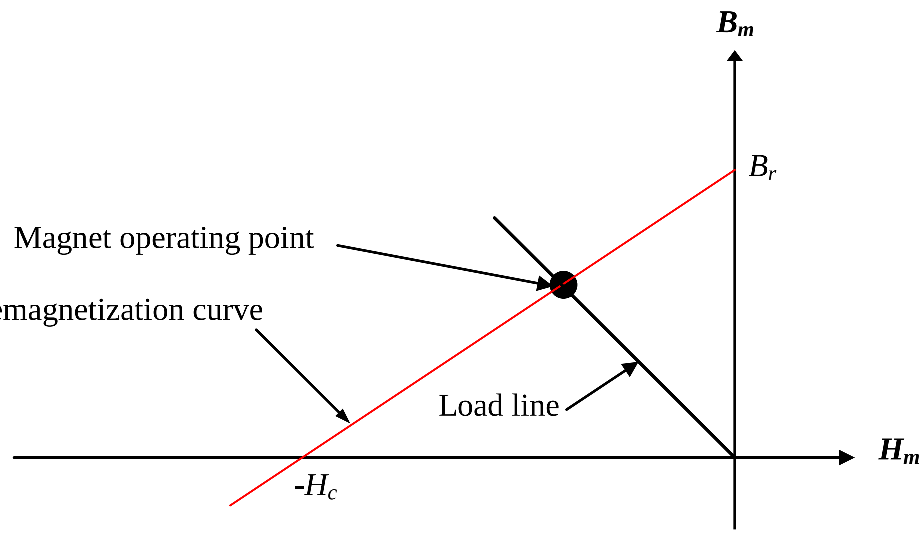

Figure 1.2: Typical characteristic curve for permanent magnets.

highest energy product of all commercially available magnets. The high remanence and coercivity allow marked reduction in motor frame size for the same output compared with motors using ferrite (ceramic) magnets. However, ceramic magnets are considerably cheaper.

For lowest cost, ferrite or ceramic magnets are the universal choice. This class of magnet materials has been steadily improved and is now available with remnant flux density of 0.38 T and almost straight demagnetization characteristic throughout the second quadrant. Since the brushless motor must be low in cost to be competitive in the adjustable-speed market, the use of the highest grade Ferrite magnet in terms of remnant flux density must be employed. In other words, the highest possible flux per pole is the main objective after cost-consideration.

1.2 Advantages of PMSM

The PMSM also known as the sinusoidal brushless DC motor or permanent magnet AC motor originates from the synchronous motor with permanent magnets replacing the field circuit. This modification eliminates the rotor copper loss as well as the need for the maintenance of the field exciting circuit. Thus, a PMSM has high efficiency and an easier to design cooling system. Moreover, the use of rare earth magnet materials increases the flux density in the air gap and accordingly increases the motor power density and torque-to-inertia ratio. In demanding motion control applications, the PMSM can provide fast response, compact motor structure, and high efficiency.

The PMSM is essentially a wound rotor AC synchronous machine with no damper windings. The difference resides in the fact that the rotor excitation is fixed and provided by permanent magnets instead of coming from an external circuit through slip rings and brushes. There are several advantages of PM motors compared to its counterparts:

- Operates at a higher power factor compared to induction motor (IM) due to the absence of magnetizing current.
- Doesn’t require regular brush maintenance like conventional wound rotor synchronous machines.
- Rotor doesn’t require any supply nor does it incur any loss.
- Low noise and vibration than switched reluctance motors (SRM) and IMs.

- Lower rotor inertia and hence fast response.
- Larger energy density and compact structure.

The main disadvantage is the high cost of the permanent magnets, and its sensitivity to temperature and load conditions. However, the cost is coming down due to the abundant supply of rare earth materials in some parts of the world.

1.3 Basic PMSM Operation

The PMSM has a stator with a set of 3-phase sinusoidally distributed copper windings and a rotor with permanent magnets. A sinusoidal magnetic field is generated in the air gap when 3-phase balanced sinusoidal currents are supplied in the 3-phase stator windings. The rotor magnetic field produced by the permanent magnets can be made sinusoidal by shaping the magnets and controlling their magnetizing directions. The electromagnetic torque is generated on the shaft by the interaction of these two magnetic fields created by the stator and the rotor circuits.

In the surface mounted PMSM, the magnets are epoxy-glued or wedge-fixed to the cylindrical rotor. The manufacturing of this kind of a rotor is simple. However, the mechanical strength of the rotor is only as good as that of the epoxy glue. The *d*- and *q*-axes inductances of the surface mounted PMSM are approximately equal. This is because the length of the air gap is equal to that of the magnet, which has a permeability that is approximately the same as that of the air.

In the inset PMSM, the magnets are put into the rotor surface slots that secure the magnet in its location. Interior PMSM has its magnets buried inside the rotor, which is even more secure. The manufacturing process is complicated that makes the interior

PMSM more expensive compared to the other PMSMs. The interior PMSMs can stand small amount of demagnetizing current; this makes the motor suitable for field weakening operation in the high-speed range. The *q*- axis inductance can be much larger than that of the *d*-axis although the length of the air gap is the same. The space occupied by the magnet in the *d*-axis is occupied by iron in the *q*-axis. This means that in addition to the electromagnetic torque (also known as mutual torque), a reluctance torque exists in interior and inset PMSMs.

1.4 Application of PMSMs

PM motors are used in a broad power range of applications from a few mWs to hundreds of kWs. There are also attempts to use PMSMs for high power applications even for those rated over a MW. Thus, PM motors span a wide variety of application fields, from stepper motors for wristwatches through industrial drives for machine tools to large PM synchronous motors for ship propulsion.

In aerospace applications, the PM alternators are in competition with several other brushless synchronous machines, namely the inductor, Lundell, rotating rectifier, and various reluctance configurations. The PM BLDCs are also popular in the computer industry for reduced noise levels, the ability of precise speed and torque control, and flexibility of shape and geometry.

The largest users of PM machines today are by far the automotive industry; PMSMs seem to be the best propulsion motors for electric and hybrid road vehicles. It can be noted that, one rotating machine in passenger cars that is not PM-excited is the alternator. However, PM alternators are used in other automotive applications such as auxiliary power supplies in trucks and off-road vehicles.

The servo types of PM motors are used as variable-speed drives in applications where compact design, high efficiency, high power factor, and low noise are the primary requirements. Possible applications of these motors are in electro-hydraulic and/or electric brakes, power steering, and certain types of valve controls. Low torque ripple levels are required for these applications, since the motors have to work at low speeds with high precision in speed control.

1.5 Scope of PMSM Design

One of the main disadvantages of PM motors is cogging torque due to the interaction of PM and the slotted iron structure of the stator. Cogging or detent torque is the zero average pulsating torque, which adds to the total torque and appears as torque ripple.

The magnetic field distribution within a motor plays a fundamental role in motor performance. In particular, the magnetic field in the air gap and the way it links with the stator coils determine the BEMF and the torque. Secondly, the magnetic field acting within the ferromagnetic portions of the motor determines the amplitude of the air gap flux density. Excessive flux in the ferromagnetic portions saturates the core, increase the BEMF harmonics, and diminish the flux flow across the air gap. This result in an increased torque ripple and decreased average torque. Some applications are sensitive to torque ripple, and may also require quiet operation by the motor. The torque ripple and noise problems can be alleviated by shaping the air gap flux to minimize the BEMF harmonics that will reduce the pulsating torque component.

1.5.1 Noise and Vibration Issues

Vibration is a limited reciprocating particle motion of an elastic body or medium in alternately opposite directions from its equilibrium position when that equilibrium has been disturbed. In order to vibrate, the body or system must have two characteristics: elasticity and mass. The amplitude of vibration is the maximum displacement of a vibrating particle or body from its position of rest.

Sound is defined as vibrations transmitted through an elastic solid, liquid, or gas; sound waves with frequencies in the approximate range of 20 to 20,000 Hz are capable of being detected by human ears. *Noise* is disagreeable or unwanted sound. Distinction can be made between airborne noise and the noise traveling through solid objects. *Airborne noise* is the noise caused by the movement of large volumes of air and the use of high pressure. *Structure-borne* noise is the noise carried by means of vibrations of solid objects. The frequency of interest for vibrations is generally within 1000 Hz, and for noise it is over 1000 Hz.

The acoustic noise in electric motors based on its source can be classified into three categories: aerodynamic, mechanical, and electromagnetic. The aerodynamic noise consists of windage noise due to air turbulence around the rotor and the noise from blowers used for ventilation. Most of the mechanical noise is associated with the bearing assembly of a motor; they may be significant if, for example, the bearing parts are deformed in some manner, or if excessive clearances permit axial travel of the shaft. In addition, inertia forces caused by an unbalanced rotor known as eccentricity can cause mechanical noise. Electromagnetic noise is often the dominant type of noise in modern small motors. Several design related factors like slotting, saturation, eccentricities of shaft, rotor slots, spigots etc. can generate periodic electromagnetic exciting forces within the motor. These exciting forces act on the machine, which is seen as a mechanically passive system capable of vibrating, and generate the vibratory motion.

The noise produced from any or all of the three sources give rise to measurable deformations and vibrations. Part of the energy of the vibration motion within the audible range transforms into sound energy, depending on motor frame’s sound radiation capacity. This sound energy is heard as acoustic noise. A flow diagram showing the process of noise generation in electrical machines is given in Fig. 1.3 [25]. The three noise production mechanisms will be discussed further in section 2.5.

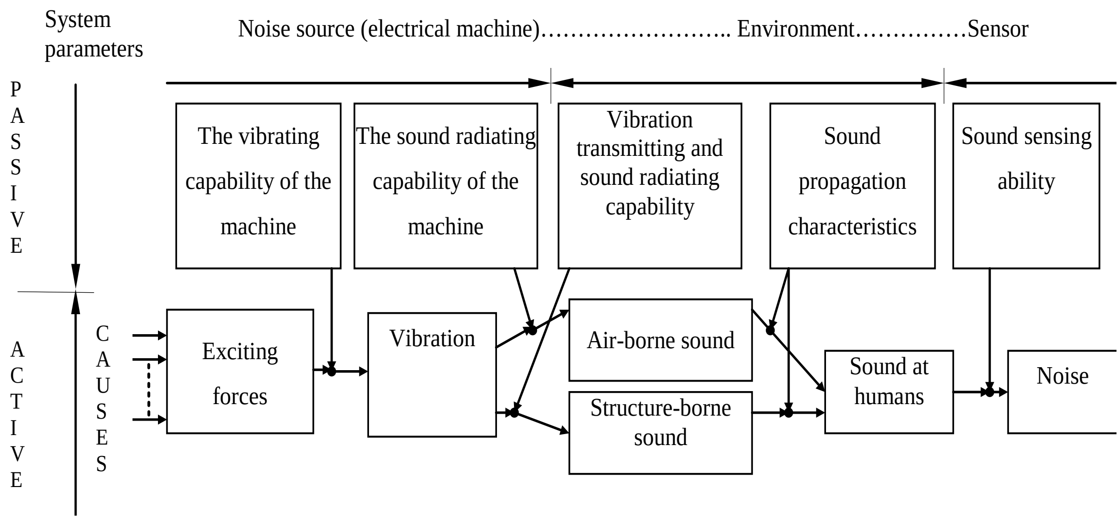

System parameters
Noise source (electrical machine)…………………….. Environment……………Sensor
PASSIVE
ACTIVE
CAUSES
The vibrating capability of the machine
The sound radiating capability of the machine
Vibration transmitting and sound radiating capability
Sound propagation characteristics
Sound sensing ability
Exciting forces
Vibration
Air-borne sound
Structure-borne sound
Sound at humans
Noise

- Constant or average component T_0 , and
- Periodic component $T_r(\theta_e)$, which is a function of time or electrical angle θ_e, superimposed on the constant component.

The periodic component causes the *torque pulsation*, which is also called the *torque ripple*. The torque ripple can be defined as a percentage of the average or RMS torque in the following way:

$$t_r = \frac{T_{r,p-p}}{T_{av}} \times 100\% = \frac{T_{max} - T_{min}}{T_{av}} \times 100\% \qquad \text{or,}$$

$$t_r = \frac{T_{r,p-p}}{T_{rms}} \times 100\% = \frac{T_{max} - T_{min}}{T_{rms}} \times 100\%$$

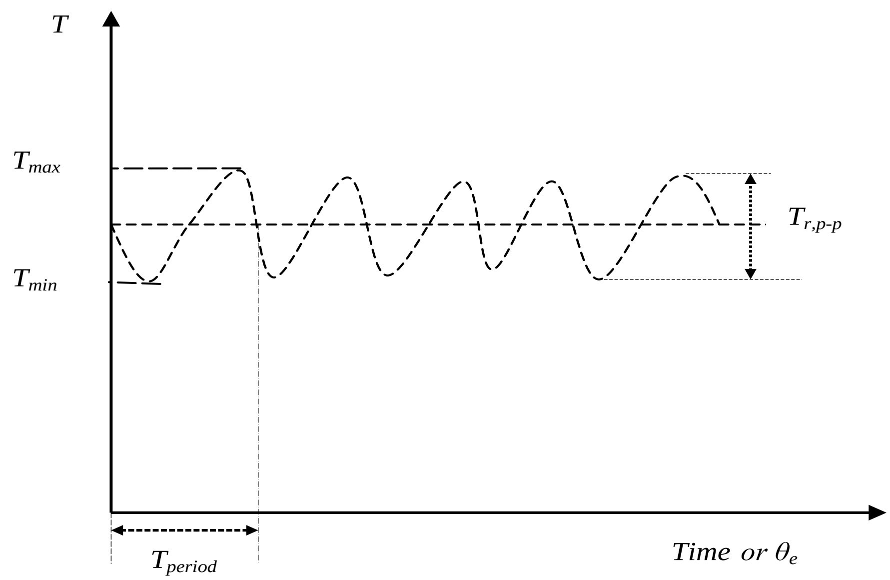

$$T_{av} = \frac{1}{T_{period}} \int_{\theta_e}^{\theta_e + T_{period}} T(\theta_e) d\theta_e \qquad\qquad T_{rms} = \frac{1}{T_{period}} \sqrt{\int_{\theta_e}^{\theta_e + T_{period}} T^2(\theta_e) d\theta_e} \; .$$

The three main contributions of torque ripple in PMSM are from: i) reluctance torque, ii) cogging torque, and iii) mutual torque. The contribution from reluctance torque in surface mounted PMSMs can be ignored since the difference in the *d*- and *q*- axes reactances are negligible. The mutual torque produces torque ripple due to the distortion of the magnetic flux density distribution in the air gap or the distortion in stator current. The interaction between the rotor magnetic flux and variable permeance of the air gap due to the stator slot opening causes the cogging torque.

Researchers have focused on reducing both the mutual torque and the cogging torque to minimize the torque ripple in SPM machines. Some researchers have considered torque ripple problem primarily from a design point of view [1]-[3], while others emphasized on the control aspects [4]-[7].

1.5.3 PMSM Design

One of the main requirements of a high performance AC servomotor is minimum torque ripple. This requires the motor to possess a good BEMF waveform (sinusoidal in case of sine wave motor) and low cogging torque. The next important requirement is low radial forces with no possible unbalances, which depend mainly on the motor configuration and stator winding arrangements. Lower radial forces are essential for reducing noise and vibration.

1.6 Research Objectives

The primary research objective of this dissertation is to develop an understanding of torque ripple and vibrations in various PMSM designs in order to facilitate the design of low noise PMSM drive systems. A detailed outline of achieving this broad objective is given in Fig. 1.5. The specific tasks to be accomplished in this research to fulfill the objective are as follows:

- ✓ Comprehensive design methodology for PMSM.
- ✓ Cogging torque and torque ripple assessment in several PMSM configurations (12-slot/10-pole, 9-slot/6-pole, 12-slot/8-pole, and 27-slot/6-pole machines).
- ✓ Investigations of skew effect on cogging torque and torque ripple in PMSMs with various magnet shapes.
- ✓ Experimental verification of torque ripple test data with FEA results.
- ✓ Analysis of magnetic radial forces in PMSMs.
- ✓ Radial pressure calculation by FEA for different PMSM configurations.
- ✓ Development of an analytical model for calculating radial displacement using radial pressures obtained from FEA.
- ✓ Verification of radial displacement analytical model.

The dissertation addresses the issues of torque ripple, acoustic noise, and vibration in PMSM and develops a methodology for designing low noise small PMSM drives. A detailed analysis of cogging torque, torque ripple, and radial forces has been accomplished in relation to rotor skew. The various contributors to acoustic noise and vibration have been identified and analyzed. Different motor topologies (i.e., motors with different slot/pole combinations) with various magnet designs and similar envelop dimensions and output characteristics (such as rated torque, power, base speed, and physical dimensions) intended for an automotive application have been analyzed in this research.

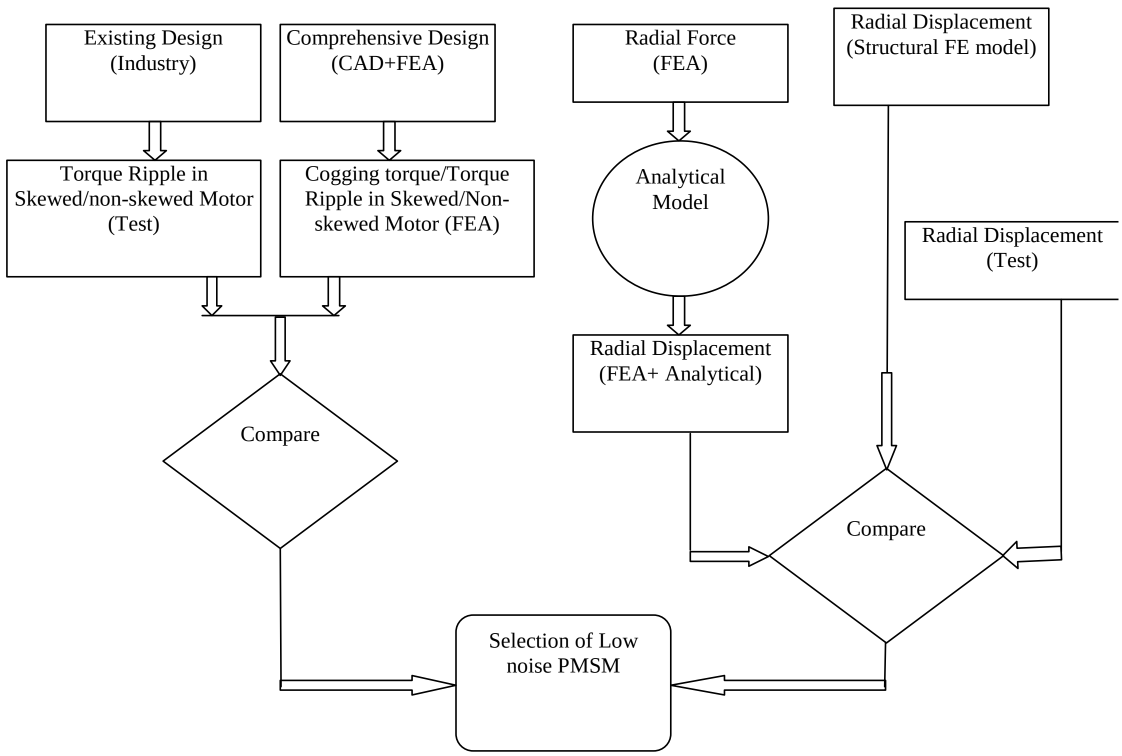

Chapter II begins with the basics of PMSM modeling and operation, and goes further into identifying the dominant sources of noise and vibration in PMSM. The available literature on design and control based methods available for improving torque ripple, noise and vibration in electric machines are reviewed. The primary motivation of this research comes from the need to reduce torque ripple, acoustic noise and vibration in PMSM using design based methods.

Chapter III presents a comprehensive design methodology for PMSMs. The first section describes the development of an algorithm for the design of a PMSM based on a given set of requirements and specifications within certain constraints. The main steps of the design are selection of the motor topology (i.e. slot-pole combination), sizing of the envelop dimension, sizing of rotor dimensions and stator laminations, etc. An outline will be given to select a good PMSM design with smooth running capability and satisfying the torque-speed requirements in the last section of this chapter.

Further refinement of the design is essential since small sized PMSM are more prone to cogging and ripple torque. Chapter IV focuses on explaining the effect of magnet shape variations on the torque waveforms, which lead to torque ripples. The effect of rotor skewing on both cogging torque and torque ripple has been analyzed. The effects of pole shaping and skewing have been studied using the FE analysis. Finally, the chapter provides the experimental results that have been used to validate the analysis.

The PMSM designs for high-performance applications also require low vibration and acoustic noise that originate from the radial pressure on the motor stator. Chapter V discusses the radial forces in the PMSM; an analytical model for predicting radial displacement due to radial forces has been developed. Both analytical model and FEA calculation have been used to validate the results of radial displacement. Finally, prediction of noise from displacement measurement has been documented in this chapter.

Finally, a summary of this dissertation and scopes of future work for PM machines are presented in Chapter VI.

CHAPTER II

PMSM TORQUE RIPPLE, NOISE AND VIBRATION

The goal in this chapter is to familiarize the readers with the torque ripple, noise and vibration in PMSMs. The origins of those issues and their minimization techniques from design perspective will be addressed. An extended literature review on the torque ripple and cogging torque as well as magnetic stress due to periodic excitation forces will also be presented.

2.1 PMSM Structure

PMSMs are synchronous AC machines. The stator of a PMSM usually incorporates a three-phase winding similar to that in a squirrel cage induction machine, but the rotor winding is replaced with permanent magnets. This means that a rotor flux always exists. The magnets can be located on the surface or inside of the rotor.

A machine equipped with surface magnets (Fig. 2.1) has a wide effective air gap because permanent magnet material has almost the same permeability as air. This results in low magnetizing inductance and limited possibilities to affect the machine's electromagnetic state by the stator current. In case of surface mounted magnets, the machine has almost no saliency, although some saliency may exist if the rotor iron saturates. The phase winding arrangement in the stator can be concentrated or distributed. Also, the winding can be single layer or multi-layer.

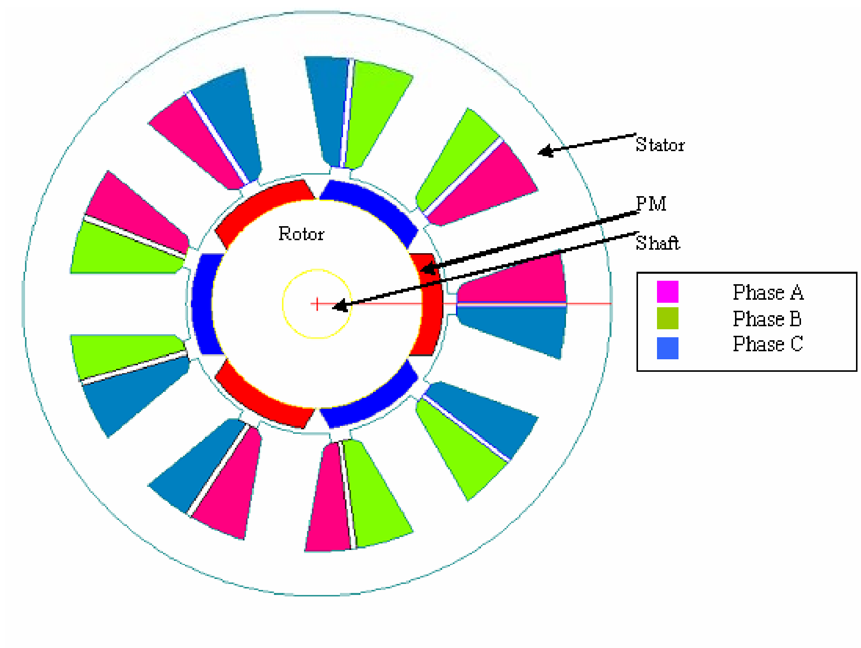

Figure 2.1: Schematic diagram of a 3-phase 9-slot/6-pole PMSM with a 2-layer concentrated winding.

2.2 PMSM Drive System

The phase windings of a PMSM are fed with sinusoidal waveforms shifted by $(360/N_{ph})^0$ from one another, where N_{ph} is the number of stator phases. For a three-phase machine, the three-phase windings with 120^0 space phase shifted are fed by 120^0 time-phase shifted currents to produce a rotating magnetic field. This type of machine is called a *sinewave* motor.

The motor drive structure includes the machine, associated position sensors (if not sensorless operation), power electronics converter and the controller. A typical PMSM motor drive system is shown in Fig. 2.2. Generally, the feedback from the position sensor provides the rotor position information, which is used to appropriately energize the phase currents for machine operation in any of the torque, speed or position controlled modes. Current sensors provide feedback to the controller to reconstruct the three phase currents for current control, which in turn allow torque control. The speed control, if necessary, is accomplished in the outer loop, and position-control, if necessary, is accomplished in yet another outer loop.

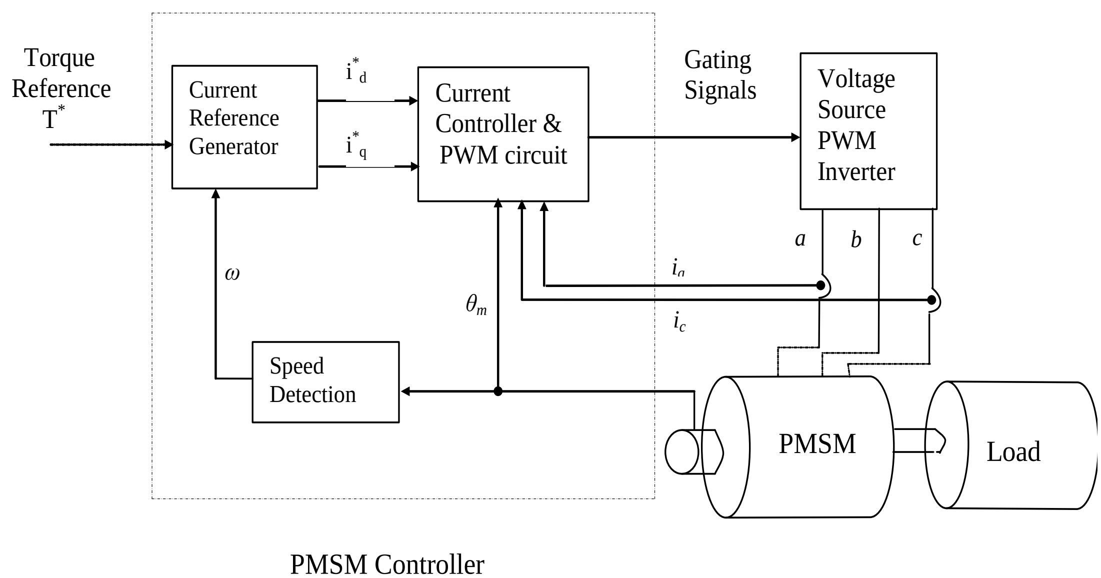

2.3 PMSM *d-q* Model

The electromagnetic analysis of a PMSM is conveniently carried out in a *d-q* rotating reference frame. The *d-q* reference frame variables are obtained from the stationary *abc* reference frame through the Park transformation equation given in (2.1). The Park transformation is a matrix transformation which converts a three phase balanced system into a two-dimensional one. Two possible transformations are commonly used. The first one is α-β and is aligned with the "*a*" phase axis. It is called fixed reference frame. The other case is usually called *d-q* rotor reference frame, and is aligned with the rotating magnetic axis of the rotor.

The Park transformation converts the *abc* system to *dq0* reference frame and *dq0* system to *abc* reference frame. In the *abc* reference frame, three phase voltage, current or flux linkage quantities are represented by f_a, f_b and f_c. The direct and quadrature axes equivalent voltages and currents are represented as f_d and f_q, respectively. The third component in the *d-q* frame is called "*0*" or homopolar component, which is identically zero in balanced three phase systems, and will be omitted later in this chapter. The transformation equations are

$$\begin{bmatrix} f_q \\ f_d \\ f_0 \end{bmatrix} = \frac{2}{3}\begin{bmatrix} \sin(\theta_r) & \sin(\theta_r - 2\pi/3) & \sin(\theta_r + 2\pi/3) \\ \cos(\theta_r) & \cos(\theta_r + 2\pi/3 & \cos(\theta_r + 2\pi/3) \\ 1/2 & 1/2 & 1/2 \end{bmatrix} . \begin{bmatrix} f_a \\ f_b \\ f_c \end{bmatrix}$$

$$\begin{bmatrix} f_a \\ f_b \\ f_c \end{bmatrix} = \begin{bmatrix} \sin(\theta_r) & \cos(\theta_r) & 1 \\ \sin(\theta_r - 2\pi/3) & \cos(\theta_r - 2\pi/3 & 1 \\ \sin(\theta_r + 2\pi/3) & \cos(\theta_r + 2\pi/3) & 1 \end{bmatrix} . \begin{bmatrix} f_q \\ f_d \\ f_0 \end{bmatrix} \tag{2.1}$$

The machine voltage equation in the *abc* reference frame can be expressed in matrix form as

$$\begin{bmatrix} v_a \\ v_b \\ v_c \end{bmatrix} = \begin{bmatrix} R_a & 0 & 0 \\ 0 & R_b & 0 \\ 0 & 0 & R_c \end{bmatrix} \begin{bmatrix} i_a \\ i_b \\ i_c \end{bmatrix} + \frac{d}{dt} \begin{bmatrix} \varphi_a \\ \varphi_b \\ \varphi_c \end{bmatrix} \tag{2.2}$$

where v_a, v_b, and v_c are the machine phase voltages, referenced to the ground, i_a , i_b , and i_c are the machine phase currents, R_a , R_b , and R_c are the machine phase resistances, and φ_a , φ_b , and φ_c are the magnetic flux linkages associated with each phase.

For the PMSM, the synchronously rotating *d*-*q* rotor reference is used. The *abc* and *d*-*q* reference frame directions are given in Fig. 2.3. The *d*-axis represents the rotor magnet flux axis and the *q*-axis is in quadrature to the *d*-axis.

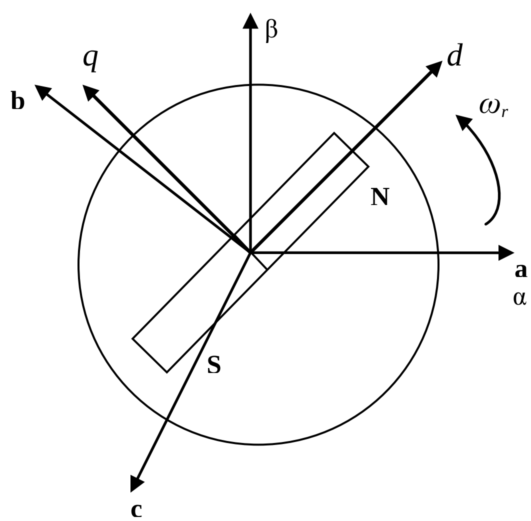

Figure 2.3: PM machine synchronously rotating *d*-*q* reference frame.

The PMSM is represented by the standard *dq* mathematical model as [9]

$$\begin{aligned} v_d &= Ri_d + L_d \frac{di_d}{dt} - pL_q \omega i_q \\ v_q &= Ri_q + L_q \frac{di_q}{dt} + pL_d \omega i_d + k_t \omega \end{aligned} \quad . \tag{2. 3a}$$

The electromagnetic torque is

$$T_m = \tfrac{3}{2}(k_t i_q + p(L_d - L_q) i_q i_d) \quad . \tag{2. 3b}$$

The motor dynamics are given by

$$T_m - T_{load} - T_{fr} = J \frac{d\omega}{dt} \quad . \tag{2.3c}$$

The stator phase voltage and currents are given by

$$v_s = \sqrt{v_d^2 + v_q^2}; \quad i_s = \sqrt{i_d^2 + i_q^2} \quad . \tag{2. 3d}$$

The PMSM drive system model described by the above equations is valid for the ideal case without magnetic saturation. The parameters and variables of the model are listed in the Table 2.1.

Table 2.1: Motor parameters & variables

v_q, i_q	q-axis stator voltage and current	v_d, i_d	d-axis stator voltage and current
R	Stator phase resistance	$v_{s,} i_s$	Stator phase voltage and phase current
L_q	Stator inductance in q axis	L_d	Stator inductance in d axis
k_t	Torque constant	p	Number pairs of poles
ω	Instantaneous rotational speed, ω>Ω	Ω	Rotational speed at a load-torque slope break point
T_m	Motor electromechanical torque	T_{load}	Load torque
T_{fr}	Friction torque	J	Moment of inertia

2.4 Principle of Operation

In a PMSM, the surface magnets are placed as alternate N and S poles. These magnets cause flux in the radial direction to flow through the air gap. Again, mmf generated due to the stator currents crosses the air gap and links the PM flux. The interaction of PM flux and stator mmf causes the rotor to rotate. As the rotor moves the flux linkage varies and induces BEMF in the stator phases. Finally, the interaction between the phase currents and the corresponding phase BEMFs produces the electromagnetic toque.

The stator phases in a PMSM are excited with sinusoidal currents; the phase BEMFs are desired to be sinusoidal through design. The speed variation can be achieved by varying the supply voltage, which is controlled by phase chopping or pulse width modulation (PWM). The PMSM runs under torque limit mode until it reaches its continuous rated speed (also known as base speed or corner speed). This point gives the rated power output. Operating speeds above the base speed is generally obtained by phase

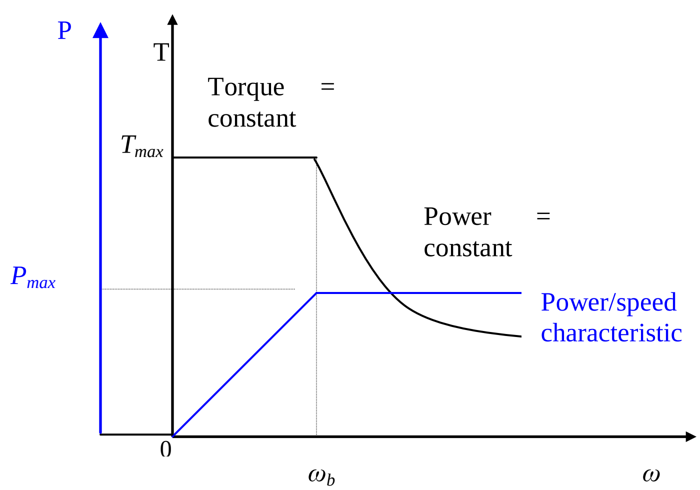

Figure 2.4: Torque/speed and power/speed characteristics of an ideal PMSM.

advancing or field weakening. Field weakening is achieved by supplying negative reactive current. The motor operates under power limit mode with speeds higher than the base speed. The ideal torque/speed characteristic is plotted in Fig. 2.4.

The time variation of electromagnetic torque generated in a PMSM can be obtained as a product of stator currents and BEMFs. The fundamental components produce the continuous component of the torque, while harmonics of different frequency

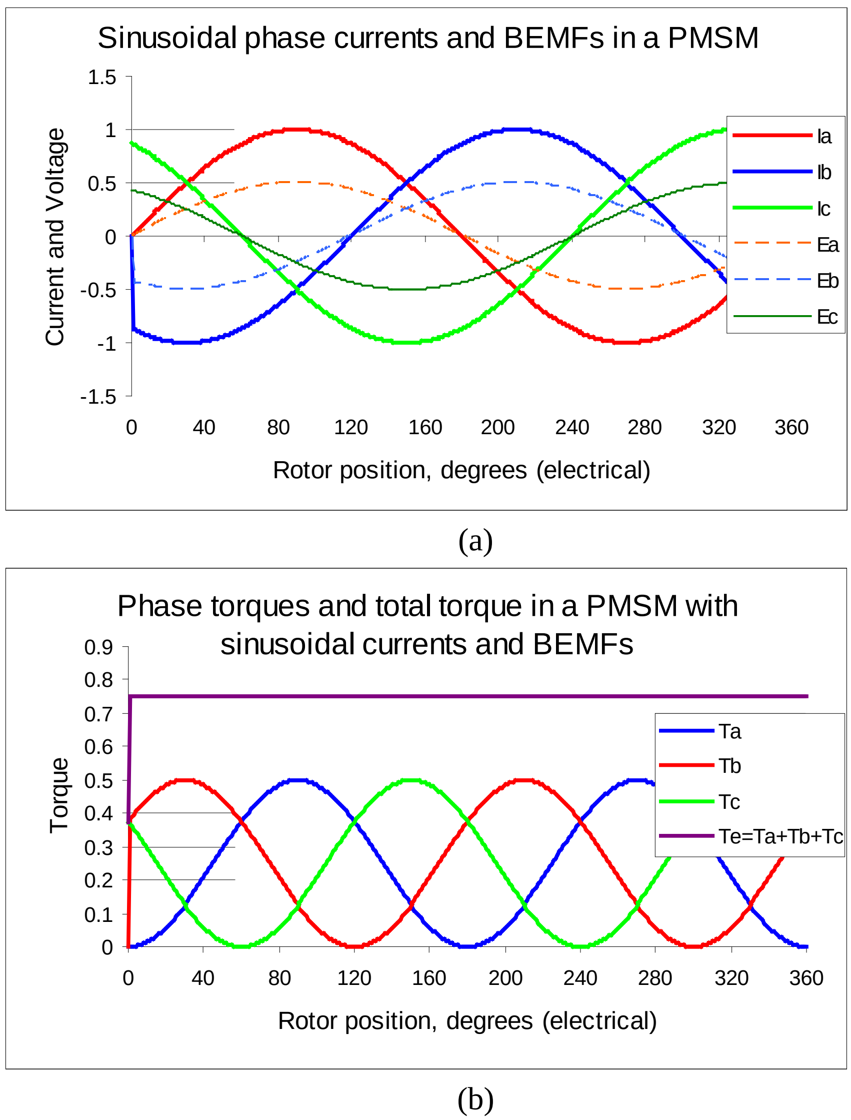

Figure 2.5: Torque production in an ideal PMSM (a) sinusoidal distribution of phase currents and BEMFs (b) phase torques and total torque.

produce torque oscillations. In case of a sinusoidal distribution of currents and sinusoidal induced voltages, the electromagnetic torque is a constant quantity as shown in Fig. 2.5. The torque suffers from pulsating or AC components if either the BEMFs or the stator conductors' distribution is not purely sinusoidal. A qualitative representation of the

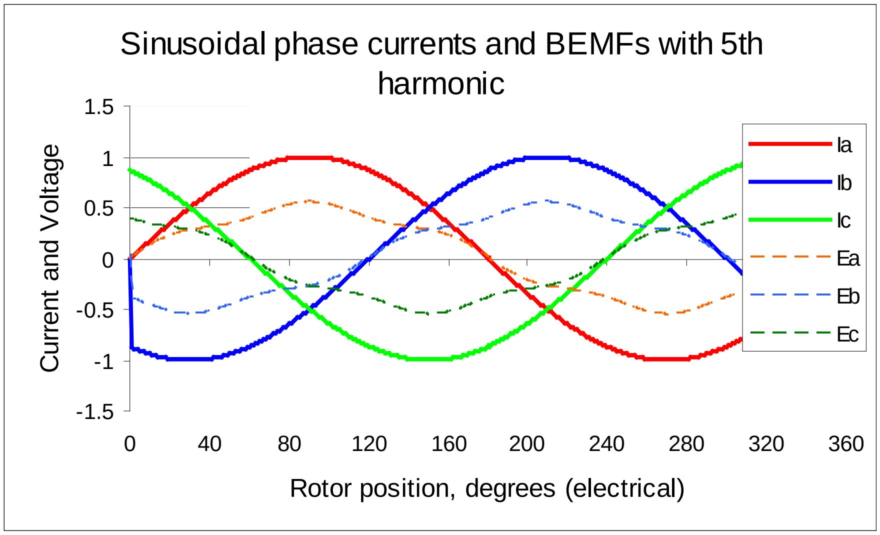

(a)

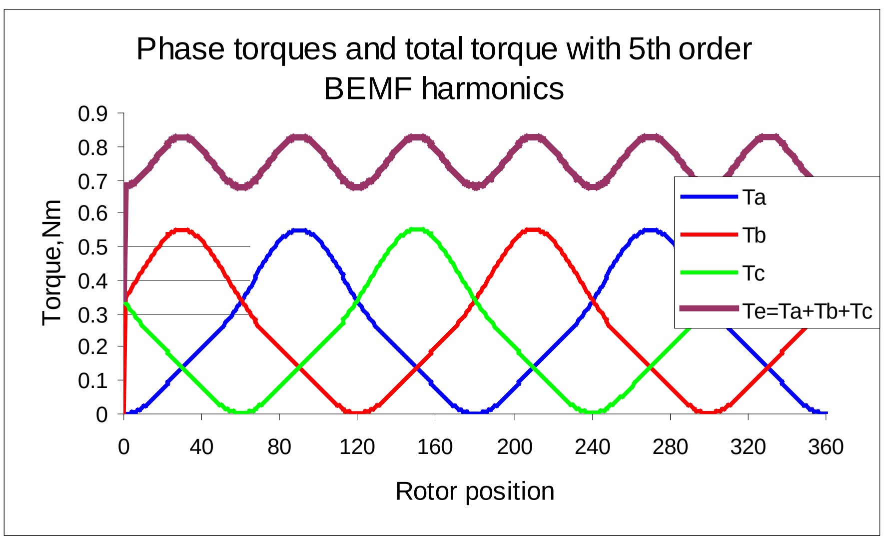

(b)

Figure 2.6: Torque production in a non-ideal PMSM (a) sinusoidal distribution of phase currents but BEMFs with a 5th harmonic (b) phase torques and total torque.

torque waveform for sinusoidal phase currents and phase BEMFs containing a 5^{th} order harmonics is shown in Fig. 2.6. Similar torque pulsations will be seen with harmonics in stator currents or with harmonics in both BEMFs and stator currents.

Field Weakening

The inverter can supply current to the phases as long as the BEMF is less than the maximum inverter voltage. Since the BEMF is proportional to speed, the maximum speed at which the machine can produce torque is bounded. With PMSMs direct field weakening is not possible due to the absence of saliency in the *dq* axes inductances. However, the stator BEMF voltage can be constrained at higher speeds by weakening the PM field. This can be explained using the *q*-axis stator voltage expression (Eq. 2.3a). The effect of PM flux can be influenced by controlling the stator currents such that the stator-current space phasor contains a *d*-axis component i_d along the negative direct axis in addition to the *q*-axis stator current component i_q.

The *d*-axis stator current component controls the airgap flux, while the *q*-axis current component is used for torque control. If i_d is positive or the phase advance angle is negative (phase lag), the armature or stator current produces an mmf around the air gap that tends to supplement the permanent magnet flux. If i_d is negative, the stator mmf is negative and causes demagnetization of the magnets. This method of phase advancing control can be effectively used for field weakening control of PMSMs [8, 9, and 10]. The *d*- and *q*- axes currents with phase advancing are shown in Fig. 2.7. In the figure, γ is the

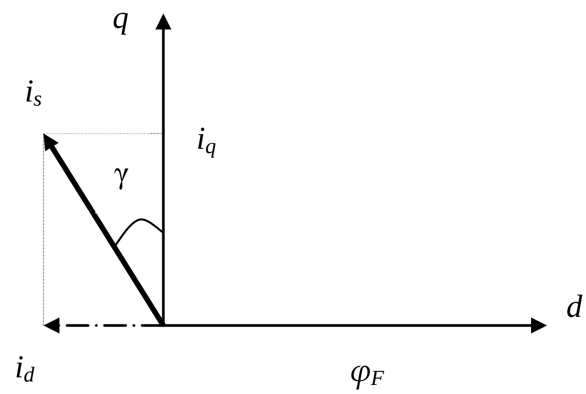

Figure 2.7: Phase diagram showing *d-q* components of stator current (positive value of γ represent phase advancing, negative value is for phase lagging).

phase advance angle and is measured from the *q*-axis. The *d*-axis and the *q*-axis components of currents are given by

$$\begin{aligned} i_d &= -i_s \sin\gamma \\ i_q &= i_s \cos\gamma \end{aligned} \tag{2.4}$$

The technique of phase advancing limits the machine BEMF, thus enabling higher speed operation. The *d*-axis current opposes the PM flux thereby weakening the flux; hence, the method is known as flux weakening. In practice, low machine inductance may limit the speed range because of excessive current needed for field weakening.

It is evident from the torque expression of PMSM (Eq. 2.4) that if L_d is almost equal to L_q then the torque is linearly varying with the *q*-axis component of current i_q. For positive or negative values of γ, the value of i_q decreases for constant stator current and hence the average torque also decreases.

2.5 Noise and Vibration in PMSM

It is very important to consider the noise and vibration problems during the process of electrical machine design. Electrical machine noise mainly consists of noise from electromagnetic, aerodynamic and mechanical origins. The machine vibration is primarily due to the eccentric position of the rotor with respect to the stator bore. The rotor eccentricity can be caused as a result of imperfection in rotor assembly which leads to shaft misalignment. Also, the unbalanced magnetic pull, if present in a motor even with perfectly aligned shaft, can create the rotor eccentricity. As a result, unbalanced forces exist in the machine air-gap that influences the radial vibration behavior, and therefore, the noise of the motor. The three categories of noise and vibration in electric machines are discussed below [43-45].

2.5.1 Electromagnetic

Electromagnetic (EM) vibration and noise are associated with parasitic effects due to higher space and time harmonics, eccentricity, phase unbalance, slot openings, magnetic saturation, and magnetostrictive expansion of the core laminations. The vibrating capability of the electronic machine is a function of two parameters, namely the mode number and the frequency. An annoying situation of “resonance’ arises where the frequency of the periodic exciting force is identical with or close to one of the natural frequencies of the machine.

Electromagnetic vibration and noise are caused by generation of electromagnetic fields. Both stator and rotor excite magnetic flux density waves in the air gap. If the stator produces $B_{m1}\cos(\omega_1 t + k\alpha + \phi_1)$ magnetic flux density wave and rotor produces $B_{m2}\cos(\omega_2 t + l\alpha + \phi_2)$ magnetic flux density wave, then the magnetic stress wave in the airgap is proportional to the product of the flux densities given as [19]

$$\begin{aligned} &\frac{1}{2}\{B_{m1}B_{m2}\cos[(\omega_1+\omega_2)t+(k+l)\alpha+(\phi_1+\phi_2)] \\ &+B_{m1}B_{m2}\cos[(\omega_1-\omega_2)t+(k-l)\alpha+(\phi_1-\phi_2)]\} \end{aligned} \tag{2.5}$$

where B_{m1} and B_{m2} are the amplitudes of the stator and rotor magnetic flux density waves, ω_1 and ω_2 are the angular frequencies of the stator and rotor magnetic fields, ϕ_1 and ϕ_2 are phases of the stator and rotor magnetic flux density waves, and k=1,2,3… and l = 1,2,3…

The magnetic stress wave in the airgap along with the slots, distribution of windings in slots, input current waveform distortion, air gap permeance fluctuations, and phase unbalance gives rise to mechanical deformations and vibrations.

The electromagnetic excitation sources in a PMSM are cogging torque, mutual torque ripple, and radial attractive force fluctuation between the rotor and stator.

2.5.2 Mechanical

Mechanical vibration and noise is mainly due to bearings, their defects, journal ovality, sliding contacts, bent shaft, rotor unbalance, shaft misalignment or rotor eccentricity, couplings, U-joints, gears etc. The rotor should be precisely balanced as it can significantly reduce the vibration. The rotor unbalance causes rotor dynamic vibration and eccentricity, which in turn results in noise emission from the stator, rotor, and rotor support structure. Again, the rotor eccentricity causes unbalanced magnetic pull in the airgap that leads toward vibration. For simplicity, eccentricity is considered as a magnetic source for noise and vibration rather than a mechanical source. This research will ignore the vibration and noise coming from mechanical sources since the relative magnitude of noise from mechanical sources in medium to small power motors is small compared to EM sources.

With appropriate design and manufacturing quality controls, mechanical noise normally has less contribution to the overall noise level of small/medium sized motors than the other two sources.

2.5.3 Aerodynamic

The basic source of noise of aerodynamic nature is the fan. Any obstacle placed in the air stream produces noise. In unsealed motors, the noise of the internal fan is emitted by the vent holes. In totally enclosed motors, the noise of the external fan predominates. According to spectral distribution of the fan noise, there is a broadband noise (100 to 10,000 Hz) and siren noise (total noise). The siren effect is a pure tone being produced as a result of the interaction between fan blades, rotor slots, or rotor axial ventilation ducts and stationary obstacles. Increasing the distance between the impeller and the stationary obstacle can reduce siren noise.

Small motors with shaft driven fans radiate much less noise when the speed is reduced below the rated speed. As the speed increases, the cooling fan becomes the primary source of noise. On the other hand, for motors with separately driven fans, no improvement in airflow noise is achieved when the speed is reduced.

Through continuous development of material science, design, and manufacturing technology, modern motors have smaller loss and better heat dissipation than those of previous generations; this allows the use of a smaller fan for cooling. Also, fan blade design technology has also improved. All these efforts minimize the motor aerodynamic noise. Large motors where the size of the cooling fan or blower is also large, the contribution of aerodynamic noise is significant. Small to medium size PMSMs with moderate speed has very little windage noise; the cooling fan, if any, does not contribute much to the total noise.

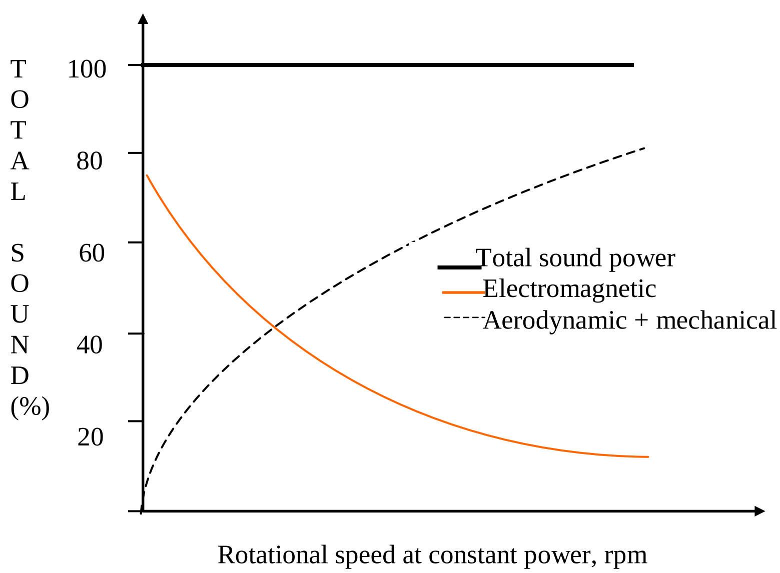

Figure 2.8: Typical relative contributions to total sound power radiation as function of speed.

The contributions to the total noise by all three categories are shown in Fig. 2.8 [11]. The contribution of electromagnetic source dominates mechanical and aerodynamic causes especially in case of a medium to low power PMSM. The large power motor (around 1 MW range) uses cooling fan or blower that is the dominant cause of noise. Also, these motors when used for high-speed applications suffer from additional mechanical noise caused by rotor bearing, gear or friction. Hence, the aerodynamic and mechanical sources of vibration and noise are not the focus of this research.

2.6 Improving Torque Ripple, Noise and Vibration

Low torque pulsations in motor drives are essential for high performance speed and position control applications where low acoustic noise and friendly human-machine interactions are demanded. The three torque components that contribute to torque ripples are reluctance torque, cogging torque and mutual torque. The reluctance torque in surface mounted PMSM is negligible; hence, it does not contribute to torque ripple. The cogging torque is a small fraction of total torque ripple. Thus, torque ripple improvement exclusively requires the reduction of key harmonics in BEMF and phase currents, which will minimize the mutual torque ripple component.

There is a fundamental relationship between noise and vibration in an electric machine. If the causes for the vibrating tendency of the electrical machine mechanical system can be eliminated or at least mitigated, then the noise and vibration will reduce considerably. The noise and vibration in the motors are mostly generated by the electromagnetic sources, which can subsequently be amplified by the dynamic characteristics of the motor structure. Certain factors of electromagnetic sources that give rise to measurable mechanical deformations and vibrations needs to be addressed properly to minimize the sound energy transformed from the vibrational energy.

Researchers around the world have been active over the past two to three decades to improve the machine performance in terms of torque ripple, noise and vibration. There are two different approaches to accomplish such work; design based approach and control based approach.

Noise and vibration reduction must start from the early design stages of the electric machine. This reduction method can be extended to some control based techniques for further enhancing the quieter performance of the machine. Several techniques of both the methods from the existing literature are discussed in the following sections.

2.6.1 Design Based Methods

Rotor/stator skew, teeth pairing i.e., use of multiple teeth, choices of slot-pole combinations, use of slotted/non-slotted stator are the common design methods to improve cogging torque, torque ripple and magnetic stress waves in the airgap. The authors in [1]-[4], [12] proposed several design variations of improving cogging torque and showed how it minimizes the torque ripple of the machine. The work by S. Huang, M. Aydin and T.A Lipo describes the appropriate selection of PM rotor shape and rotor skew angle to minimize the resultant sound power level, and hence, obtain a low noise motor design [14]. PM motors with fractional ratio of slot number to pole number have lower cogging torque but a considerable amount of unbalanced magnetic force [13]. Again slot-less motor have less torque ripple and zero cogging torque compared to slotted motor [14].

Different methods of design variations are discussed in the following section in the context of cogging torque improvement, torque ripple minimization and radial force reduction. A list of common measures in relation to design variation is given as follows:

- Elimination of slots [15]
- Skewed slots [18]
- Special shape slot [1,3]
- Selection of number of slots with respect to number of poles [30, 31]
- Decentered magnets [11]
- Skewed magnets [1]
- Shifted magnet segments [1]
- Selection of magnet width [35]
- Direction-dependent magnetization of PMs [11]

Cogging Torque

Cogging torque is the zero average pulsating torque caused by the tendency of the PM to align with the stator iron. This appears whenever magnet flux travels through a varying reluctance. A simplified expression of cogging torque is given by equation (2.6) where ϕ_g is the magnet flux crossing the air gap and $\Re$ is the total reluctance through which the flux passes. Clearly, if the reluctance $\Re$ does not vary as the rotor rotates, the derivative in (2.6) is zero and the cogging torque is zero. In addition, cogging torque is independent of flux direction as the magnet flux ϕ_g is squared. Again, the reluctance of the PM and the iron core are negligible compared to air gap reluctance and thus the reluctance here exclusively refers to the air gap reluctance.

$$T_{cogg} = -\frac{1}{2}\phi_g^2 \frac{d\Re}{d\theta} \tag{2.6}$$

Cogging torque results from interaction between the permanent magnets and the stator slots. The most common technique for cogging torque reduction is stator slot skewing. The idea is to reduce the change of reluctance with position and thus to reduce the cogging torque. The net change in reluctance can be minimized if the slot openings are spread over the surface area of the magnet as depicted in Fig. 2.9. Here, the slots are skewed so that each magnet sees a net reluctance that stays the same or nearly the same as slots pass by. In this way, changes along the axial dimension reduce the effect of changes along the circumferential dimension. As a result, the $d\Re/d\theta$ experienced by the entire magnet decreases, and consequently, the cogging torque decreases. The same effect can also be obtained by shaping the stator slots using any of the following techniques:

a) Bifurcated slots [1]

b) Empty or dummy slots[38]

c) Closed slots [11]

d) Teeth with different width of the active surface (teeth pairing) [3]

The same results can be achieved by skewing the PMs where each magnet can be represented by a number of straight rotor bar segments offset from each other by a fixed angle. This type of magnet skew is called step skew. There is another type of skew called continuous skew where the each magnet pole is a skewed rotor bar. The detail of a 3-step skew scheme is described in chapter IV.

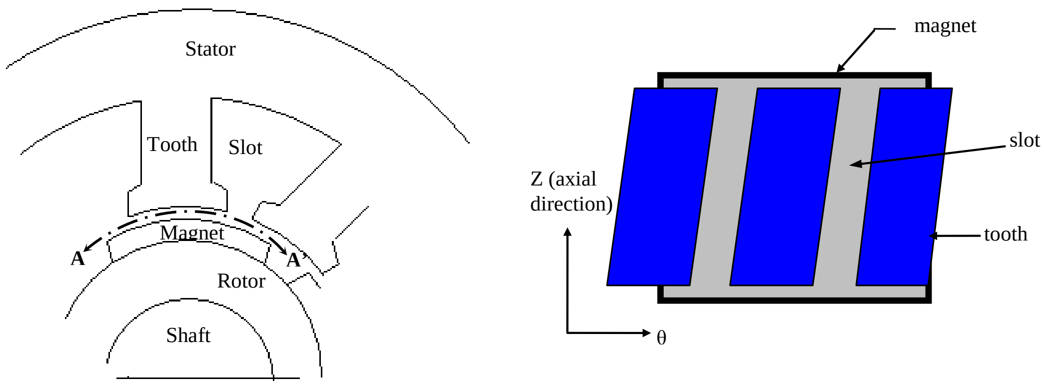

(a) (b)

The number of periods of the cogging torque waveform N_{period} during a rotation of a slot pitch depends on the number of slots and poles. For a rotor with identical PM poles, equally spaced around the rotor, N_{period} is given by

$$N_{period} = \frac{N_p}{HCF\{N_s, N_p\}} \tag{2. 8a}$$

where N_s and N_p are the number of stator slots and rotor poles, respectively, and $HCF(N_s,N_p)$ gives the highest common factor between N_s and N_p.

The mechanical angle corresponding to each period required to completely eliminate the cogging torque is the optimum skew angle θ_{skew} given by

$$\theta_{skew} = \frac{2\pi}{N_{period} N_s} \tag{2. 8b}$$

Equation (2.8b) shows that the cogging torque is also a function of stator slots and rotor poles. The closer the number of slots is to the poles, the higher is the cogging torque period and the lower is its amplitude. The selection of slot-pole combination can thus reduce cogging torque significantly. The use of slotless stator is another novel way of eliminating cogging torque [15]. Since the PM field and stator teeth produce the cogging torque, a slotless motor can totally eliminate the cogging torque. A slotless structure requires increased air gap, which in turn reduces the PM excitation field. To keep the same air gap magnetic flux density, the height of PMs must be increased. Slotless PMSMs therefore use more PM material than slotted motors.

The research by Hwang *et al*. shows the use of teeth pairing with two different tooth widths for significant improvement in the cogging torque. The airgap permeance function is modified as the period is doubled with teeth pairing compared to single tooth situation. A model of teeth pairing with simplest airgap permeance function is shown in Fig 2.10. The fundamental component of air gap permeance G_{nN_L} as well as the cogging torque can be eliminated with appropriate combinations of two different tooth widths *a* and *b* as shown in Fig. 2.10. Without teeth pairing (*i.e.*, *a* = *b*), the period of airgap permeance is *2π/Ns* and with teeth pairing the period is *4π/Ns*. The cogging torque and permeance is given by [3].

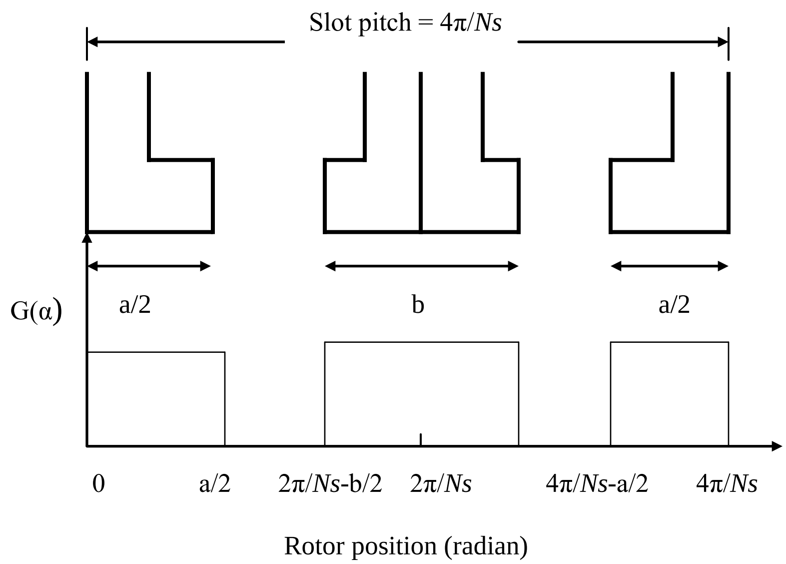

Figure 2.10: Teeth pairing in stator slot and corresponding permeance function.

$$T_{cogg}(\theta) = -\frac{\partial W_g(\theta)}{\partial \theta} \propto \int_0^{2\pi} G^2(\alpha) B^2(\alpha,\theta) d\alpha \propto \sum_{n=0}^{\infty} nN_L G_{nN_L} B_{nN_L} \sin(nN_L\theta)$$
$$G_{nN_L} = \frac{N_s}{\pi} \frac{1}{nN_L} 2[\sin nN_L \frac{a}{2} + \sin nN_L \frac{b}{2}] \quad (2.\ 8c)$$

where N_L is the least common multiple of N_s and N_p, W_g and B are the air gap energy function and air gap flux density function, respectively.

Torque Ripple

Torque ripple can cause undesirable vibrations [2, 17, 20, and 34] in the load response. Torque ripple consists of two components: electromagnetic torque fluctuation and cogging torque. Electromagnetic torque ripple is caused by the harmonic interaction between the BEMF and the phase currents associated with the motor electrical dynamics.

The instantaneous electromagnetic torque for a 3-phase PMSM can be given by [18]

$$T_e = \sum_{x=a,b,c} \frac{e_x i_x}{\omega} + \frac{1}{2}\phi_g^2 \frac{d\Re}{d\theta} \tag{2.9}$$

where e_x and i_x represent the phase BEMF and phase current, respectively, and the second term in the expression represents the cogging torque. The first term in (2.9) is known as the electromagnetic torque or the mutual torque. The motor can produce constant electromagnetic torque only if the part of the flux through stator windings due to the rotor field known as mutual flux is purely sinusoidal. This also requires sinusoidal spatial distribution of either the stator windings, or of the field due to rotor magnets. In practice, the perfect sinusoidal distribution is not achievable and the mutual flux contains higher harmonics and causes ripple in steady state torque in response to a purely sinusoidal current excitation. The torque ripple cannot be separated from cogging torque; most of the researchers mentioned these two issues together [2, 11, and 23]. Therefore, the design methods developed for reducing cogging torque can also be considered as the methods for reducing torque ripple.

Carlson *et al.* formulated an optimized design problem by evaluating the maximization of the EMF fundamental component and the minimization of the torque ripple without separating the different contributions [16]. The optimization problem was set as

$$\begin{aligned} & \min(f) \\ \text{subject to} \quad & q_1 = 0 \\ & q_2 < 0 \end{aligned}$$

where the cost function f is given by

$$f = \sum_{k=3,odd}^{\infty} c_{E,k} \frac{E_k^2}{E_1^2} - c_{E,1} \frac{E_1^2}{E_{1,\max}^2} + \sum_{k=1}^{\infty} c_{T,k} \frac{T_{c,k}^2}{T_0^2} \tag{2.10}$$

Here, E_k^2 is the squared amplitude of the k^{th} EMF harmonic component. E_1^2 and $E_{1,\max}^2$ are the squared amplitude of the first harmonic component and its maximum value (with pole arc equal to pole pitch), respectively. $T_{c,k}^2$ is the squared amplitude of the k^{th} cogging torque harmonic component. $c_{E,k}$, $c_{E,1}$, $c_{T,k}$ are the weighted coefficients. The constraint $q_1 = 0$ guarantees the geometrical consistency of the rotor. In the constraint $q_2 < 0$, a lower bound to the distance between the magnets is taken. The unknowns of the optimization algorithm are the length of the magnets and their positions, the skew length, and the number of tooth intervals *r* by which the pitch of the primary winding is shorted. The first term of the optimization function minimizes the dominant BEMF harmonics of order 3, 5, 7 etc. to minimize ripple, the second term maximizes the fundamental harmonics to have maximum output torque, and the third term minimizes the cogging torque. Their analysis provided results showing the elimination of certain harmonics in

BEMF for a particular value of magnet arc; this arc length depends on the number of poles in the machine, winding arrangement in the stator, and amount of magnet skew.

In surface mounted PM machines, the magnet shape determines the distribution of the air-gap magnetic field when influences of armature reactance of load currents are ignored. The practice is to start with a given magnet shape, and then to obtain the magnetic flux density curve by 2-D or 3-D FEA calculation. The curve is compared to the standard waveform and the FEA is repeated until a satisfactory waveform is obtained [35]. For example, if the 5th harmonic in BEMF needs to be eliminated then the pole arc angle (θ_m), shown in Fig. 2.11, should be selected such that 5 θ_m = $n180^0$, where n = 1,2,3,... If the machine has p pair of poles, then the mechanical degrees of θ_m is given as $\theta_m(mech) = \theta_m/p$. Generally, 5th and 7th order harmonics in BEMF are the most significant and any one of these can be eliminated completely by selecting the pole arc angle using the above procedure.

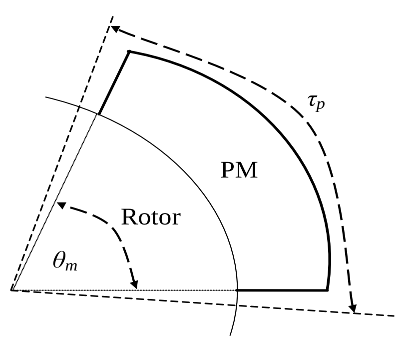

Figure 2.11: Defining magnet parameters, pole arc angle, and pole pitch.

S. Huang, *et al*. in their research showed that the optimum selection of pole arc ratio and magnet skew angle can minimize the ripple torque and optimize the machine performance [20]. The sizing procedure starts by defining the output power as a product of air gap phase EMF and phase currents

$$P_e = \eta m \frac{1}{T}\int_0^T e(t)i(t)dt$$

where *e(t)* and i*(t)* are the phase air gap EMF and phase current, respectively. These two periodic functions are given as

$$\begin{aligned} e(t) &\propto NB_g \frac{f}{p}\lambda_0 D_0 L_{stk} \\ i(t) &\propto \frac{A\pi\lambda_0 D_0}{(1+K\phi)}.\frac{1}{N} \end{aligned} \tag{2.11}$$

The parameters used are:

η	- machine efficiency
m	- number of phases
T	- period of the EMF
N	- number of turns per phase
B_g	- air gap flux density
f	- converter frequency
p	- pole pair
λ_0	- ratio of outer surface diameter to air gap diameter
D_0	- outer surface diameter
K_Φ	- ratio of electrical loading on rotor to stator
A	- total electrical loading

The power output of the PMSM can be obtained by combining *e(t)* and *i(t)* in terms of the primary dimensions, magnet property, and electrical loading. The machine torque density and power density equations given by (2.12) can then be used to find the motor dimensions like outer surface diameter D_0, rotor diameter to the airgap D_{tot}, and so on. These dimensions can be utilized to find the optimum values for magnet length and width.

$$
\begin{aligned}
T_{den} &= \frac{P_e}{\omega \frac{\pi}{4} D_{tot}^2 L_{tot}} \\
P_{den} &= \frac{P_e}{\frac{\pi}{4} D_{tot}^2 L_{tot}}
\end{aligned}
\tag{2.12}
$$

The research presented in this dissertation investigate further to show that the variation in magnet shapes with the same pole arc ratio and skew angle can affect the torque ripple significantly. A systematic approach is then developed to design the PMSM with minimum torque ripple, and less noise and vibration.

Radial Force

The attraction force between the rotor permanent magnets and the stator iron is known as radial forces. In an ideal situation where the shaft alignment with respect to the stator is perfect enough to maintain a uniform airgap and the phase windings are balanced, the motor sees a constant stress wave along the stator periphery. Any deviation from this ideal condition creates unbalanced radial force and excites the stator structural response. This can radiate unwanted acoustic noise depending on the frequency and amplitude of the excitation force.

The authors in [13] calculated the unbalanced force components analytically and validated by finite element analysis using Maxwell's stress tensor method. The analysis was carried out for 3-slot/2-pole and 9-slot/8-pole PMSM and PMBLDC motors. Each phase of the 9-slot/8-pole machine comprises of three adjacent coils connected in series, the middle coil being of opposite polarity to the other two coils. Although the windings of phases A, B and C are displaced by 120^0 Elec. and their BEMFs are symmetrical and phase shifted by 120^0 Elec., the disposition of the phase windings about the diameter of the machine is asymmetrical. This result in an unbalanced magnetic force between the rotor and the stator.

Researchers have analyzed the radial forces by FE tools to show the differences between two types of fractional slot PMSMs based on their winding configuration [21]. One type of PMSM has the traditional concentrated winding, while the other type has non-traditional winding where the coils of each phase are placed in diametrically opposite slots. The later type is called the "modular" winding machines. Other researchers have measured the radial forces from the air gap flux function without breaking it into its constituents of rotor and stator fluxes [13]. First, the radial pressure is proportional to the square of the normal component of airgap flux density and can be estimated by the equation given below (2.13). The next step is to calculate the radial force on a tooth by multiplying radial pressure with tooth area. This research presents a detail analysis on the formation of radial force.

$$P_r \approx \frac{B_n^2}{2\mu_0}$$
$$F_{rad} = A_{tooth}.P_r \qquad (2.13)$$

A summary of possible design based methods to control radial force is listed below:

- Increasing airgap
- Reducing the magnet strength
- Improving shaft alignment or rotor eccentricity
- Use of balanced winding
- Increasing resonant frequency by changing lamination dimensions

The idea of increasing airgap or using a lower strength magnet is to reduce the magnetic stress waves in the airgap. The adoption of these techniques leads to reduction in useful torque also. The improvement in shaft alignment is completely dependent on the manufacturing capability and might work out well. Some motor configurations are unable to have balanced winding, for example a 3-phase PMSM with 9-slot/8-pole combination; some configuration has possibility to have both a balanced and an unbalanced winding, for example a 3-phase PMSM with 12-slot/10-pole combination; and some are by default balanced, for example a 3-phase PMSM with 9-slot/6-pole combination. In the second type of motors even with balanced winding there is possibility of having unbalanced radial stress that can cause vibration. The research is aimed to elaborate the vibration behavior of those motors in particular. Also, the following chapter will explain how the natural resonance frequency of the motor structure can be increased by changing the stator dimensions.

Methods based on the motor design (skewing, shifting the magnet position, special windings, etc.) are more difficult than control-based methods. The main drawbacks of these design based methods are the reduced average (nominal) torque and the increased complexity of the motor construction, resulting in higher overall costs.

2.6.2 Control Based Methods

Machine performances in terms of torque ripple, noise and vibration can also be improved by several control methods. Control techniques mainly use modulation of the stator current or BEMF waveforms. The control techniques adopted for obtaining ripple free torque and reduced radial forces are:

- Open-loop control (harmonic cancellation technique) based on programmed current waveform [28]
- Closed-loop control including flux and/or torque estimators [5]
- Alteration of motor commutation pattern, and therefore, the pattern of the force pulses [24]
- Increasing the number of stator phases to have lower radial forces [27]
- Concentrated windings with enlarged air gap for minimizing radial forces [24]
- Field weakening operation with higher currents for reduced radial forces in sinusoidally excited BLDC motors [6].

Bojan Grcar *et al.* proposed control based reduction of pulsating torque for PMSMs [5]. The researchers subdivided the method into two basic groups: open-loop control (harmonic cancellation technique based on programmed current waveform), and closed-loop control including flux and/or torque estimations. The work of Asano, Yoshinari *et al.* concluded that the vibration of concentrated winding motors tends to be higher than distributed winding motors [24]. Field weakening technique can reduce radial forces in sinusoidally commutated PMBLDC machines [6], but requires higher currents to maintain the desired torque. Smoothening the drive current to prevent torque ripple can also reduce vibration [26]. Increasing the number of stator phases can also reduce the exciting forces, and hence, the vibration of the machine [27].

Control based methods [4-7], [16, 17, and 23] without influencing the drive hardware can be implemented in a low cost digital signal processor (DSP) and field programmable gate array (FPGA) based motor control hardware; however, the obtained torque is never entirely smooth.

Cogging torque is directly related to torque ripple and both of them causes noise and vibration in the machine [1-7]. Radial forces cause significant vibration when they are unbalanced. To improve the performance of a motor, torque pulsations need to be reduced and unbalanced radial forces are to be minimized either by design variation or through control techniques. It is hard to find some designs with low torque ripple and cogging torque as well as with low radial forces. There is always a trade-off among these two phenomena.

2.7 Shortcomings in Existing Research

In spite of the several techniques discussed in this chapter to improve the performance of PMSM, there are still opportunities for further research, especially from a design point of view. The existing literature cover the variation in magnet design by changing the pole arc, but do not cover the variation in magnet shapes within a particular pole arc. The research in this dissertation will show that fairly simple variations in magnet shapes can lead to substantial improvements in torque ripple minimization without sacrificing the average torque significantly. These magnet shape variations can be implemented in a very cost effective manner. Also, the existing literature showed that magnet skew can reduce cogging torque as well as torque ripple. This research in particular has shown that this is not always the case and there are ways to utilize appropriate skew techniques.

Unbalanced radial forces cause the stator deflection, which produces vibration. Existing literature do not show the differences in radial forces between modular and non-modular motors; the relationship of vibration with radial displacement of the stator yoke is yet to be established. The existing research provides no theoretical basis for relating the noise and vibration with motors of different geometry. Identifying the variation in radial stress due to variation in winding and motor topologies, developing model to predict vibration as a result of the radial stress, and finally relating vibration with acoustic noise are within the scope of this research.

2.8 Research Motivation

Use of skewed magnets, shifted magnet segments, decentered magnets or selection of magnet width can reduce the cogging torque, and supposedly the torque ripple as well. But, in reality these methods may not necessarily reduce the torque ripple and can even make it worse. It is the dominant order(s) of BEMF harmonics present in those design variations that will determine the reduction or increase of the torque ripple in a skewed motor. Moreover, selection of magnet arc width can eliminate one particular harmonics of BEMF, but no other BEMF harmonics can be removed. Hence, further research needs to be conducted to see the torque ripple variation (increase or decrease) under magnet skewing for different geometry of PMSM. The determination and elimination of more dominant BEMF harmonics by variation in magnet shapes for a particular slot-pole combination motor with a selected magnet arc width will give a motor design with low torque ripple.

The symmetric arrangement of the magnets by making pole arc equal to pole pitch leads to the maximum value of the fundamental component of the BEMF. However, with this magnet arrangement, the other harmonics of the BEMF are also high to cause a significant torque ripple. In general, a nonsymmetrical distribution of magnets having different pole arc and pole pitch leads to a reduction of the fundamental component of BEMF and also to a variation of the other harmonic components. Therefore, it is possible to find a suitable magnet arrangement leading to a compromise between a high value of the BEMF fundamental component and a low value of all other harmonic components, thus leading to a high-performance motor. Research is thus essential to develop the fundamental understanding of the relationship between magnet shape and BEMF, and then develop the methodology to eliminate certain high order harmonics of BEMF by appropriate shaping of the magnets.

The vibrating tendency of PMSMs doesn't show a direct correlation with the magnitude of the radial stress wave on its stator structure. It also depends on the dominant frequency of the stress wave. Again, it is not only the motor topology (slot/pole combination), but also the winding configuration that determines the lower order frequency of radial stress responsible for vibration. This research is thus motivated to unveil all of the above in selecting a PMSM less prone to noise and vibration.

2.9 Research Objectives

Based on the literature review presented in this chapter, the following research objectives have been set forth:

- Determination of the peak-to-peak torque ripple vs. phase angle characteristics for different PMSM geometry.
- A complete study of the peak-to-peak torque ripples variation with magnet skewing for different motor topology and with various magnet shapes.
- An investigation to identify the key BEMF harmonics, and therefore, the key orders of electromagnetic torque ripple with different magnet shapes.
- Design of magnet pole arc and pole shape, selection of slot-pole combination and rotor/stator skew scheme to specify a low torque ripple motor with less noise and vibration.
- FE analysis for several motor topologies to investigate the variation in radial forces.
- Development of an analytical model to calculate the radial deflection using radial forces by FEA and to validate the model with structural finite element analysis and test results.

The above objectives are crucial for the design and development of a high performance PMSM. The tasks to achieve these objectives have been organized into three categories:

i) A comprehensive design methodology.

ii) Torque ripple and cogging torque analysis.

iii) Noise and vibration analysis.

2.10 Conclusions

Simple, low-cost, and effective ways to reduce torque ripple, noise and vibration in PMSM can not be found in the literature. The literature also claims the indirect effect of cogging torque reduction in reducing the torque pulsations in [2, 3, and 7] without validation. The research presented in this dissertation will formulate a methodology to choose a design with rotor skewing that can minimize the torque ripple. It will also show the magnet design cases where torque ripple gets worse even after rotor skewing.

This research will show how the different shapes of magnet for a particular pole arc can make differences in the peak-to-peak torque ripple in a skewed motor compared to its non-skewed version. This research will also show in detail the stator excitation due to magnetic radial pressure, the mode shapes and mode frequencies responsible for structural vibration, and how this phenomenon varies with motor topology and winding configuration. In this regard, a detailed analytical model for predicting radial displacement as well as vibration based on radial pressure on the tooth will be included in this research.

CHAPTER III

COMPREHENSIVE DESIGN METHODOLOGY

A design methodology for surface mounted PMSM with a given set of design constraints is developed in this chapter. The primary constraints considered are the maximum outer diameter of the stator, the allowable axial length of rotor and stator laminations, the radial depth of the airgap between rotor and stator, the torque and speed requirements and so on. Techniques for reducing cogging torque, torque ripple and radial forces have been incorporated throughout the systematic design approach.

The fundamental steps involved in designing a surface mounted PMSM are described first. The design starts with the specifications that may include the requirements of rated torque T_{rated}, maximum power P_{max} or rated speed $\omega_{mrate.}$ Supply bus voltage V_{bus} or dimensions may also be included as constraints. Needless to say that the specifications are application-specific. Aside from the motor design there may exist several other environmental and performance requirements that must be taken into account. The next design steps include the initial selection of the surface mounted PMSM configuration, design parameters and design-ratios (ratios between internal dimensions). Configuration options may include the number of phases, the number of stator and rotor poles, and the number of series or parallel paths in each phase which is also called repetition. Design parameters may include hoop stress T_s, rms current density J_{rms} and rotor torque density $T_{density}$. After selecting the configuration, parameters and design ratios, internal and external motor dimensions such as rotor radius R_g, stack length L_{stk}, stator outer radius R_{out} etc. are determined through the design equations; an analytical parameter model is then developed to predict the torque ripple and radial forces of the motor. If the output requirements are satisfied, then static and dynamic system level simulations are carried out for verification of overall performance.

3.1 Design Methodology

The electrical machine design is a multi-disciplinary subject. It involves electromagnetic design, engineering materials selection, thermal and mechanical analysis, material and component specifications and production techniques. The magnetic properties of the iron, the numbers of phases and the number of poles-per-phase all have effect on PMSM's performance. These effects along with the sizing of the machine envelope and internal dimensions make the PMSM design an insight intensive effort. In designing PMSM, except for the most basic sizing calculations, the CAD (computer aided design) methods must include system level simulation capability as an integral part of the design process. Finite element analysis is also needed for the understanding of motor performances at design variations.

A number of requirements and objectives need to be compromised to achieve an optimal PMSM design for a specific application. Various PMSM design aspects have been studied and reported in the literature [29-32] emphasizing some of the design parameters, the number of phases and repetitions and a few dimensional design ratios. The traditional design process starts with some initial realization derived from experience without going through any optimization routine.

One of the main design requirements addressed in this dissertation is torque ripple minimization. This requires the motor to possess a good BEMF waveform (sinusoidal in the case of PMSM) and low cogging torque. Magnet arc length selection and shaping the magnet arc to minimize the BEMF harmonics are necessary to achieve the goals. A further requirement is to maintain lower radial forces to have less radial deflection. This requires correct selection of slot-pole combinations and proper winding arrangements around the stator circumference. A comprehensive design methodology, which sets design guidelines to encompass the effects of machine geometry, configuration and all possible design parameters on the overall performance of the PMSM, will thus, be developed in this research.

The various dimensions of the rotor and stator, defined as motor parameters for the CAD design program, are shown in Fig. 3.1. The 3-phase winding configuration cited in Fig. 3.1(a) has the number of repetition being 1 as there is only one coil per phase distributed within 180° in space. The symbols of the stator slot and teeth dimensions can be found in Fig. 3.1(c).

Another important part of design is the rotor magnet sizing. The pole arc can be varied with respect to pole pitch and slot pitch or coil pitch to make the flux distribution square wave or sinusoidal as per application requirement (Fig. 3.2). A square wave shape

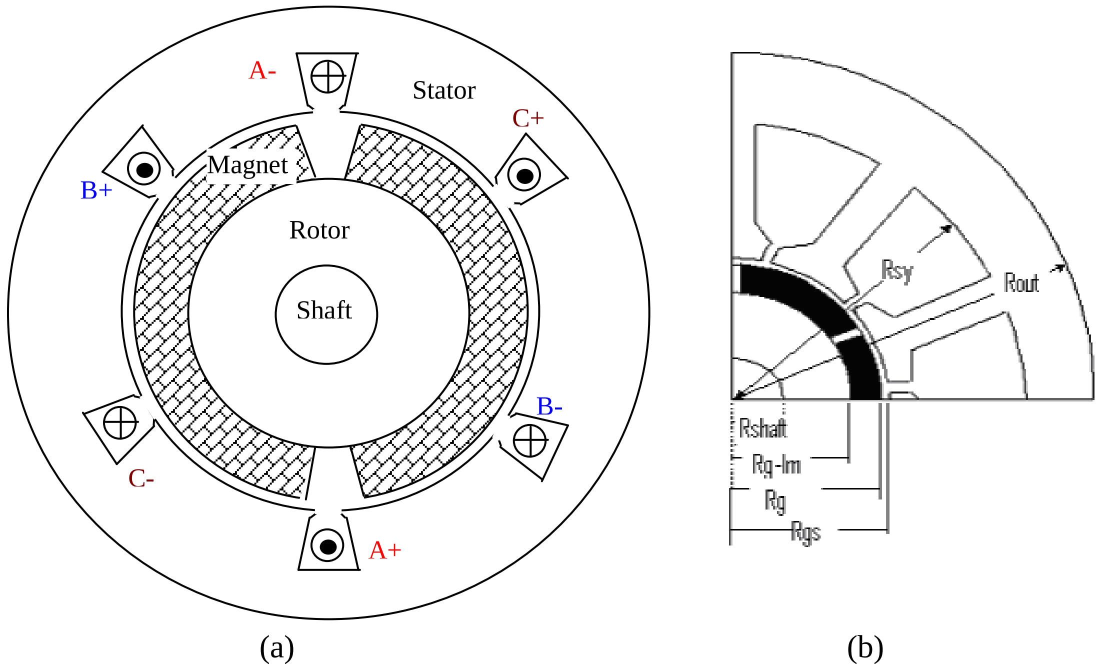

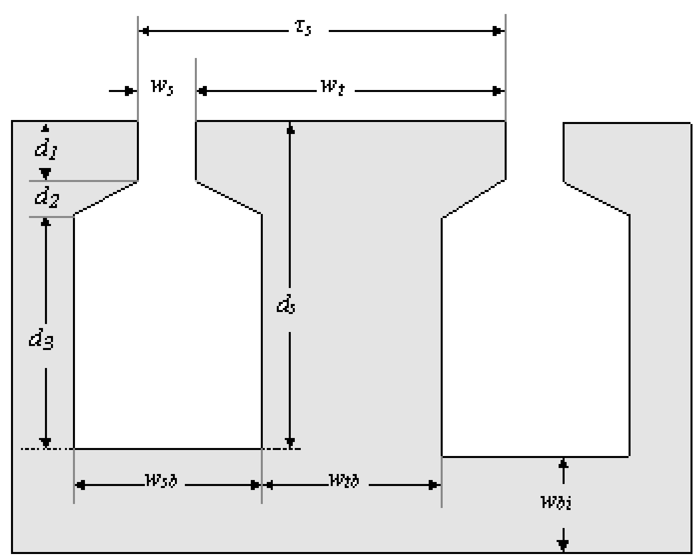

(c)

Figure 3.1: Schematics of a PMSM (a) A 3-phase winding layout (b) Sectional view with different rotor and stator radii (c) Dimensions of the stator tooth and slot.

of the flux distribution is obtained when $\tau_c = \tau_p$; the flux linked with the winding in this case is

$\phi_g = B_g.L_{stk}.\tau_p$, where L_{stk} is the length into the page [32]. Again, the sinusoidal distribution of the flux density is obtained when $\tau_c < \tau_p$; the flux linked with the winding is $\phi_g = B_g.L_{stk}.\tau_c = 2.B_g.L_{stk}.\sin(\theta_{ce}/2)$. Here the pitch factor is defined as

$$k_p = \theta_{ce}/\pi = \frac{\tau_c}{\tau_p}.$$

More details of flux density distribution shapes with variation in pole arc compared to pole pitch and coil pitch are discussed in chapter IV.

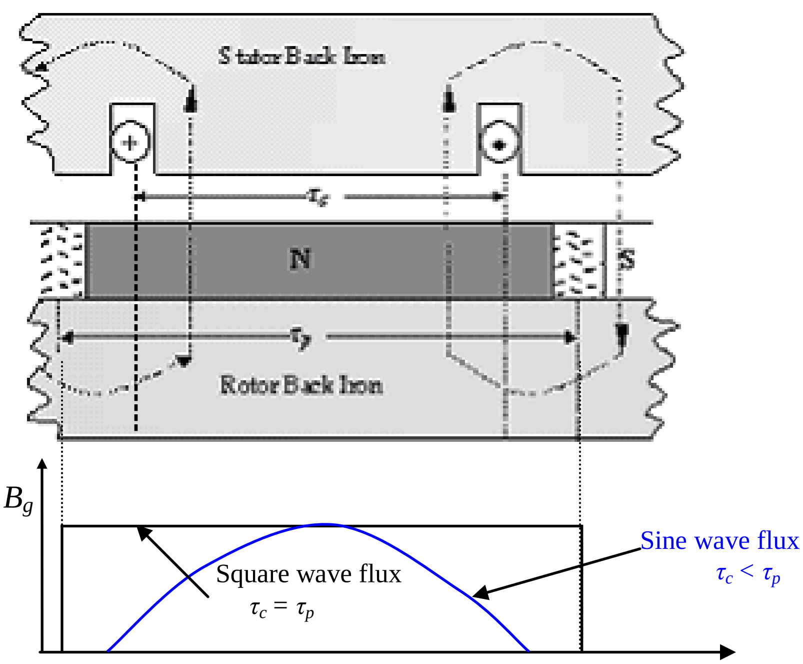

Figure 3.2: Air gap flux distribution pattern for cases when pole pitch and slot pitch are equal and different.

3.2 Design Steps

The design steps include the initial selection of the configuration, parameters and dimensional design ratios; evaluation of critical design issues; validation of an "*output checklist*"; verification of overall performances by system level simulations and finite element analysis (FEA). The design specifications may include all or some of the following parameters depending on the application: rated torque, base speed, maximum rated speed, maximum output power, power factor, supply bus voltage, maximum phase current, torque-ripples, acoustic noise level etc. The number of phases, poles, stator slots as well as winding configuration must be selected based on the application requirements.

The first step is to define the important ratios of the machine dimensions. The design constraints are the iterative process of the design software and simplified output equations are used for the initial sizing and output checklist to simplify the back and forth adjustments of the design variations. The machine configuration, parameters and design ratios are changed within their limits to obtain a satisfactory output checklist for the design. Finally, fine tuning of the design to achieve the accurate static and dynamic performances of the candidate design is carried out through FE analysis of the machine. The design steps are continued in an iterative process until the requirements are met.

3.2.1 Design Ratios

The design ratios are defined as the ratios between various internal dimensions of the machine. The objective of defining the design ratios is to maximize the stator mode

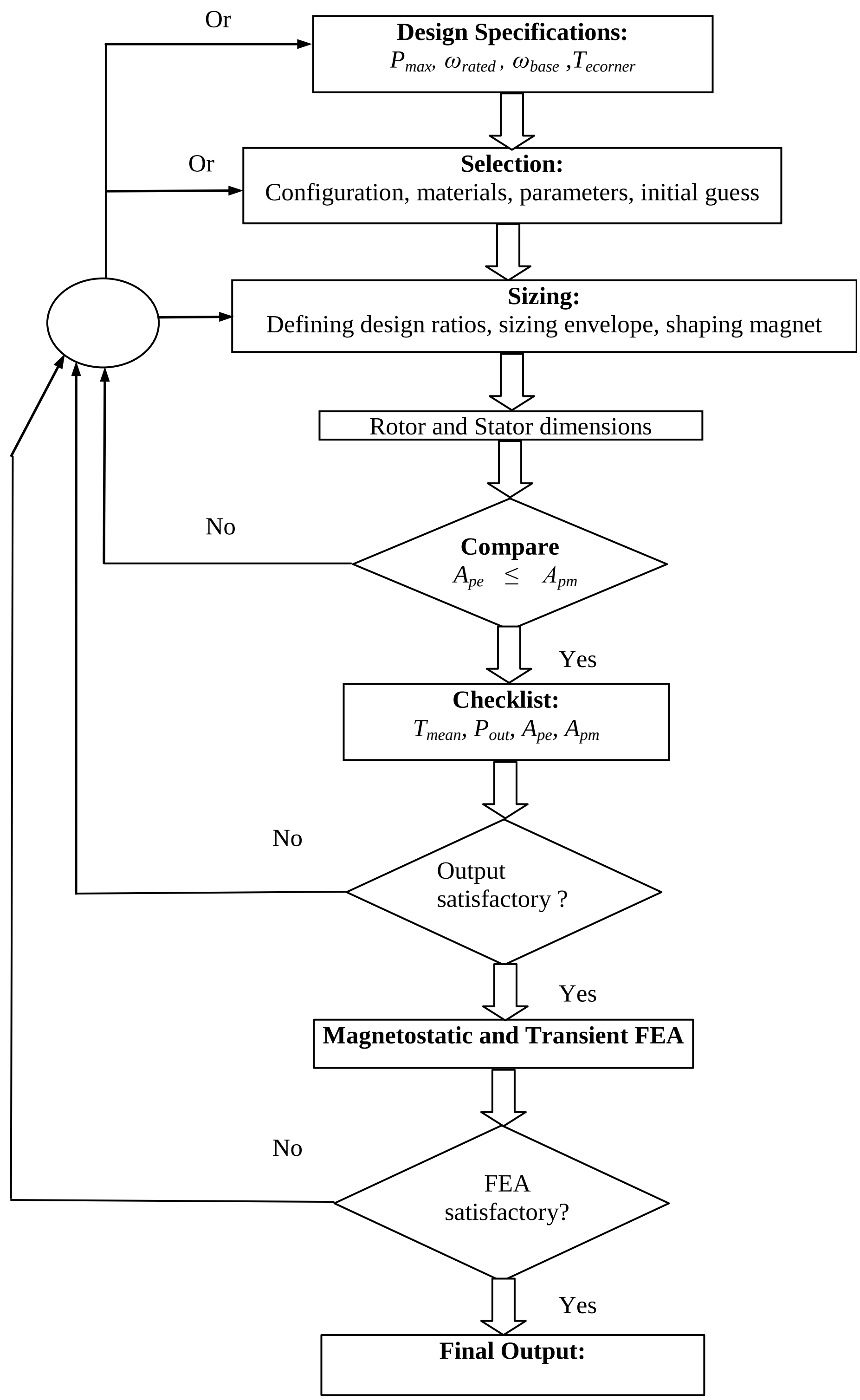

Fig. 3.3: Flowchart of the overall design methodology of PMSM.

frequency, to minimize the envelope dimension, and to insure critical speed well above the rated speed of the machine. Referring to the dimensions shown in Fig. 3.1, the following design ratios are

$$\alpha_{lmrg} = \frac{l_m}{R_g}, \qquad \alpha_{yrys} = \frac{y_r}{y_s} = \frac{w_{bi}}{R_{yr} - R_{shaft}},$$

$$\alpha_{sd} = \frac{d_1 + d_2}{w_{tb}}, \qquad \alpha_{rourrg} = \frac{R_{out}}{R_g}, \text{ and } \qquad \alpha_{lmds} = \frac{l_m}{d_s} \tag{3.1}$$

The ratio between the magnet width, l_m and the slot height, d_s (α_{lmds}) is a comparison between magnetic loading vs. electrical loading, a ratio between magnet size and winding area, and has a significant effect on torque density and mean torque. It indicates a trade off between magnet width and the amount of stator conductors to meet the required torque. The higher the ratio is, the lower is the height of the slot and less would be the number of conductors possible; also, the higher is the thickness of the magnet. The ratio between the outer radius of the stator, R_{out} and the outer radius of the rotor, R_g (α_{routrg}) is a way of constraining the rotor diameter for a given stator diameter and generally set to 2 as a starting point of design iteration. The objectives for selecting optimal values for α_{lmrg} ,α_{routrg} , and α_{lmds} are to minimize the envelope dimension which is the product of R_{out} and L_{stk}. The selection of the ratio between rotor back iron, y_r and the stator back iron, y_s (α_{yrys}) is critical to maximize the stator mode frequencies and to keep the motor beyond the condition of resonance at rated speed. On the other hand the ratio α_{sd} in (3.1) important for tooth saturation. Iteration is done to get an optimum value for all these ratios in order to meet the torque requirement. These ratios are set with an initial guess and finalized by back and forth iteration.

3.2.2 Envelope Sizing

Two envelope dimensions of the machine geometry are the air gap radius to the rotor R_g and the axial length of the stack L_{stk}. An initial estimate of air gap radius to the rotor is obtained from the rotor hoop stress and the rated speed of the machine as [22]

$$R_g = \frac{1}{\omega_{rated}} \sqrt{\frac{T_s}{K_h}}, \tag{3.2}$$

where T_s is the hoop stress and K_h *is* the hoop stress constant, which is a function of the material property and few design ratios. R_g obtained from this relation gives the maximum allowable dimension for rotor radius to the air gap.

Another important design parameter is the rotor torque density $T_{e\rho}$, which depends on the saturation flux density (B_{sat}) of the rotor iron, the type of enclosure, and the cooling process employed in a particular application. Again it varies inversely with the stack length as

$$L_{stk} = \frac{P_{\max}}{\pi \omega_{corner} R_g^2 T_{e\rho}}. \tag{3.3}$$

The mean torque density calculated during design iterations is obtained from

$$T_{density} = K_t \frac{J_{rms} A_{wn} B_{sat} STF n_{ser} n_{par}}{R_g}. \tag{3.4}$$

Here, K_t is a constant containing the ratios between the peak and rms values of phase current and torque. J_{rms} is the rms current density that affects a number of design outputs.

The mean torque density should be greater than the rotor torque density T_{ep}, which should be checked during design iterations.

The average torque produced by the machine is proportional to the air gap radius (*i.e.* rotor radius) squared and to the stack length. Using the iteration process in CAD tools these parameters are determined to meet certain torque-speed-power requirements.

3.2.3 Stator and Rotor Sizing

Once the rotor radius to air gap (R_g) is determined, all other radial dimensions of rotor and stator geometry can be found as a function of R_g and the allowable air gap flux density B_g. The radial depth of stator back iron w_{bi} (also used as y_s), the stator tooth width w_{tb}, and the air gap flux Φ_g is given as

$$w_{bi} = \frac{\phi_g}{2B_{\max} Stf L_{stk}} , \qquad w_{tb} = \frac{2}{N_{sp}} w_{bi} ,$$

$$\phi_g = B_g A_g , \qquad B_g = \frac{B_r}{1+\mu_r \frac{g_e}{l_m}} \tag{3.5}$$

The stator radius to yoke R_{ys}, air gap radius of the rotor R_{gs}, and the outer radius of the stator R_{out} are expressed as a function of the design ratios and rotor dimensions as

$$R_{ys} = R_{out} - w_{bi} , \qquad R_{gs} = R_g + g = R_{ys} - d_s ,$$

$$R_{out} = \alpha_{routrg} R_g \qquad d_s = d_1 + d_2 + d_3 \tag{3.6}$$

The selection of the tooth width (w_{tb}) depends on the property of the stator lamination material and the maximum value of the flux density produced in the air gap. The value is chosen such that the tooth doesn't saturate which then can add torque ripple.

Another important parameter is the slot opening, w_s. To minimize the value of cogging torque, the slot opening parameter needs to be minimized also. Care should be taken not to make w_s too small, which can lead to slot leakage of the flux and consequently decrease the torque output level. Slot opening is also limited by the winding capability.

3.2.4 RMS Current Density

The rms current density is chosen such that it fulfils the design constraint $A_{pm} \geq A_{pe}$, where the area products A_{pm} and A_{pe} represent the mechanical and electrical loading of the machine. The value of J_{rms} ranges from 2500~6000 A/m^2 depending on the cooling system. The mechanical and electrical area products are given as

$$A_{pm} = R_g L_{stk} N_p A_{slot} \quad , \quad A_{pe} = \frac{3P_{\max}}{2Stf\eta K_{eff} B_{sat} J_{rms} w_{bi} N_s k_{cu}} \tag{3.7}$$

The maximum power output P_{max} and the slot area A_{slot} can be expressed as

$$P_{max} = (V_{bus} I_{coil})\, pf.\eta \ , \quad A_{slot} = \frac{\pi(R_{sy}^2 - R_{gs}^2) - N_s w_{tb} d_s}{N_s} \tag{3.8}$$

where pf and η are the power factor and efficiency of the machine. Bus voltage, V_{bus} expressed in terms of geometry and parameters is

$$V_{bus} = \frac{2}{3} n_s N_s B_{\max} R_g L_{stk} stf \omega_{mcorn} \tag{3.9}$$

Therefore, $P_{\max} = \left(\frac{2}{3} n_s N_s B_{\max} R_g L_{stk} stf \omega_{mcorn}\right) I_{coil}.pf.\eta$

However, $I_{coil} \times n_s = A_{slot} \times k_{eff} \times J_{rms}$;

This gives

$$P_{\max} = \left(\frac{2}{3} N_s B_{\max} R_g L_{stk} stf\omega_{mcorn}\right) A_{slot}.k_{eff}.pf.\eta$$
$$\Rightarrow R_g L_{stk} A_w = \frac{3P_{\max}}{2\omega_{mcorn}} \frac{1}{N_s.B_{\max}.stf.k_{eff}.\eta.J_{rms}.pf} \quad (3.10)$$

The left hand side of the above expression (Eq. 3.10) is the 'mechanical area product' A_{pm} representing the product of the flux passage area and the slot area. The right hand side is the electrical area product A_{pe}. The design constraint is $A_{pm} \geq A_{pe}$.

3.2.5 Computation of Maximum Number of Turns in the Slot

The rms value of coil current I_{coil} is derived from the expression for maximum power given in (3.10). Maximum number of turns in the slot n_s is then found out as

$$n_s = \frac{A_{slot}.k_{eff}.J_{rms}}{I_{coil}} \quad . \quad (3.11)$$

The per phase peak current I_{peak} is related to coil rms current as

$$I_{peak} = I_{coil} \times \sqrt{\frac{3}{2}} \quad (3.12)$$

Maximum allowable slot fill factor based on the winding requirements must be checked prior to determining the number of turns per slot. Therefore, the effective slot area should be used to calculate the number of turns and the maximum amplitude of coil current. Multiplying the slot area by slot fill factor gives the effective area of winding.

$$A_{slot,eff} = A_{slot}.k_{eff} \quad (3.13)$$

Here, k_{eff} is the slot fill factor expressed as a percentage of the total slot area. This factor depends on the size and shape of the conductor and type of winding mechanism (needle, insert, or segmented winding etc.). A conservative estimate for slot fill factor is between 60% to 70% for needle type of winding with round wire. Care should be taken while maximizing the slot fill either by reducing the wire diameter or by increasing the number of conductors, since both methods will increase the phase resistance (section 3.2.8).

3.2.6 Calculation of Maximum Demagnetization Current I_{demag}

The maximum stator current that tends to demagnetize the magnet is defined as I_{demag}. Application of Ampere's law around a magnetic flux line embracing the ampere-turns per pole gives the value of the demagnetizing MMF. If H_d is the maximum negative field which can be withstood in the magnet, then I_{demag} is given by [39]

$$I_{demag} = \left[\frac{1000}{4\pi \times 39.37}\right] \times \frac{8N_m(l_m + g)H_d}{z_1} = 2.02 \times \frac{8N_m(l_m + g)H_d}{z_1} \tag{3.14}$$

Here, z_1 is the total no. of conductors actually carrying current and $z_1 = 4N_{ph} = (2/3)n_sN_s$; the design constraint is: $I_{peak} < I_{demag}$

3.2.7 Choice of Magnet and Magnet Thickness l_m:

The flux in a PM motor is established by the magnets. The torque is proportional to the current and the flux, while the no-load speed is proportional to the voltage and inversely proportional to the flux. So, the flux is clearly the most important parameter in the design. The choice of the magnets could be anything from simple less expensive ferrites to a high energy Neodymium-Iron-Boron as mentioned in chapter I.

The characteristics of a permanent magnet are shown graphically in Fig. 3.4. It shows the relations between magnet flux and MMF, along with relating flux density with magnetizing force. The amount of flux that can be produced in an infinitely permeable material expresses the maximum available flux from the magnet is known as remnant flux Φ_r. The external demagnetizing MMF that must be applied to suppress all of the magnet flux is known as coercive MMF, F_c.

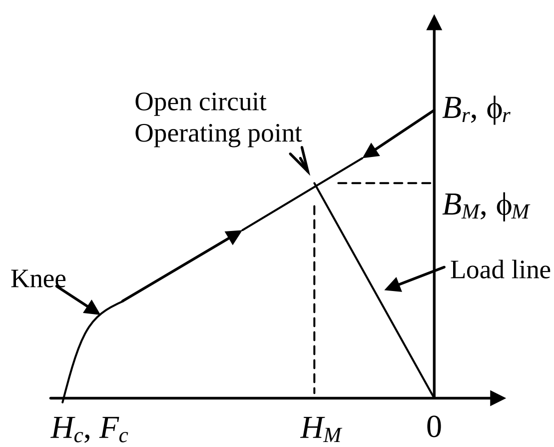

Figure 3.4: Flux/MMF and B-H characteristics of permanent magnet.

The remnant flux Φ_r and the coercive MMF F_c depend not only on the material properties, but also on the dimensions of the magnet, which makes the relationship more complicated than the simple magnetic equivalent circuit. Φ_r is expressed as

$$\Phi_r = B_r A_M \tag{3.15}$$

where A_M is the magnet pole area and B_r is the remnant flux density. A_M is calculated using the inside arc length of the magnet as Eq. 3.16a.

$$A_M = \tau_p L_{stk} \tag{3.16a}$$

The material property associated with F_c is the coercive magnetizing force or coercivity H_c. H_c is related to F_c as

$$F_c = H_c l_m \tag{3.16b}$$

where l_m is the magnet length in the direction of magnetization or magnet thickness and τ_p is the magnet arc length. The magnet's operating point generally moves reversibly up and down the linear part of the characteristic in Fig. 3.4. This characteristic is called the demagnetization characteristic and its slope is recoil permeability, μ_{rec}.

Permeance Coefficient (PC):

The airgap applies a static demagnetizing field to the magnet, causing it to operate below its remnant flux-density. With no current in the phase windings, the operating point is typically at the point labeled open-circuit in Fig. 3.4 with magnet flux density B_M of the order of 0.7-0.95 times B_r. The line from the origin through the open-circuit operating point is called the 'load-line'. The slope of the load-line is the permeance coefficient, (*PC*). the permeance coefficient is typically in the range of (5-15).

$$\mathrm{PC} = \frac{B_M}{\mu_0 H_M} \tag{3.17}$$

Fig. 3.5 shows the magnetic equivalent circuit of one pole. The main flux or airgap flux Φ_g crosses the airgap and links the coils of the phase windings. The magnet flux Φ_M is the flux passing through the magnet and the leakage flux Φ_L is the part of magnet flux that fails to link the phase windings. Φ_g and Φ_L are related to each other by a leakage coefficient f_{lkg}

$$f_{lkg} = \frac{\Phi_g}{\Phi_M} = \frac{\Phi_g}{\Phi_g + \Phi_L} \tag{3.18}$$

The leakage coefficient is less than unity and its value depends on the configuration of the motor. A typical “rule of thumb” value for most motors is 0.9.

The airgap flux density B_g is related to B_M as

$$B_g = \mu_0 H_g = \frac{\phi_g}{A_g} = \frac{f_{lkg}\phi_M}{A_g} = \frac{f_{lkg} A_M B_M}{A_g} \tag{3.19}$$

where H_g is the magnetic field in the airgap and A_g is the pole area at the airgap. Applying Ampere’s Law in a single flux path, the following can be written

$$2H_M l_m + 2H_g g = 0 \quad \Rightarrow H_M l_m = -H_g g \tag{3.20}$$

From the above two equations, the following can be derived

$$\mathrm{PC} = \frac{B_M}{\mu_0 H_M} = \frac{1}{f_{lkg}} \times \frac{A_g}{A_M} \times \frac{l_m}{g} \tag{3.21}$$

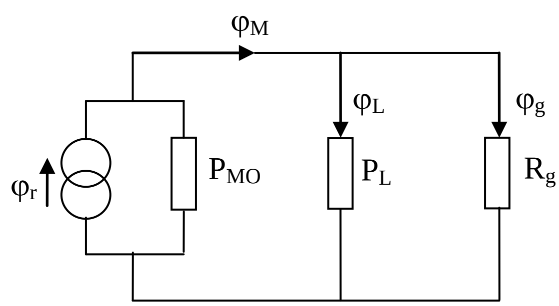

Figure 3.5: Magnetic equivalent circuit for one pole.

P_{MO} in Fig. 3.5 is the magnet internal permeance given by

$$P_{MO} = \mu_{rec}\mu_0 \frac{A_M}{l_m} \tag{3.22}$$

First Estimate of Magnet Thickness

Since higher values of PC are desirable for operating as close as possible to B_r, magnet thickness l_m has to be very large compared to airgap length g. But increasing l_m results in increased airgap radius, which may be constrained to some particular value.

A rough first estimate of magnet thickness is about ten times the airgap length. This method of first approximation applies to the use of high-coercivity magnets such as those made of ferrites and rare-earths materials.

The ratio between A_M and A_g can be determined from the first estimate of l_m, the 'rule of thumb' value of 0.9 for f_{lkg}, and the designer's choice of permeance coefficient (PC). This ratio can be expressed as

$$\frac{A_M}{A_g} = \frac{\beta_M (R_g - l_m) L_{stk}}{\beta_M R_g L_{stk}} = \frac{R_g - l_m}{R_g} \tag{3.23}$$

3.2.8 Computation of Phase Resistance

Length of mean turn is the length of the stack plus the end turn and is given by

$$L_{meanturn} = \left[L_{stk} + \frac{2\pi}{N_m} \frac{(R_{sy} + R_{gs})}{2} \right] \tag{3.24}$$

Per phase resistance is then calculated based on the mean turn length, number of phases and conductor resistivity ρ_{res}, which depends solely on conductor size. The per phase resistance is given by

$$R_{phase} = \frac{12.N_{ph}^2.L_{meanturn}.\rho_{res}}{(A_{slot}.k_{eff}.k_{CU}).N_s} \tag{3.25}$$

3.2.9 Number of Phases and Slot/Pole Combinations

The number of phases is mostly application specific. Three phase motors are by far the most common choice for all but the lowest power levels. Common to AC motors, three phase motors have extremely good utilization of copper, iron, magnet, insulating materials and silicon for a given output power. Although the utilization can theoretically be argued to be higher in motors of higher phase numbers, the gains would be offset by the increased number of leads and transistors, which increases cost and may severely compromise reliability.

The maximum number of poles is restricted by the maximum operating speed of the machine to limit the switching losses in the inverter. Again the pole number has to be in pair. The number of slots has to be an integer multiple of number of phases. The selection of number of stator slots for a given number of poles is crucial to have the minimum effect of cogging torque.

Torque of a brushless PM motor with one slot per pole per phase is approximately given by [18]

$$\tau_{mean} = 2n_s N_m R_g B_g L_{stk} I_{coil} \tag{3.26}$$

where N_m is the number of magnet poles. This equation suggests that increasing the number of magnet poles increases the torque generated by the motor. A basic rule of thumb is that the number of poles should be inversely proportional to the maximum speed of rotation. The reason, of course, is to limit the commutation frequency to avoid excessive switching losses in the transistors and iron losses in the stator. For very high speeds, two- and four-pole motors are preferred. If smooth torque is required at low speed, such as in a DC torque motor, a larger number of poles should be selected [40]. Yet another consequence of increasing the number of magnet poles is that the required rotor and stator back iron thickness decreases since the amount of flux to be passed by the back iron is reduced. As a result, the overall diameter can be reduced by increasing the number of poles [41]. Another important issue regarding the number of poles has to do with cost. Usually the greater the number of poles, the greater is the cost in magnets and labor for fabrication.

One of the primary constraints on PM stator design is that the total number of stator slots is to be some even integer multiple of the number of phases. There are many combinations of slot- and pole-numbers that can be used effectively [29]. With a large number of slots/pole, the cogging torque is inherently reduced by the fact that the relative permeance variation seen by the magnet is reduced as it successively covers and uncovers the slots one at a time. Also the coil-winding easiness is an important factor for the number of slots or poles. If there is one coil per pole per phase (say, in case of 24 slots and 8 poles), it is then possible to insert all the coils into the stator in one stroke of the machine, which certainly speeds up productions [29].

As suggested in [41], the stator back iron thickness y_s is determined by the solution of the magnetic circuit. The flux from each magnet splits equally in both the stator and rotor back irons and is coupled to the adjacent magnets. Thus, the back iron must support one-half of the air gap flux Φ_g, i.e., the back iron flux is $\Phi_s = \Phi_g/2$. If the flux density allowed in the back iron is $B_{\max}$, then the back iron width is

$$y_s = \frac{\Phi_g}{(2B_{\max} L_{stk})Stf} \tag{3.27}$$

Here *Stf is* the lamination stacking factor. The typical value between 0.93 to 0.97 is used for *Stf* .

An example design is presented in the following section that has been developed analytically through the use of all the design equations and constraints discussed so far in this chapter.

3.2.10 Example Design

The stator ampere-turns, rotor magnetization and the processing of stator steel have effect on the torque ripple of a PMSM [24]. Reduction in the torque ripple and cogging torque of this type of motors is very essential for certain applications such as electrical power steering of automobiles. Core shape optimization to reduce cogging torque in PM motor has been presented in [42] using reluctance network method and genetic algorithm.

The design constraints set for this research are the maximum outer diameter of the stator, the allowable axial length or the stack length of the rotor and the stator laminations and is given in the dimensional requirements section of Table 3.1. Also, the air gap flux density or allowable flux density through the slot tooth is constrained to avoid excessive saturation.

The systematic design approach described in this section has been followed to design a surface mounted PMSM. The effects of changing the parameters, configuration and dimensional design ratios are shown with respect to a 3-phase, ¾ hp PMSM taken as an example design. The design iteration is carried out for the four different motor topologies namely 12-slot/10 pole, 12-slot/8-pole, 9-slot/6-pole, and 27-slot/6-pole machines for which the brief operational specifications are listed in Table 3.1.

Once the motor dimensions are set according to the requirements in Table 3.1, the next important things to validate for different motor topologies are the back emf constant K_e, line-to-line resistances R_{LL}, and the phase inductances L_{phase}. A summary of these results are listed in Table 3.2. These parameters are very close in all four motor topologies presented here as they are intended to meet similar torque-speed requirements.

Table 3.1: Requirement specifications of the 3-phase, ¾ hp PMSM as an example design

Torque-speed-power Specifications		
Maximum average torque, Nm	5.5	At least
Corner /base speed, rpm	1000	Minimum
Rated maximum speed, rpm	4000	At least
Maximum constant power, watts	600	At and beyond base speed
Dimensional requirements		
Maximum outer radius,mm	95	Maximum
Allowable axial length, mm	59	Maximum
Requirements of critical issues		
Cogging torque, mNm (p-p)	10	Maximum
Torque ripple (% of average torque)	4%	Maximum
BEMF harmonics (5^{th}, 7^{th}, 11^{th} etc as % of fundamental)	0.5%	Maximum

Table 3.2: Verification of design parameters

Parameters	12-slot/10-pole	12-slot/8-pole	9-slot/6-pole	27-slot/6-pole
K_e	0.08	0.073	0.075	0.076
R_{L-L} (mΩ)	21.6	21.4	18.7	18.1
L_{phase} (mH)	0.081	0.086	0.131	0.12

Comparative analyses of several static performances for the motor topologies selected for this research are done with motor design tool PC BDC of SPEED. The design requirements have been verified in SPEED (Fig. 3.6) for the different motor topologies selected with the same envelope dimensions for this research. The significant differences in the amplitude and frequency of cogging torque [Fig. 3.7a] with variation in motor topology are evident. The value of cogging torque as well as torque ripple can

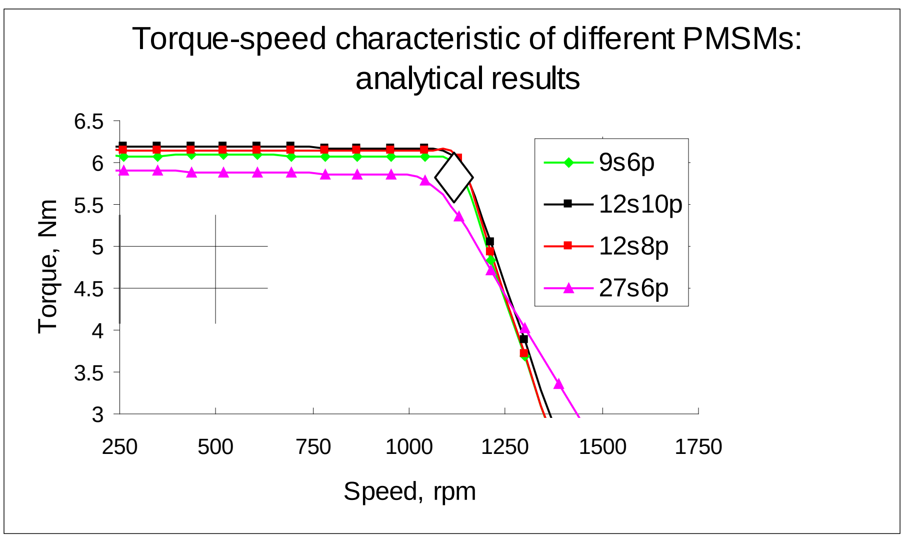

(a)

Figure 3.6: Several motor topologies verified with their characteristics (a) Torque-speed (b) Maximum power at corner speed.

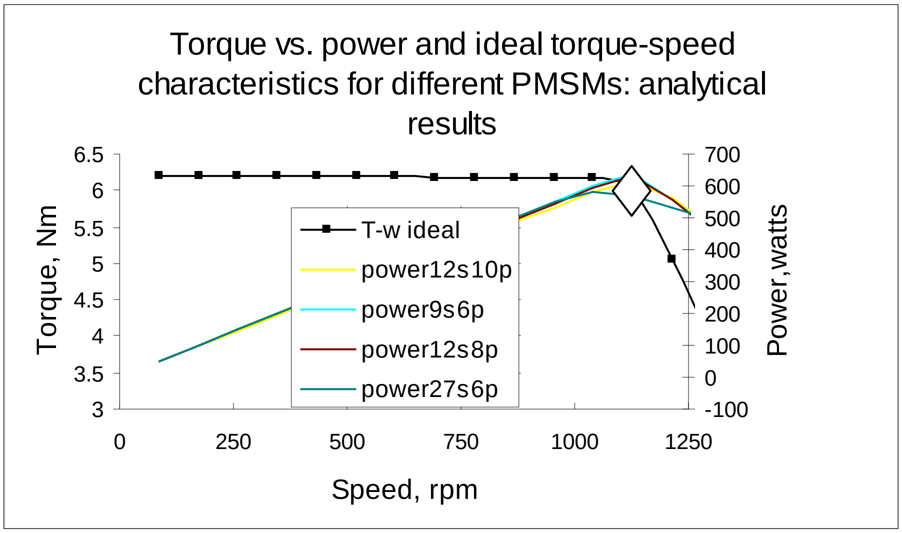

(b)

Figure 3.6: Several motor topologies verified with their characteristics (a) Torque-speed (b) Maximum power at corner speed. (continued)

further be improved by rotor pole shaping and rotor skewing. This will be shown with FE modeling in chapter IV.

3.2.11 Critical Issues

The critical issues in PMSM design are cogging torque, torque ripple and radial pressure. One or more of these issues may be very significant for a particular application.

Cogging Torque

The PMSM for certain automotive applications requires a very low cogging torque. It is evident from the results in Fig. 3.7(a) that for slot/pole combinations of 9-slot/6-pole and 12-slot/8-pole the cogging torque is more than the required value given in Table 3.1. Also, the 12-slot/10-pole and 27-slot/6-pole motor topologies have cogging torque very close to the requirements. The slot-pole combination of the motor can significantly influence the amplitude of cogging torque. For instance, the higher the value of the least common multiplier (LCM) of N_s and N_p, the lower the value of cogging torque for that motor.

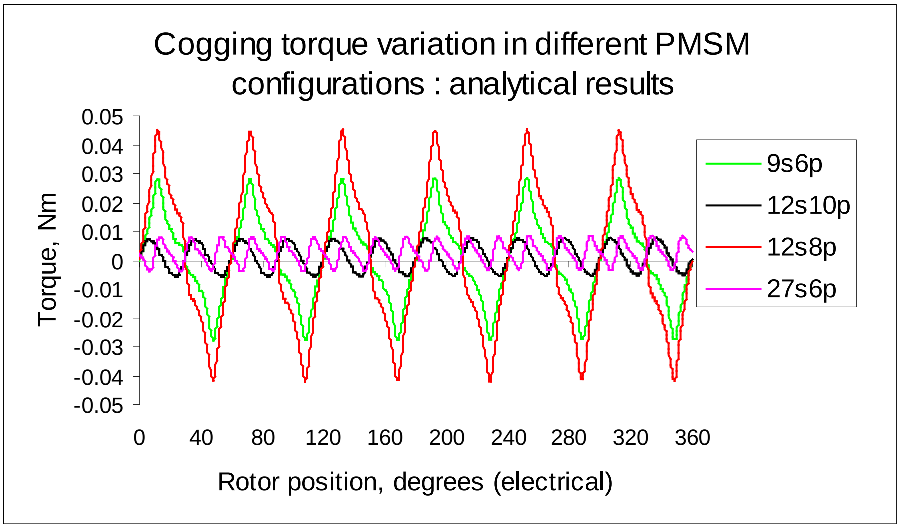

Torque Ripple

The major constituents of torque ripple are the BEMF harmonics, cogging torque, saturation and more importantly the distribution of the air-gap flux density. The selection of tooth width and tooth height in relation to the maximum value of air gap flux density and the type and shape of the magnet is critical to keep the torque ripple level to a minimum. Wider and / or longer tooth reduces saturation but wider tooth causes potential loss of winding area. To accommodate the required ampere-turns under wider tooth the tooth height or the slot depth needs to be increased. The result of increased tooth height means increased saturation. Longer tooth means larger outer radius and the outer radius of the motor should be constrained by the ratio $\alpha_{routrg} = \frac{R_{out}}{R_g}$, where the ratio needs to be minimized to maximize the mean output torque. The torque variation for all four PMSMs developed analytically is shown in Fig. 3.7(b).

Radial Pressure

From the noise and vibration requirement point of view, the radial pressure distribution on the stator tooth is critical. The mode shapes and the frequency of radial force is completely a function of the slot / pole combination of the machine. The machines where the slot number differs from the pole number by 2 (also called ‘modular’ machines) has the low order mode number as the dominant mode and suffers from vibration. These motors have different type of winding, which is known as modular winding, if the winding arrangement is changed to distributed winding (Appendix-B), the

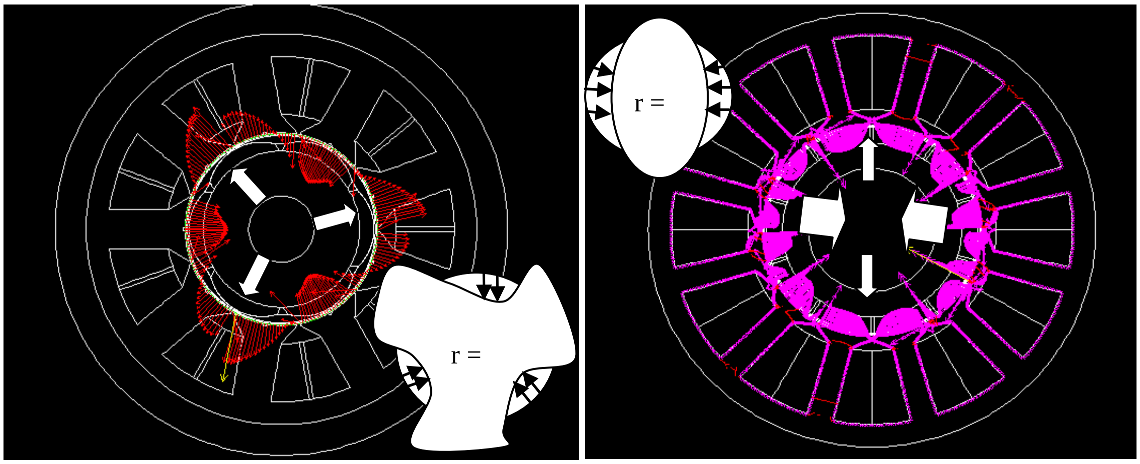

(a) (b)

Figure 3.8: Dominant mode orders in different motor topologies (a) 9-slot/6-pole motor (order 3) (b) 12-slot/10-pole motor (order 2).

dominant mode order can increase thereby reducing vibration problems [20]. The motor topologies of 9-slot/6-pole and 12-slot/8-pole shows higher cogging torque compared to 12-slot/10-pole and 27-slot/6-pole motors, but their dominant mode orders are 3 and 4, respectively. The dominant mode shapes obtained from magnetostatic analysis of FEA for 12-slot/10-pole and 9-slot/6-pole PMSMs can be found in Fig. 3.8. It can be inferred that the modular machines (i.e. 12-slot/10-pole) will be more prone to vibration than non-modular machines (9-slot/6-pole). Further details supporting this phenomenon can be found in chapter V.

Other than the selection of slot/pole combination, the natural mode frequencies of the stator geometry can be increased to reduce vibration. This can be achieved by making the stator yoke thicker with lowering the design ratio α_{yrys}. Again, a thicker yoke reduces the power density resulting in a lower utilization of the iron. Therefore, the design choice requires a tradeoff between

- cogging torque and vibration due to radial pressure in selecting the particular motor topology;
- the selection of a thinner yoke and a thicker yoke;
- the choice of modular and distributed windings.

3.3 Design Data of PMSM

The final design parameters for all four motor configurations are summarized in Table 3.3 for a 3-phase, 90A, ¾ hp PMSM. Using the dimensions, parameters and outputs from this table, the static plots of flux-linkage are checked to insure that they are satisfactory. The torque-profiles of all four motor configurations at maximum operating current obtained form analytical model simulation are given in Fig. 3.7 for both cogging torque and torque ripple. Fig. 3.9 shows the equi-flux lines in the designed 12-slot/10-pole and 9-slot/6-pole motors simulated using FEA.

The comparison of the cogging torque results obtained from the analytical model and from FEA is shown in Fig. 3.10(a) for a 12-slot/10-pole and a 12-slot/8-pole PMSM. The torque variation in a 9-slot/6-pole motor compared between analytical and the FEA results is also shown in Fig. 3.10(b). The plots confirm that the analytical model results do differ with FEA results but they are very close. All of the four designs meet the maximum torque requirement of 5.5 Nm (Fig. 3.7b), but the amount of torque ripple

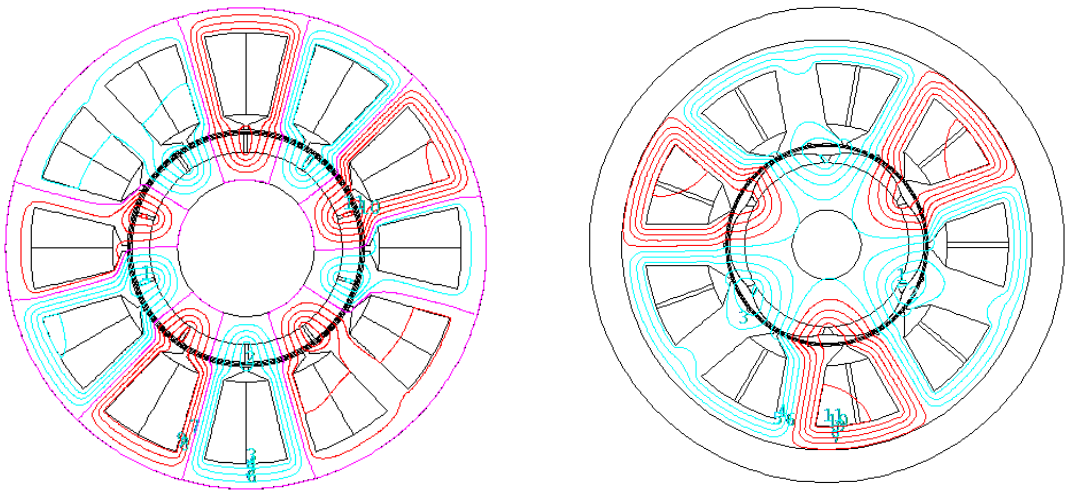

(a) 12-slot/10-pole (b) 9-slot/6-pole

Figure 3.9: Equi flux lines simulated using FEA (a) 12-slot/10-pole (b) 9-slot/6-pole machines.

Table 3.3: Dimensions, parameters and some outputs of 4-different PMSM design configuration

		Motor configuration			
Dimensior	**units**	12s/10p	12s/8p	9s/6p	27s/6p
L_{stk}	mm	59	59	59	59
R_{shaft}	mm	9	9	9	9
R_{yr}	mm	10.5	10.5	10.5	10.5
R_g	mm	22.5	22.5	22.5	22.5
l_m	mm	3	3	3	3
R_{sy}	mm	5	5	5	5
R_{out}	mm	47.5	47.5	47.5	47.5
g	mm	0.9	0.9	0.9	0.9
y_s	mm	5.5	5.5	5.5	5.5
w_{tb}	mm	**7.5**	**8**	**8**	**2.36**
w_s	mm	1	1	1	1
Parameters					
n_{par}	no. of parallel	**2**	**4**	**3**	**3**
A_{wire}	wire area, mm	0.723	0.811	0.811	0.643
TC	no. of turns	18	19	20	7
n_{sh}	wire in hand	8	3	5	9
Output					
T_{shaft}	Nm	6.07	6.04	6.02	5.72
P_{shaft}	watts	636	633	631	599
T_{cogg}	mN-m	±10	±25	±40	±10
T_{ripple}	%of average t	>8%	< 6%	< 6%	> 8%

present in these designs is more than the requirements (4% of average torque) listed in Table 3.1. Therefore, further design optimization is necessary to minimize the torque ripple. The next chapter will address these issues by appropriately adopting pole shaping and rotor skewing.

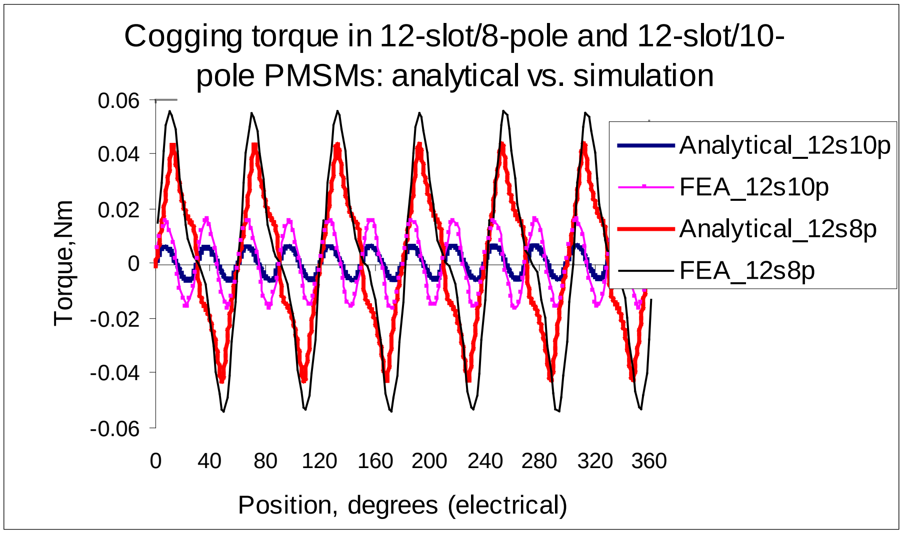

(a)

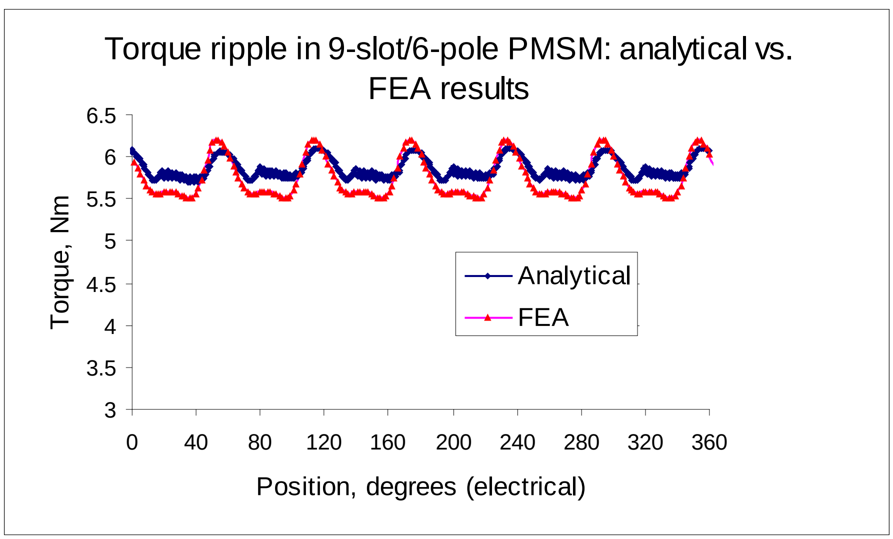

3.4 Conclusions

A comprehensive design methodology for PM machines that include FE computations has been presented in this chapter. The critical factors of torque ripple, cogging torque and radial forces have been discussed. The next chapter will present novel PMSM design techniques to minimize torque ripple. One of the contributions of this research is the pole shaping and rotor skewing techniques to reduce cogging torque and hence torque ripple. Several design techniques will be applied to manage the torque ripple issues; both test and simulation results for some of these designs are documented in the next chapter. Also, the noise and vibration analysis will be presented in detail in chapter V. A novel analytical model to predict the radial vibration and acoustic noise from the radial pressure will be presented.

CHAPTER IV

TORQUE RIPPLE AND COGGING TORQUE ANALYSIS

This chapter examines the torque ripple and cogging torque variation in surface mounted PMSMs with skewed rotor. The effect of slot/pole combinations and magnet shapes on the magnitude and harmonic content of torque waveforms in a PMSM drive have been studied. Finite element analysis (FEA) and experimental results show that for certain magnet designs and configurations the skewing with steps does not necessarily reduce the ripple in the electromagnetic torque, but may cause it to increase. The electromagnetic torque waveforms including cogging torque have been analyzed for four different PMSM configurations having the same envelop dimensions and output characteristics.

In the previous chapter design parameters for several motor topologies have been determined based on static and dynamic characteristics (torque-speed-power requirements etc) using CAD design tools. This chapter will focus on the strict requirements of cogging torque and torque ripple for an automotive application. The torque outputs will be examined using FEA tools. Several design techniques like magnet pole shaping, step skewing of the magnet etc. will be used to improve the performances by reducing cogging torque and torque ripple.

4.1 Torque Ripple and Cogging Torque

The three main components of torque in PMSM are: 1) mutual torque, which is caused by the interaction of the rotor field and stator currents, 2) reluctance torque, which is due to the rotor saliency; and 3) cogging torque, which arises from the interaction between permanent magnets and slotted iron structure. The contribution from reluctance torque in surface mounted PMSM can be ignored due to almost zero saliency. The output torque quality can be improved by reducing the torque ripple in the mutual torque that is related to the harmonic content in the BEMF. Reducing the cogging torque will also improve the output torque quality. Methods for reducing cogging torque and for minimizing the harmonic contents in mutual torque to minimize the torque ripple in PMSMs appear in [1]-[7], and [15]-[17]. Some researchers have considered the torque ripple problem in PMSM primarily from a design point of view [1]-[3], and [15] while others worked from the control side [4]-[7], [16], and [17]. Several researchers have shown that the improvement of cogging torque leads to improvement in the torque ripple [1, 3, and 15]. One of the well-known approaches to minimize cogging torque is rotor or stator skewing. Cogging or detent torque in PMSMs can be theoretically reduced to zero by the selection of optimum skew angle, which is solely a function of slot-pole combination [1].

The torque ripple variation under field weakening operation and cogging torque variation with different magnet shapes and skew schemes has been investigated. This research shows that the torque ripple can either reduce or increase after magnet skewing when step skew techniques are used. Step-skewing is a common practice in the industry adopted for ease of manufacturing and cost reduction.

This chapter presents torque waveform and cogging torque results with variations in machine configurations and magnet shapes computed using two-dimensional (2-D) FEA. Both straight magnet and skewed magnet have been used in the PMSM designs intended for automotive applications. The objective is to obtain a magnet design with skewing in a certain motor configuration that has minimum torque ripple without significant average torque reduction. The new designs are obtained with further adjustments on the basic machine designs presented earlier in chapter III.

4.2 BEMF and Torque Ripples

The PMSM has a stator with a sinusoidally distributed three-phase copper windings, while the rotor has permanent magnets. With three-phase balanced sinusoidal currents in the three-phase distributed stator windings, a sinusoidal magnetomotive force is generated in the air gap. A sinusoidal distribution of rotor flux can be established by shaping the permanent magnets and controlling their magnetization directions. The electromagnetic torque is generated on the shaft by the interaction of the stator and rotor magnetic fields. The instantaneous torque for a three-phase PMSM without magnetic saturation is given by

$$T_e = (e_a i_a + e_b i_b + e_c i_c) / \omega_r \tag{4.1}$$

where e_a, e_b ,e_c are the phase BEMFs, ω_r is the angular mechanical speed, and i_a, i_b, i_c are the phase currents. The motor can produce constant mutual torque only if the part of the mutual flux through stator windings due to the rotor field is purely sinusoidal. This also requires sinusoidal spatial distribution of either the stator windings, or of the field due to rotor magnets. In practice, the perfect sinusoidal distribution of the winding is not achievable, and the mutual flux contains several higher harmonics and causes steady state torque ripple in response to a purely sinusoidal excitation.

All three phases are excited at the same time in a PMSM drive. The phases are excited by controlling their respective switches such that the phase currents are in phase with their respective phase BEMFs to avoid any torque pulsation. The presence of harmonics in current and/or BEMF leads to torque harmonics. Even if the currents are maintained to be purely sinusoidal the BEMFs always contain some harmonics depending on the magnet shape and design and based on the saturation level of flux distribution in stator. The most commonly seen harmonics order for a 3-phase y-connected stator windings are 5^{th}, 7^{th}, 11^{th}, 13^{th}, 17^{th}, and 19^{th} etc. Again the dominant order of torque ripple is the 6^{th} order which results from the interaction of 5^{th} and 7^{th} order BEMF harmonics with the fundamental component of phase currents or vice versa. For simplicity let us assume that there is only 5^{th} order (per electrical cycle) harmonics in the BEMF. The equation of phase BEMFs with 5^{th} harmonics only, and the corresponding phase currents without any harmonics and phase advance angle γ (according to field weakening explained in chapter II) are given by the following equations

$$e_a = E_1\cos(\omega t) + E_5\cos(5\omega t); i_a = I_1\cos(\omega t - \gamma) \tag{4.2}$$

$$e_b = E_1 \cos(\omega t - 2\pi/3) + E_5 \cos(5(\omega t - 2\pi/3)); i_b = I_1 \cos(\omega t - 2\pi/3 - \gamma) \tag{4.3}$$

$$e_c = E_1 \cos(\omega t + 2\pi/3) + E_5 \cos(5(\omega t + 2\pi/3)); i_b = I_1 \cos(\omega t + 2\pi/3 - \gamma) \tag{4.4}$$

The instantaneous torque is then calculated as the sum of the products of phase BEMFs and phase currents divided by the rotational speed of the machine. This torque has both a pulsating component and a DC component.

$$\begin{aligned} T &= \frac{1}{\omega_r}[\{\frac{3}{2}E_1 I_1 \cos\gamma\} + \{\frac{3}{2}E_5 I_1 \cos(6\omega t - \gamma)\}] \\ &= T_0 \cos\gamma + T_r. \end{aligned} \tag{4.5}$$

The first term in the torque expression represents the average or DC component whereas the last term is the unwanted pulsating component. Without any harmonics or phase advancing the torque is a pure DC given by

$$T = T_0 = \frac{1}{\omega_m}\frac{3}{2}E_1 I_1. \tag{4.6}$$

Due to phase advancing the average torque is reduced by a factor of the cosine of the phase advance angle. Also, the 6^{th} order torque ripple in the above equation is a direct consequence of the 5^{th} order BEMF. The peak-to-peak torque ripple is twice that of T_r. A 5^{th} order harmonics equal to 5% of the fundamental component will thus produce a torque ripple of 10% of the average torque provided there are no other harmonics present in BEMFs and the current is a purely sinusoidal. A PMSM design objective is to limit the 5^{th} order harmonics to a small fraction of its fundamental component; the contributions from higher order harmonics like 7^{th}, 11^{th}, 13^{th} etc are kept less than that of the 5^{th} order harmonics.

The interaction between fundamental component of current and 5^{th} order harmonics of BEMF produces both 4^{th} and 6^{th} order torque ripple. In a 3-phase balanced system, 4^{th} order is cancelled out (also 2^{nd}, 8^{th}, 14^{th}, 16^{th}, 20^{th} etc.). The details of the cancellation can be found in Appendix-C. The 6^{th} order torque ripple can also be caused due to interaction of 7^{th} order BEMF and fundamental component of current where the other derivative is 8^{th} order and cancelled out in the y-connected 3-phase system. Since the 6^{th} order component is the dominant component of torque ripple, it is important to minimize the 5^{th} and 7^{th} order BEMF harmonics in most cases. Any one of these orders can be completely eliminated by selecting an optimum magnet pole arc in a particular slot/pole motor topology. In reality, total elimination of any particular BEMF harmonic from magnet design standpoint is always challenged by manufacturing tolerances of the PMs. The presence of saturation in the magnetic circuit also can cause some of these harmonics in BEMF. More on this saturation and how it affects the torque ripple is explained in section 4.8 of this chapter.

4.3 PMSM Design Choices

The airgap flux pattern which depends on the type and shape of the magnets (i.e. surface radial, surface parallel, or bread loaf etc) determines the BEMF waveform. The BEMF can be shaped to be rectangular or sinusoidal (Fig. 4.1) in any particular type of magnet by changing the pole pitch τ_p with respect to slot pitch τ_c or coil pitch. This might not produce a pure sinusoidal distribution of air gap flux and may contain significant amount of harmonics in BEMF for some motor configurations especially when the magnet poles are of uniform width all over its arc length. The flux density is made sinusoidal in those cases by shaping the two ends of the magnet such that PMs are thinner at the edges than in the center. This shaping of the surface magnets at one point will make the BEMF perfectly sinusoidal, and therefore, will reduce both the cogging torque and torque ripple.

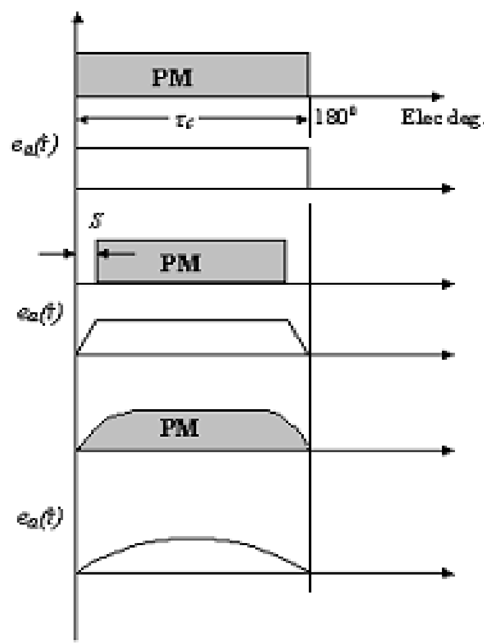

Figure 4.1: Phase BEMF shapes for different shapes of permanent magnet (i) top: $\tau_c = \tau_p$ (ii) middle: $\tau_c > \tau_p$ (iii) lower: $\tau_c = \tau_p$ and magnets thinner at edges.

4.3.1 Magnet Shapes

Both cogging torque and torque ripple varies as the pole arc length varies compared to the pole pitch length. If the arc of the magnet covers the full pole pitch, the airgap flux density as well as the average torque will be higher compared to the case when pole arc is less than the pole pitch. More so, the torque ripple and cogging torque could be worse depending on the value of maximum airgap flux density.

In addition to varying the pole arc, reshaping the PM for a fixed pole arc (magnet angle θ_m in Fig. 4.2) can also change the harmonics in the BEMF significantly; this will change torque ripples in different designs. Three different magnet shapes with a fixed magnet angle of a surface mounted PM are shown in Fig. 4.2. The bar shaped magnet shown in Fig. 4.2(a), widely known as surface radial magnet, produces more average torque compared to the magnet shapes in 4.2(b) and 4.2(c) provided all other dimensions and parameters of the motor remain the same. The loaf and petal shaped magnets shown in 4.2(b) and 4.2(c) produce more sinusoidal flux distribution in the air gap than the bar

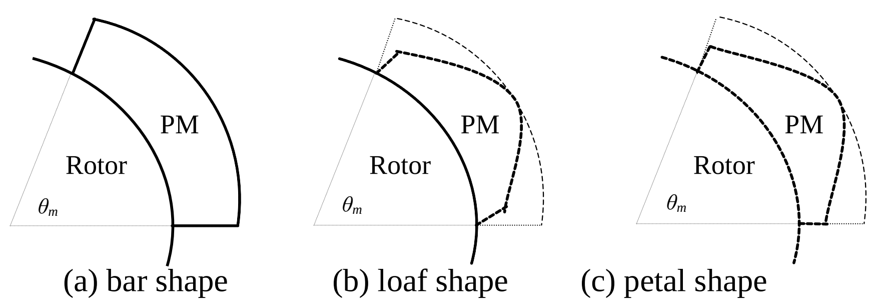

Figure 4.2: Different magnet shapes of a surface mounted PMSM.

shaped magnet, and consequently should contain fewer harmonics of the dominant orders resulting in lower torque ripple.

Again, keeping the same pole arc length, the shape of the magnet can be varied in various ways similar to Figs. 4.2(b) and 4.2(c). The flux distribution in the airgap and also the harmonics in the BEMF will be different in those cases compared to the common design choice shown in Fig. 4.2(a).

4.3.2 Geometry Selection

Slot/pole combination of a PMSM strongly influences the cogging torque and torque ripple characteristics of the machine. A smaller difference between the number of poles and the number of slots implies that there is less of a chance for complete alignment of rotor poles with stator tooth, and therefore, their cogging torque will be of smaller magnitude. The cogging torque and torque ripple have been analyzed using 2-D FEA for four PMSM configurations. The design features of these motors are given in Table 4.1. In each of the four configurations, the outer envelop dimensions and output torque requirements are kept the same. In configurations like 12-slot/10-pole, the fundamental order of cogging is 60th (LCM of pole number and slot number); the optimum skew angle required to cancel this order completely is 360º/60 or 6º mechanical. On the other hand, the fundamental cogging torque order is only 18th in the 9-slot/6-pole motor and the optimum skew angle to cancel this is 20º mechanical. Ideally, the higher the number of cogging order the lower is the amplitude of cogging torque. In the preliminary designs, it has been shown how the cogging torque and torque ripple are different in different motor configurations though all of them meet the same torque-speed requirements. It was shown in the previous chapter that the cogging torque and the torque ripple quantities were very close to the design requirements in 12-slot/10-pole and 27-slot/6-pole motors as per analytical results from CAD tool. On the other hand, these are worse in 9-slot/6-pole and 12-slot/8-pole motors. For the second type of configurations, pole shaping is one of the solutions to bring down the cogging torque and torque ripple.

Table 4.1: Four different PMSM configurations

Number of slots	12	12	9	27
Number of poles	10	8	6	6
Pole arc/pole pitch ratio	0.94	0.95	0.96	0.96
Number of cogging period in 1-slot pitch $N_{period} = \frac{N_p}{HCF\{N_s, N_p\}}$	5	2	2	2
N_{period} in 360° *m* (i.e. fundamental cogging frequency)	**60**	**24**	**18**	**54**
Optimum skew angle, $\theta_{skew} = \frac{360}{N_s N_{period}}$	6°	15°	20°	6.67°
Slot number /pole number ratio	1.2	1.5	1.5	4.5

4.4 Torque Variation with Design Choices

The variations in torque ripple and average torque with different machine configurations and magnet shapes are analyzed in this section.

4.4.1 Cogging Torque Variation with Configurations

Cogging torque of the four machine configurations selected for this research has been analyzed by FEA. The results are plotted in Fig. 4.3 for comparison. The amplitude of cogging torque is much smaller in the 12-slot/10-pole and 27-slot/6-pole configurations compared to the 12-slot/8-pole and 9-slot/6-pole configurations, as expected. A suitable slot/pole combination can be chosen to improve the torque performance of the machine.

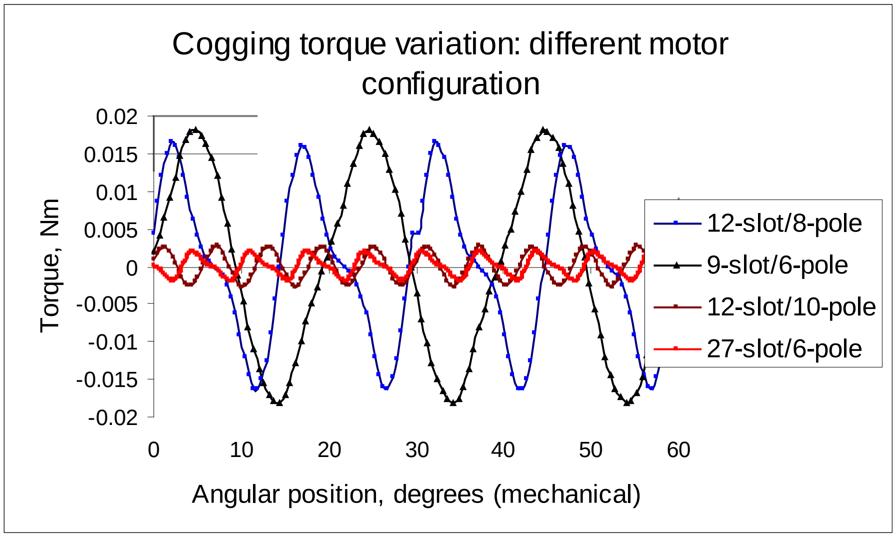

Figure 4.3: Cogging torque variation in different motor configurations.

4.4.2 Effect of Magnet Shapes

The cogging torque variation with rotor position and the peak-to-peak torque ripple results with phase advancing described in chapter II for a 12-slot/8-pole PMSM with the three magnet shapes of Fig. 4.2 are given in Fig. 4.4. All three designs have the same rotor and stator dimensions. The peak-to-peak torque ripple is higher for the bar shaped magnet compared to loaf or petal shaped ones (Fig. 4.4b), although the relative differences in cogging torque value is minimal for all three magnet designs (Fig. 4.4a).

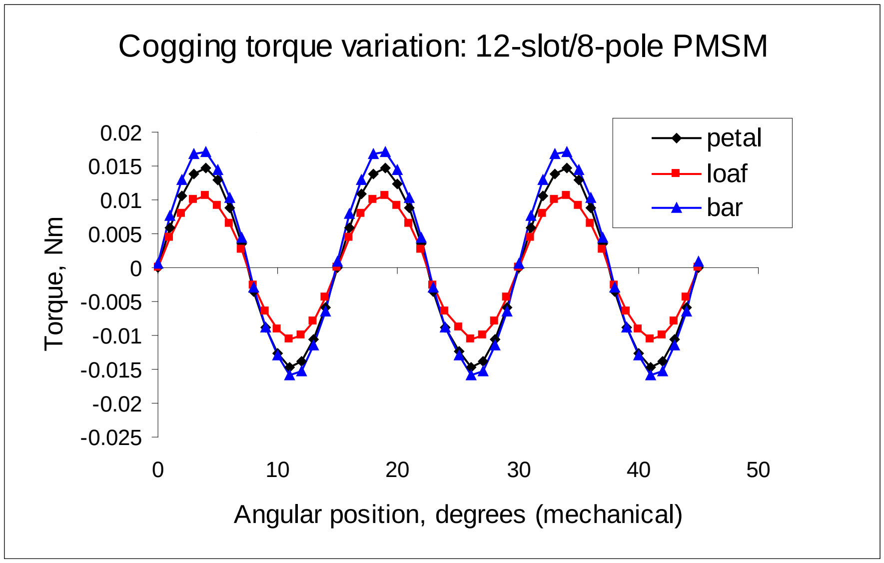

(a)

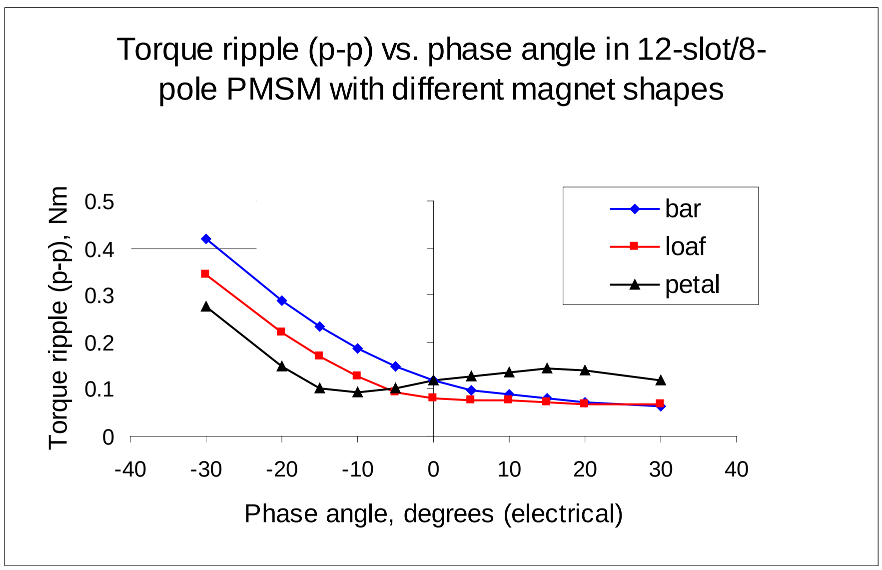

(b)

Figure 4.4: A 12-slot/8-pole PMSM performances with the bar, loaf and petal shape magnets (a) Cogging torque variations (b) Torque ripple variations.

Again, the cogging torque and torque ripple in a 12-slot/10-pole PMSM are shown in Fig. 4.5 for the three magnet shapes. The torque ripple changes are minimum with phase angle variation especially for the loaf and bar shape magnets for this configuration (Fig. 4.5(b)). The same conclusion hold true for the cogging torque (Fig. 4.5(a)).

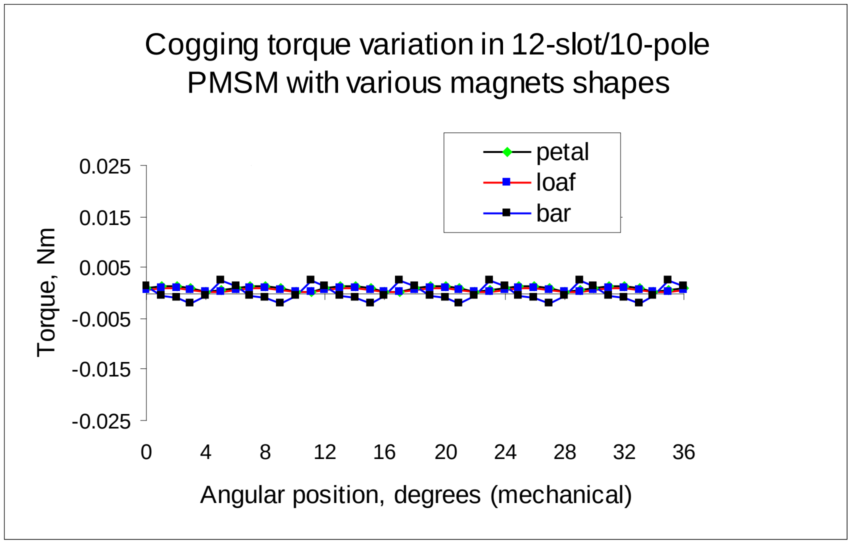

(a)

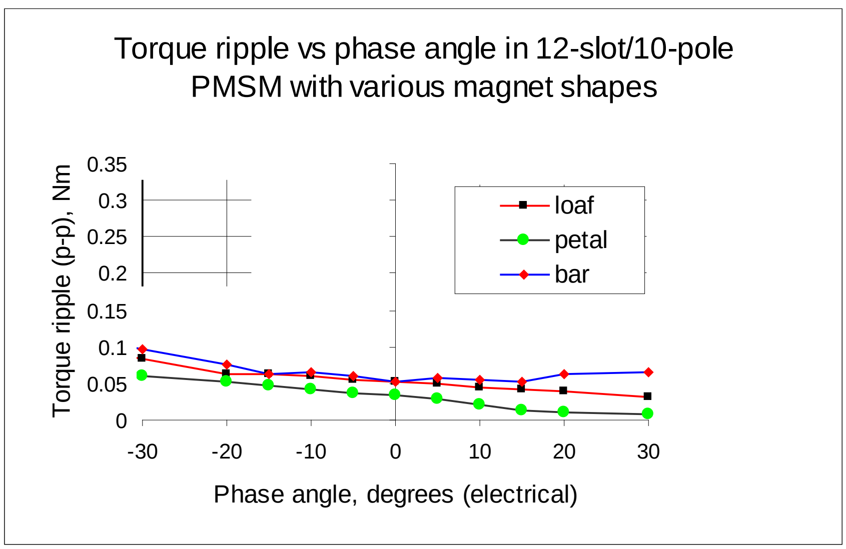

(b)

Figure 4.5: A 12-slot/10-pole PMSM performances with the petal, loaf, and bar shape magnets (a) Cogging torque variations (b) Torque ripple variations.

The 12-slot/8-pole and 12-slot/10-pole configurations fall under two distinct categories where the optimum skew angles for the two configurations are significantly different (see Table 4.1). The skew angle of a configuration indicates the available window over which the airgap reluctance can be varied. Design choices, such as rotor/stator skew, can be utilized to bring down the airgap reluctance to zero with a wider skew angle. In the case of 12-slot/10-pole and 27-slot/6-pole machines, the window is rather small (6° and 6.67°, respectively). In the case of 12-slot/8-pole and 9-slot/6-pole machines, the skew angle is quite large (15° and 20°, respectively), and consequently, the peak-to-peak torque ripple will vary significantly with phase angle variations. This is reflected in the results of torque ripple shown in Figs. 4.4 and 4.5. Therefore, torque ripple may be reduced by skewing in machines with larger optimum skew angle.

The results presented in this section are without skewing. The need for skewing in configurations with smaller skew angles is questionable judging from the relatively small cogging torque seen in Fig. 4.5(a) for the 12/10 configuration. However, skewing is still used in these types of configurations to shift the lower orders of cogging to higher orders in order to address the manufacturing tolerances.

4.4.3 Average Torque Variation

The average torque will decrease with phase advancing (either lagging or leading) due to the *d*-axis current component as explained in chapter II. The average is also less for the loaf and petal shaped magnets compared to the bar magnet. This can be observed in Fig. 4.6 with the results from a 12-slot/8-pole PMSM configuration. The results are similar for the other configurations. The average torque varies cosinusoidally with phase angles as the torque is proportional to q-axis current i_q, and with phase advance or phase lag angle γ. The average torque follows the envelope of a cosine function with varying phase advance angles.

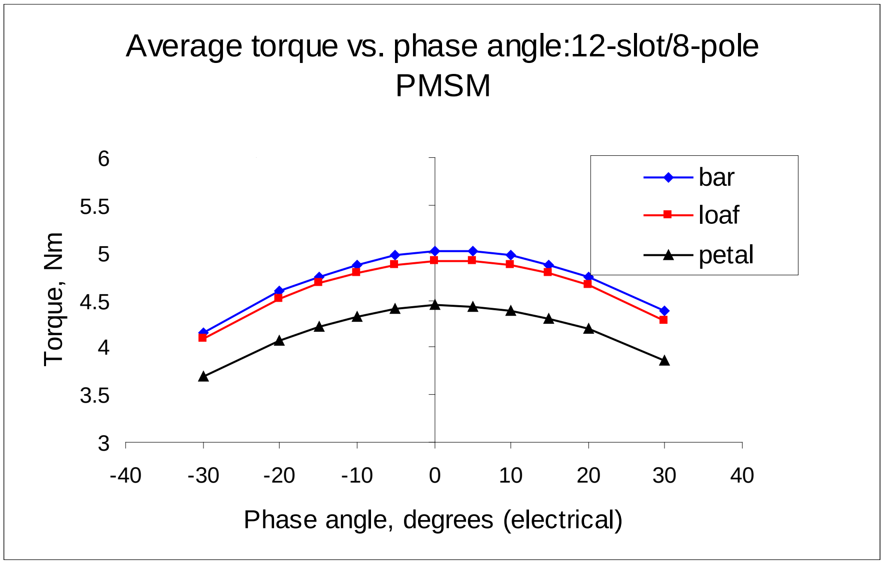

Figure 4.6: Average torque variation with phase advancing in a 12-slot/8-pole motor with the bar, loaf and petal shapes respectively.

4.5 Torque Variation with Magnet Skewing

This section discusses about the cogging torque variation with magnet skewed particularly addressing the step-wise skew techniques in relation to a 9-slot/6-pole PMSM.

4.5.1 Cogging Torque Reduction

The use of skewed magnet is an established approach of reducing cogging torque. The cogging torque is the oscillatory torque of zero average value caused by the tendency of the rotor to line up with the stator in a particular direction where the permeance of the magnetic circuit "seen" by the magnets is maximized [18]. The peak value of the cogging torque is defined by such parameters as slot opening/ slot pitch ratio, magnet strength, and air gap length, while its profile could be altered by varying the pole arc/pole pitch ratio. Cogging torque can be minimized by careful selection of some of these parameters, but this approach is limited by practical and performance constraints.

A more common approach for cogging torque minimization is by skewing the rotor magnet or the stator pole. Bolognani *et al.* [1] showed the dependence of the cogging waveform period during a rotation of a slot pitch with the number of slots and poles, and also the relationship of the torque magnitude to the period. Hwang *et al.* [2] extended the research to show that the cogging torque can theoretically be reduced to zero by skewing the rotor magnet with an angle equal to one half of a slot pitch.

4.5.2 Step Skewing

Skewing can be continuous or step-wise. This research focuses on step-skew motors; the PMSMs available for experiments are also of step-skew type. A three-step skew is a good compromise between manufacturing complexity and performance. The three-step skew scheme is shown in Fig. 4.7. The arrangement provides a gradual transition of cogging as the magnet moves under a stator tooth.

A three-step skewed motor is modeled as a motor with three axial slices each shifted by the skew angle. The centre piece is considered to have zero phase angle ($\gamma = 0$), while the other two pieces (lagging and leading pieces) have positive and negative phase angles of γ.

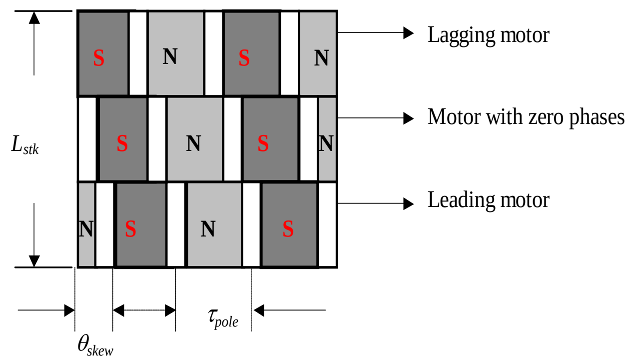

Figure 4.7: Three-step magnet skew scheme.

4.5.3 Cogging Torque Results

FE results in Fig. 4.8(a) shows the cogging torque reduction with the skew angle in case of a 3-step magnet skew in a 9-slot/6-pole PMSM. The legend in the figure indicates the skew angle. A 21^0 skew angle reduces the cogging torque significantly, since the optimum skew angle for this configuration is 20^0. In the ideal case, the fundamental component (18^{th} in this particular case) of cogging torque will be eliminated completely for a 3-step skew with skew angle of 20^0 . This requires the magnet segments to be placed 6.67^0 displaced radially from each other.

The simulations for cogging torque obtained for a 9-slot/6-pole motor geometry with different skew angles in a skewed rotor proved that the optimum selection of skew angle could eliminate cogging torque for a particular geometry (Fig. 4.8a). The optimum skew angle is a function of stator and rotor poles only. Again, the more the numbers of magnet modules (also known as number of steps in skew) in a skewed magnet, the less are the amplitude of cogging torque (Fig. 4.8b). There is always a trade off between the cost and the relative improvements in cogging with the number of modules increased in the skewed magnet. Common trend in the motor industry is to have 2-step or 3-step skew. Cogging torque is always lowered with skewed rotor motor compared to straight rotor motor irrespective of the skew steps and the geometry (*i.e.* slot-pole variation).

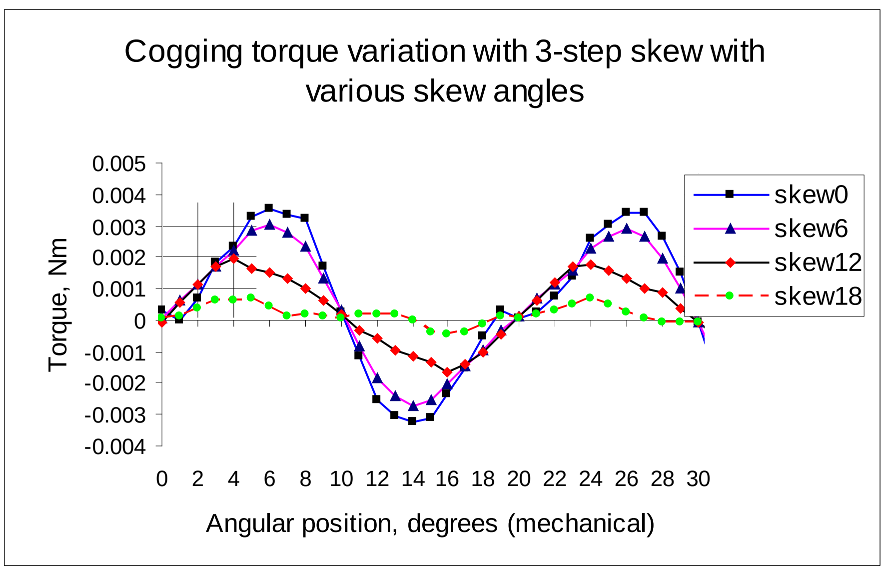

(a)

Figure 4.8: Cogging torque variation for 9-slot/6-pole PMSM (a) with various skew angles; skew0: no skew, skew6: 6 degree, skew12: 12 degree, skew21: 21 degree (b) with various number of magnet modules.

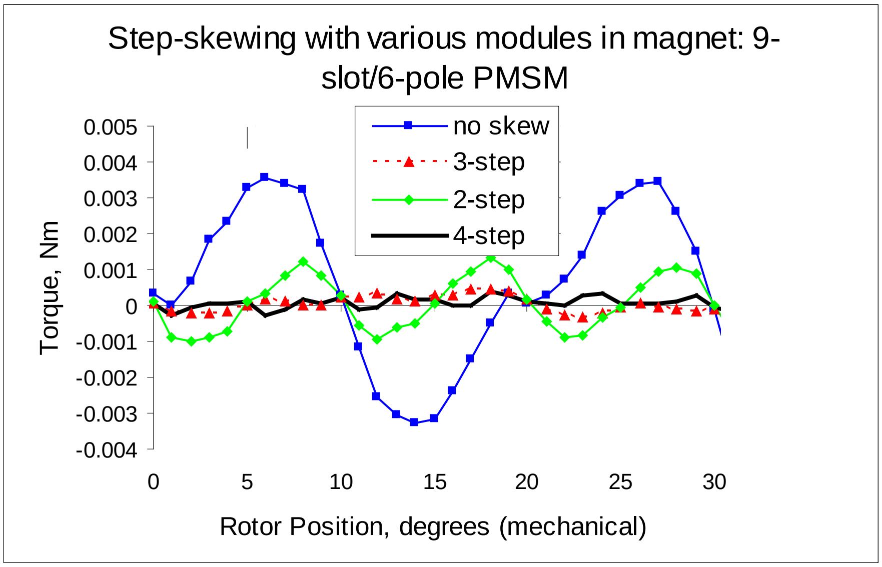

(b)

Figure 4.8: Cogging torque variation for 9-slot/6-pole PMSM (a) with various skew angles; skew0: no skew, skew6: 6 degree, skew12: 12 degree, skew21: 21 degree (b) with various number of magnet modules. (continued)

4.6 Skewing with Variation in Magnet Shapes

Torque ripple reduction is a challenging task for both the motor designer and the control engineer. Methods based on the motor design like skewing, magnet position shifting, special windings etc. are more efficient than control based methods. The main disadvantages of the design-based methods are the reduction in average torque and the increased complexity of motor construction, and hence increased overall cost.

The torque ripple in a skewed motor can be calculated using the concept of phase advancing and the results of FE analysis. A motor with three-step magnet skew can be considered as a combination of three motors operating with three different phase angles. If the effective skew angle is θ_{skew}, then the torque of a three-step skewed motor without any phase advancing can be obtained by taking the average of the torques produced by three non-skewed motors: One motor operating at $\theta_{skew}/3$ lagging, one without phase advancing and the other at $\theta_{skew}/3$ leading. Phase advance angles are represented in electrical quantities obtained by multiplying the skew angle with the number of pole-pairs for the respective motor. The overall torque ripple in a skewed motor is reduced or increased depending on the decrease or increase of torque ripples in the lagging and leading motors compared to the motor with zero phase angle advancing.

The torque ripple variation results of Fig. 4.4(b) for the non-skewed 12-slot/8-pole motors with phase advancing (both leading and lagging phase angles) can be used to explain how torque ripple results for skewed motors can be obtained. The optimum value of skew angle for a theoretical zero cogging torque for this motor is 15° (mechanical). A three-step skewed motor will thus have a torque ripple equal to the average torque ripples at ±5° (mechanical) or ±20° (electrical), and at 0° (mechanical/electrical). For 12-slot/8-pole PMSMs with bar and loaf shaped magnets, the averaged torque ripple will be higher than the ripple at zero phase, whereas the average will be slightly lower in the machine with petal shaped magnets. Therefore, the results of torque ripple vs. phase angle predict which magnet designs will reduce torque ripple with skewing. It can also be concluded that skewing does not always reduce the torque ripple, although cogging torque is reduced. There are certain configurations (like 12-slot/10-pole) and magnet shapes (like bar shapes in 9-slot/6-pole or 12-slot/8-pole motors) for which torque ripple can't be improved significantly by magnet skew. The results of 12-slot/10-pole motor given in Fig. 4.5(b) show that torque ripple variation remains almost the same with phase advance angle variations for all of the three magnet shapes used.

The peak-to-peak torque ripples as a function of phase angles for two different loaf magnet shapes for a 9-slot/6-pole PMSM are shown in Fig. 4.9. The results of the non-skewed motor can be evaluated to see whether skewing will help reduce torque ripple or not. The torque ripple change is more significant with lagging phase angles (injecting more magnetization by adding positive i_d), and is almost constant with leading phase angles (or field weakening). The most significant result is at the minimum point of torque ripple. The plot in Fig. 4.9 shows this point right at phase zero for loaf-A magnet design and at -20° (electrical) phase lagging for loaf-B magnet design.

The likelihood of obtaining lower torque ripple in the skewed motor depends on where the minimum ripple point is located and the magnitude of the ripple at this position. This minimum point should be close to the optimum skew angle for a good design.

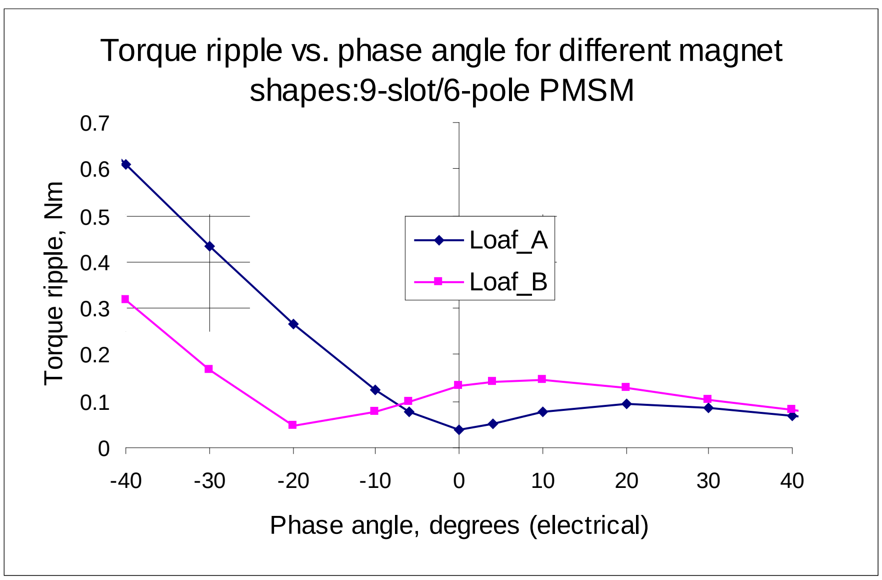

Figure 4.9: Torque ripples variation for two different magnet designs, 9-slot/6-pole PMSM.

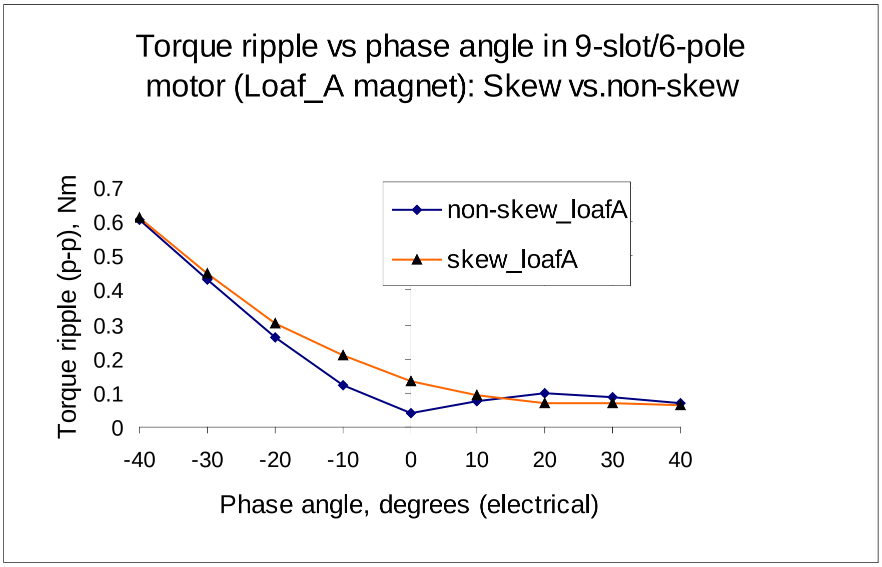

(a)

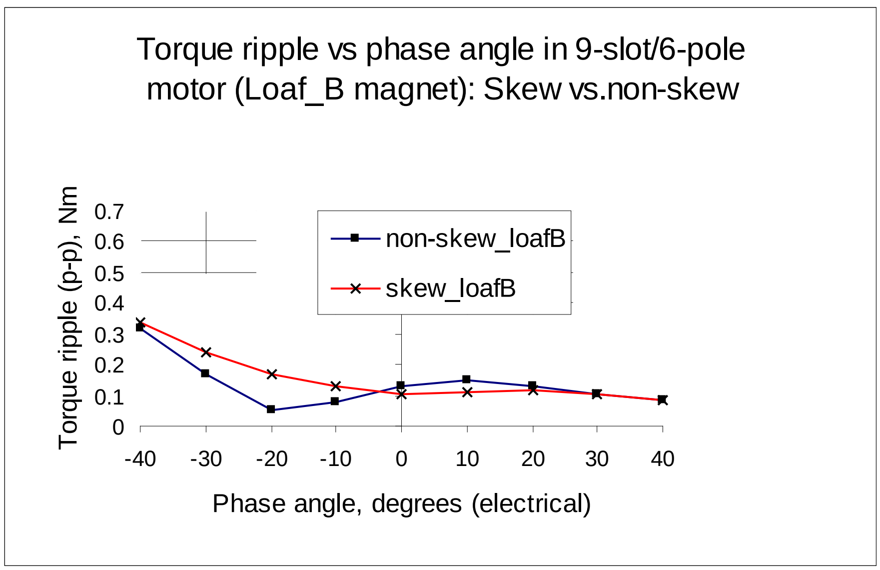

(b)

Figure 4.10: Torque ripple characteristics of a 9-slot/6-pole PMSM with skew and non-skew (a) loaf-A magnet; (b) loaf-B magnet.

The torque ripple pattern for the skewed motor (with an optimum skew angle of 20 deg.) has been calculated for both the magnet designs according to the techniques described earlier. The torque ripple for skewed motor is higher than the non-skewed case with loaf-A shaped magnet at the operating point of zero phase angle (Fig. 4.10(a), while the case is opposite for the loaf-B shaped magnet (Fig. 4.10(b)). The location of the torque ripple minimum in the non-skew motor is the key in determining whether torque ripple can be reduced or not in a certain design.

4.7 BEMF and Torque Ripple Harmonics

The spectrum analyses for the torque ripple and the phase BEMFs have been obtained to study the effect of harmonics in the magnitude of torque ripple. The dominant BEMF harmonics of the 5^{th}, 7^{th}, 11^{th}, and 13^{th} orders have been considered (Fig. 4.11). The harmonics are obtained at a very low speed of 1deg./sec of the motor. Assuming a pure sinusoidal phase current distribution, the torque will contain mostly the 6^{th}, 12^{th}, and 18^{th} order harmonics due to these BEMF harmonics. The 6^{th} order harmonics of the torque ripple will not necessarily be proportional to the contribution of 5^{th} and 7^{th} order BEMF harmonics due to magnetic saturation in the machine. Some higher order harmonics may follow the envelope of the torque ripple (p-p) waveform when plotted against phase angle.

The torque ripple harmonics of 6^{th}, 12^{th}, and 18^{th} orders for a 9-slot/6-pole motor with the two loaf shaped magnets, loaf_A and loaf_B, are shown in Fig. 4.12 and Fig. 4.13, respectively. The phase advance angles in these figures corresponds to -40°, -30°,

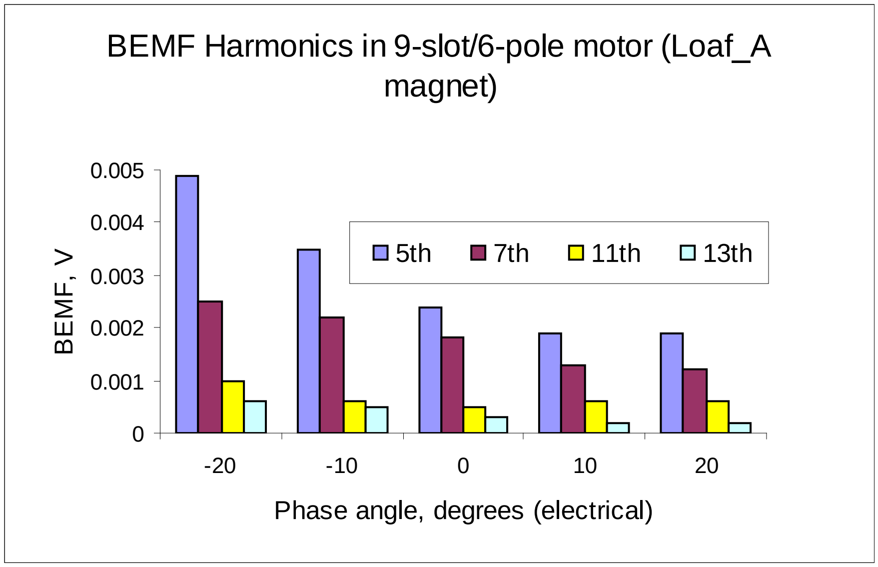

(a)

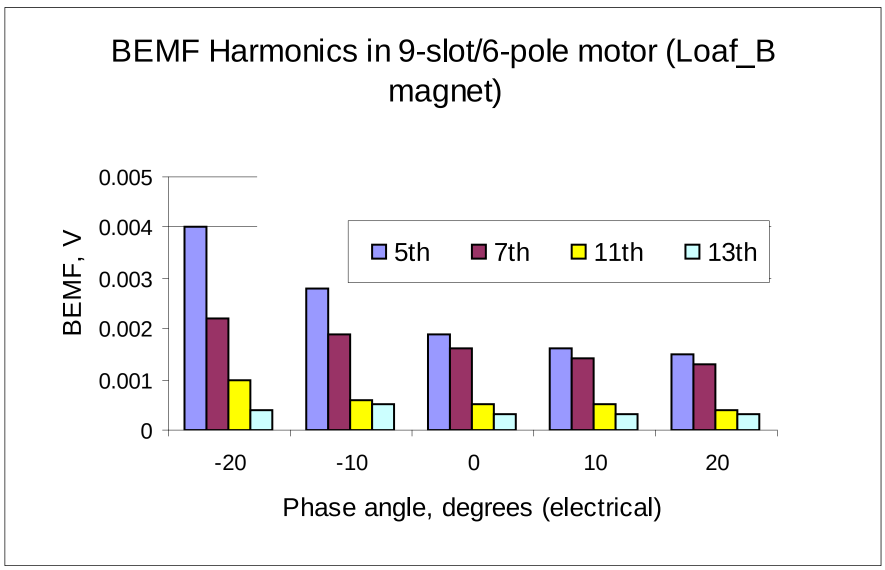

(b)

Figure 4.11: BEMF harmonic components (5^{th}, 7^{th}, 11^{th}, 13^{th}) (a) 9-slot/6-pole motor with loaf_A magnet (b) 9-slot/6-pole motor with loaf_B magnet.

-20°, -10°, 0°, 10°, 20°, 30°, and 40° respectively denoted by *m40* through *p40*. The main harmonics clearly follows the envelope of the peak-to-peak torque ripple waveforms for both the magnet shapes (non-skew cases shown in Fig. 4.10). Also, it is evident that the motor with loaf_B magnet shape has less BEMF harmonics compared to

Loaf_A (Fig. 4.11), which leads to early saturation in the former. The result is increased torque ripple in Loaf_A magnet design at all angles of phase lagging compared to zero phase (Figs 4.12 and 4.13).

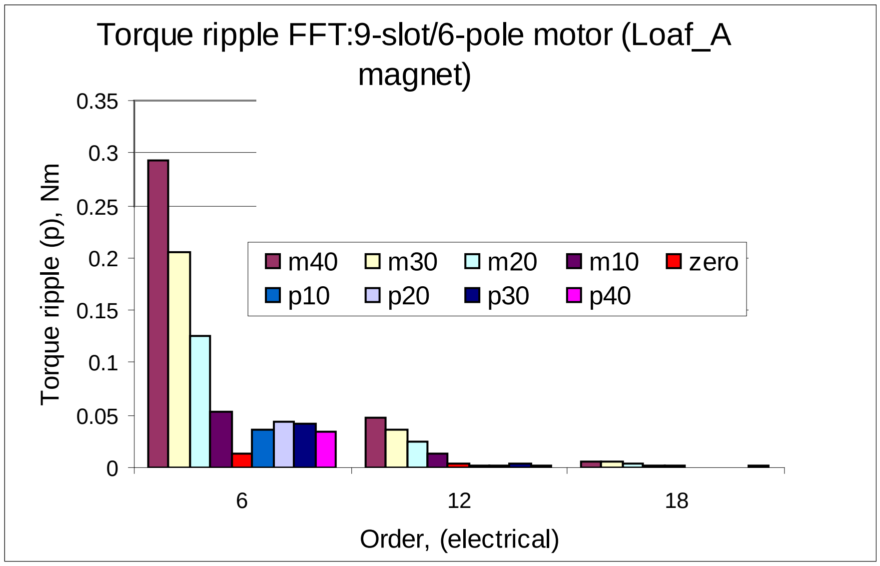

(a)

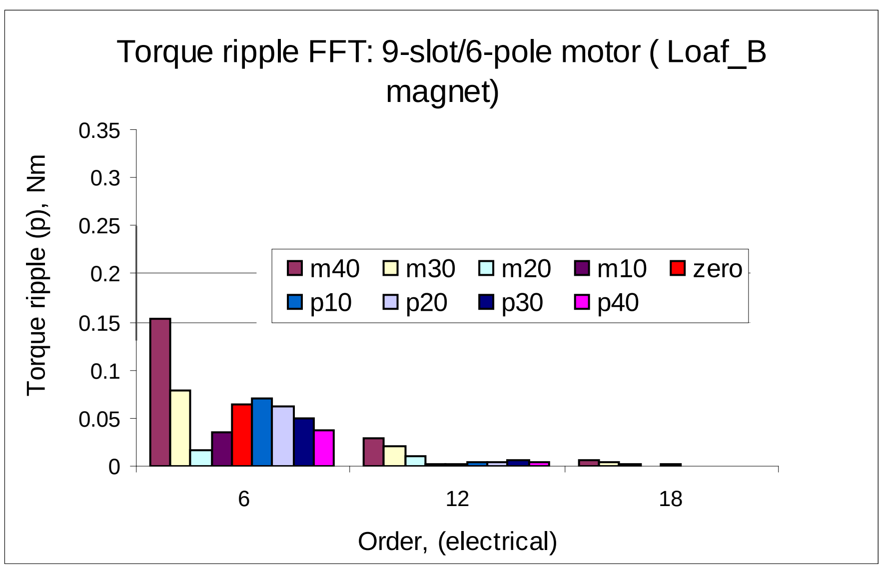

(b)

Figure 4.12. Absolute values of Torque Ripple harmonics (6^{th}, 12^{th}, 18^{th} orders) (a) 9-slot/6-pole motor with loaf_A magnet (b) 9-slot/6-pole motor with loaf_B magnet.

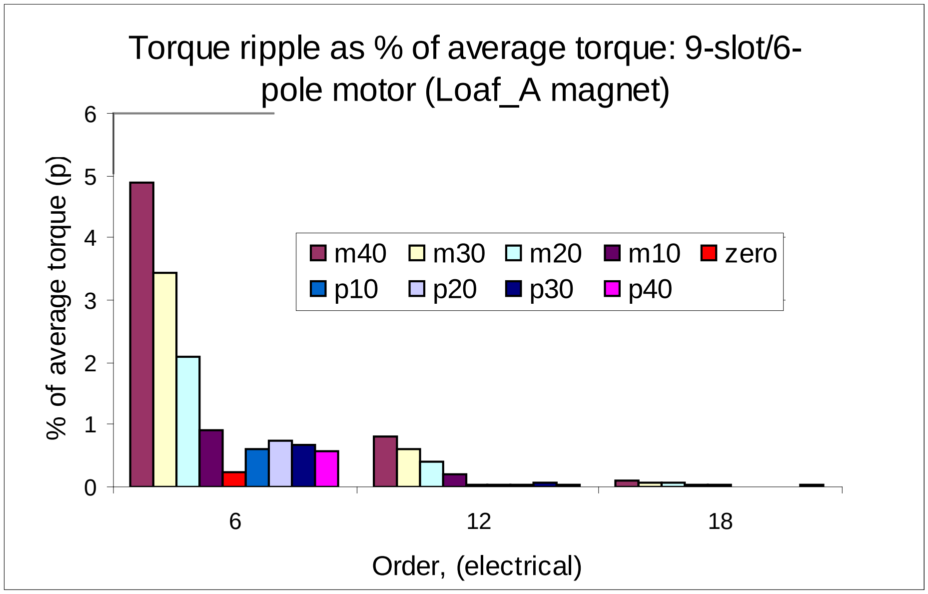

(a)

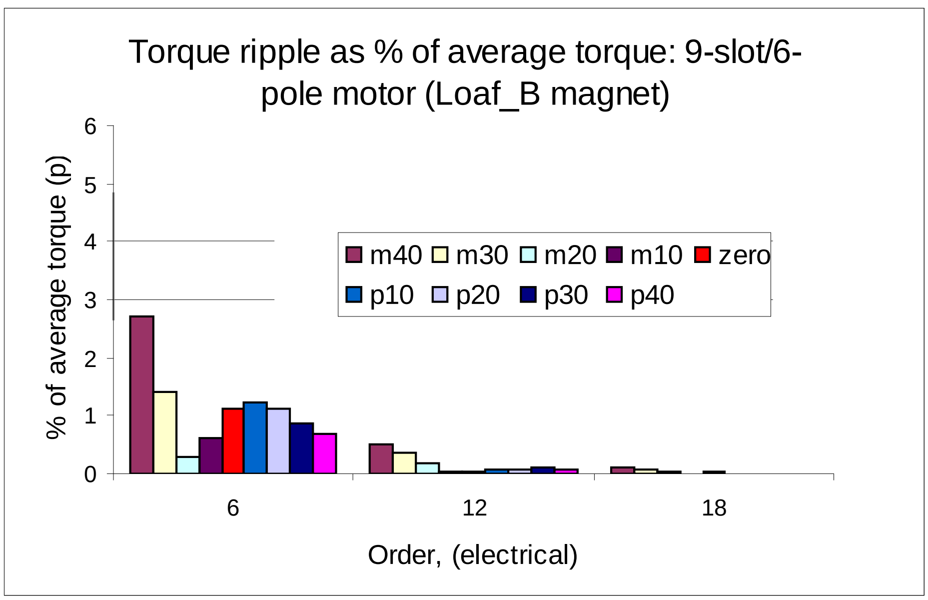

(b)

Figure 4.13. Torque ripple harmonics as % of average torque (6th, 12th, 18th orders) (a) 9-slot/6-pole motor with loaf_A magnet (b) 9-slot/6-pole motor with loaf_B magnet (with rotor positions of phase angles between -40°and 40°).

4.7.1 Effect of Saturation

The BEMF harmonics expressed as a percentage of their corresponding fundamental component for Loaf_A and Loaf_B magnet shapes is given in Fig. 4.14 for the zero phase angle condition. According to the principle of electromagnetic torque development in a PMSM without magnetic satuaration (presented in chapter II), the 6th order torque ripple should be equal to the contributions of 5th and 7th order BEMF harmonics. Thus, the torque ripple components in Fig. 4.13 for both the designs of 9-slot/6-pole PMSM should be originate from the BEMF components of Fig. 4.14. In both cases, the 6th order torque ripple values (percentage of average torque) are more than the 5th and 7th orders of BEMF values (percentage of the fundamental component of BEMF). The reason for this difference is the saturation in the magnetic circuit.

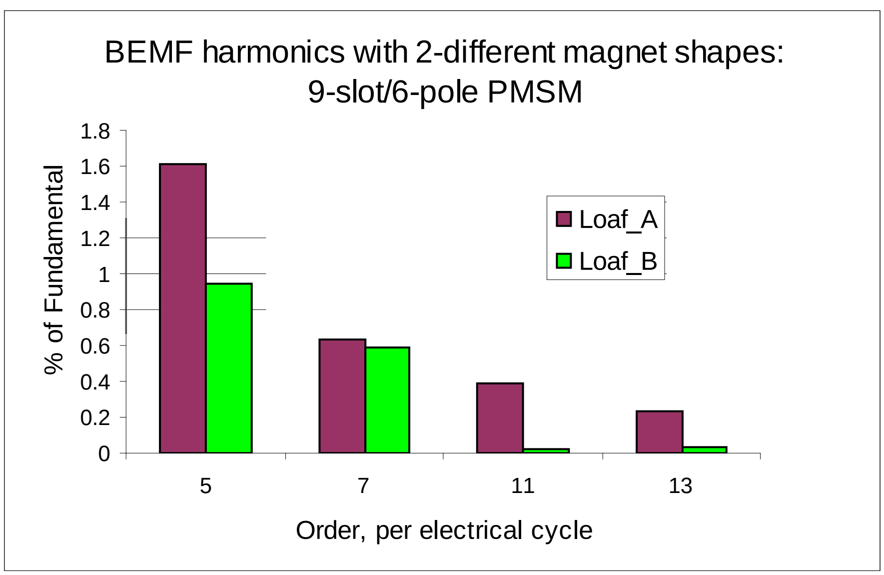

Figure 4.14: BEMF harmonics as % of fundamental (5th, 7th, 11th, 13th orders) in a 9/6 motor with loaf_A and loaf_B magnet.

The torque ripple arises from the existence of cogging torque, effect of BEMF harmonics, and non ideality due to saturation. The magnetic circuit in PM motor consists of the rotor and stator steel, magnet, and air. The magnetic permeability of magnet material and air are very close to unity wheareas the steel material posseses a very high permeability. Also, the property of steel is very much non-linear (typical B-H curves of Si steel can be found in Appendix-D). This means that beyond certain value of flux density (known as the saturation limit), the stator core gets saturated and the flux density in the core doesn't increase proportionately with the increase in air gap flux density. This ultimately distorts the smoothness of the BEMF wave forms (sinusoidal form appears with flat top) and causes torque pulsation. This phenomenon is known as saturation. A motor can go through this situation due to both electrical and magnetic loading. Electrical loading defines the amp-turn of the machine which is simply number of turns per coil times the amount of current through the coil. This is also called stator mmf due to current in the conductors. The flux density in the air gap due to permanent magnet is called the magnetic loading. This depends on the size, shape, remnant flux density of the magnet and the length of the air gap. The effect of saturation can be simulated by applying different levels of current (or amp-turn) to the stator winding and observing for the change in total torque ripple. Fig. 4.15 shows how a motor gradually enter into saturation with increasing amp-turn in the machine. The same results will follow if the PM flux density is increased instead. As the contribution to torque ripple due to BEMF harmonics as well as due to cogging torque remains constant irrespective of electrical or magnetic loading conditions, the ripple due to saturation can be obtained by subtracting

Results with linear steel can be interpreted as that for a machine without saturation; the total torque ripple will be the sum of cogging torque and ripple due to harmonics only.The instantaneous value of torque results from FE simulation when subtracted from the cogging torque will be equal to the torque derived from the sum of the products of phase BEMFs and phase currents (Fig. 4.16). In reality, saturation in PMSM is very common. The peak-to-peak torque ripple variation as a function of saturation (modeled as increasing phase currents in the x-axis) can be found in Fig. 4.17. The figure also shows the individual components of torque ripple for a 9-slot/6-pole motor design. The results shown are for a wide variation of phase currents. At any particular level of current the total ripple has a fixed component from cogging torque, a linearly increasing component from BEMF, and a quadratically increasing component due to saturation.

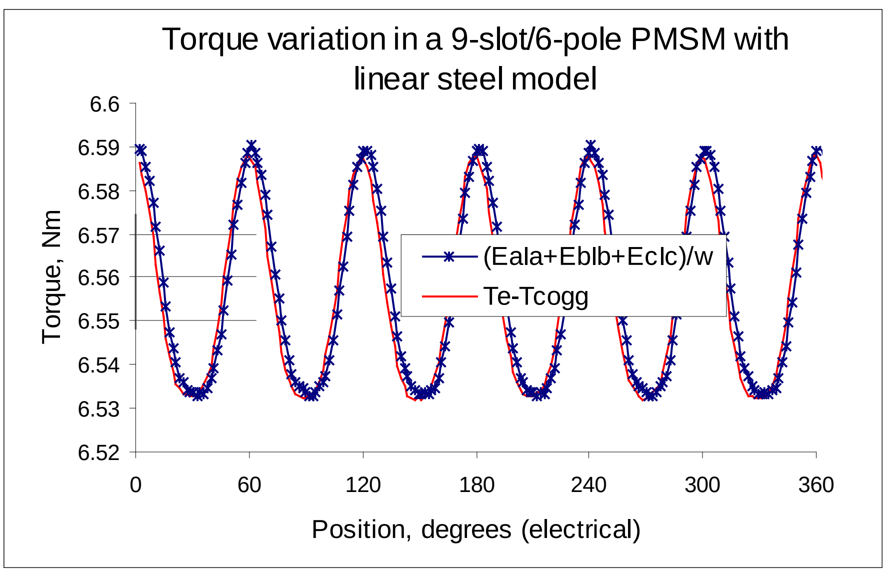

Figure 4.16: Torque ripple variation in a 9-slot/6-pole motor with linear steel as rotor iron and stator laminations.

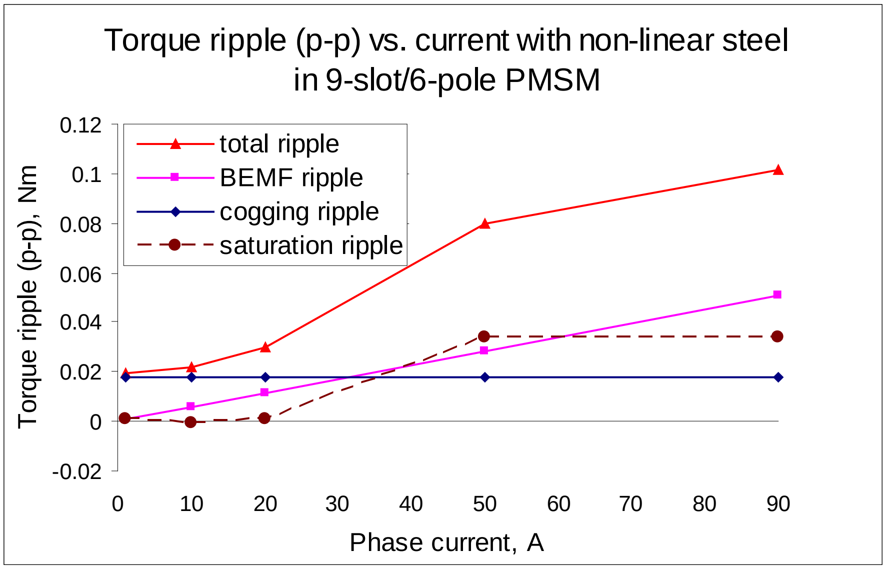

(a)

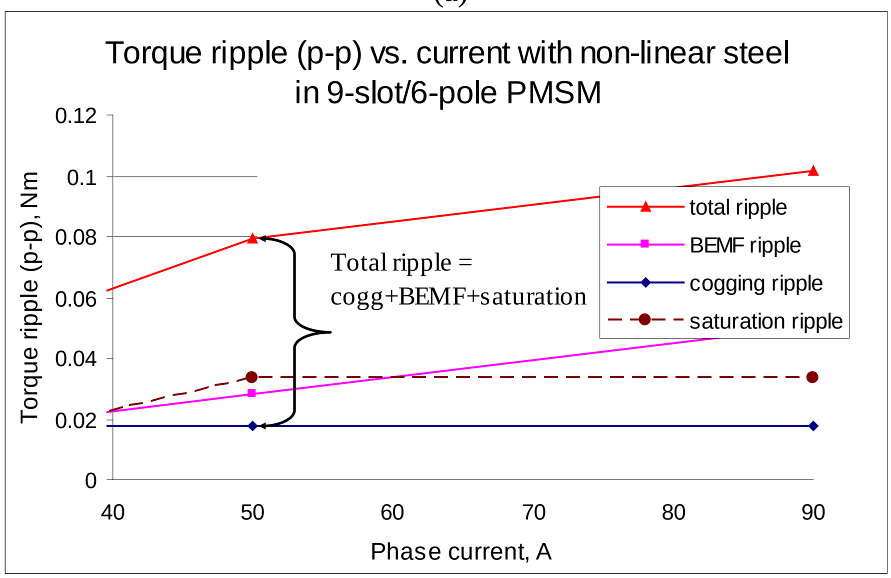

(b)

Figure 4.17: Torque ripple causing components in a 9-slot/6-pole motor with non-linear steel as rotor back iron and stator lamination (a) all current levels (b) higher levels of currents.

4.8 Simulation and Experimental Results

Torque ripple tests were conducted for two 0.75 hp, 90 A, 12 V PMSMs for an automotive application on a dyno test stand. Test results obtained for the 9-slot/6-pole non-skewed and skewed motor closely resembles the FE simulation results for the same motor. The FE results and the test data are plotted in Fig. 4.18. Tests were also conducted on a 12-slot/10-pole non-skewed PMSM. The test data contains 1st order harmonics because of measurement noise, and have slot order and pole order harmonics arising from asymmetry in the rotor and stator, respectively. Those orders were filtered out before comparing with simulation results. The simulation and experimental results are given in Fig. 4.19. The results of the 12-slot/10-pole motor shows that magnet shaping didn't help in reducing torque ripple.The experimental results verify that torque ripple reduction is possible through magnet shaping and step skewing only in certain machine configurations.

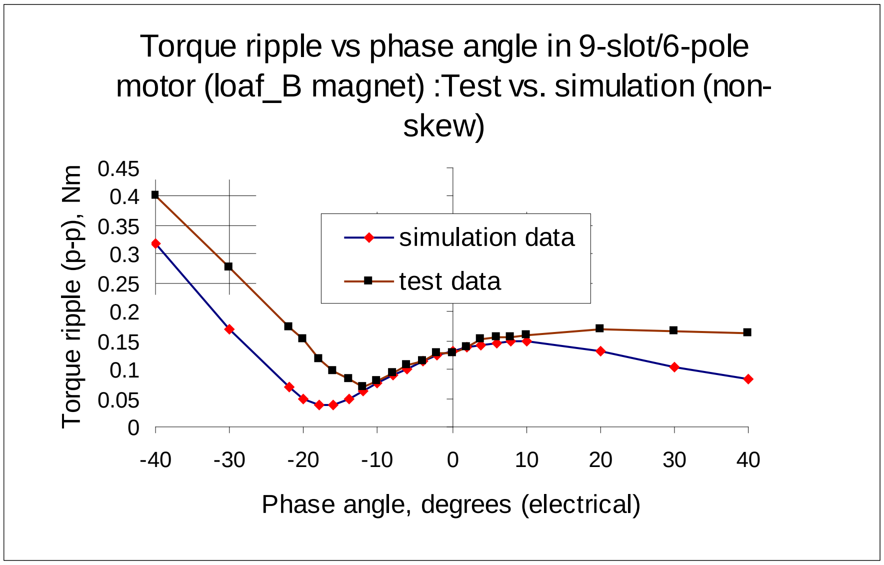

(a)

Figure 4.18: Peak-to-peak torque ripple variation in a 9/6 motor (a) test and simulation results for non-skewed motor; (b) test and simulation results for the skewed motor.

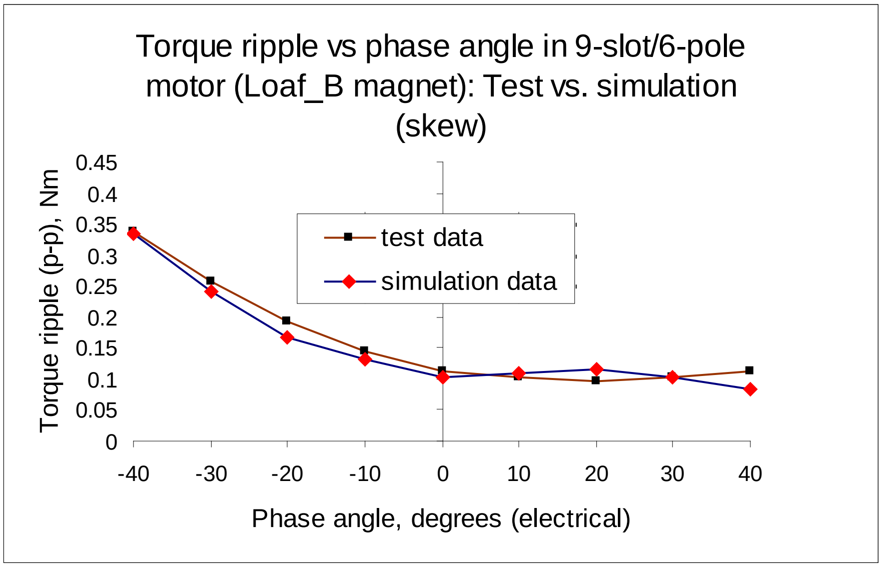

(b)

Figure 4.18: Peak-to-peak torque ripple variation in a 9/6 motor (a) test and simulation results for non-skewed motor; (b) test and simulation results for the skewed motor. (continued)

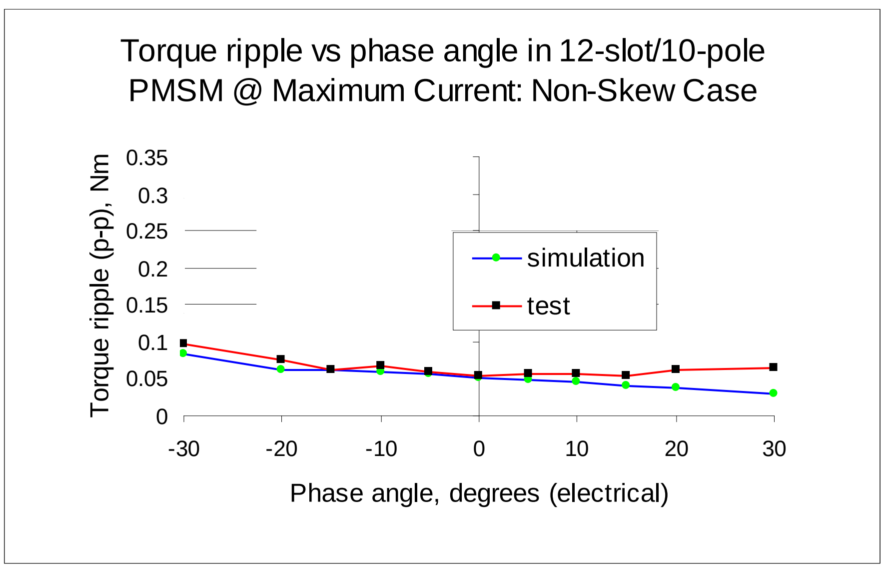

Figure 4.19: Peak-to-peak torque ripple variation in a 12/10 non-skewed motor; test and simulation results.

4.9 Conclusions

Torque ripple improvement in PMSMs using step-skewed magnet is an effective approach, but requires careful selection of magnet shapes. The torque ripple reduction approach using skewing is more effective in machines that have a higher optimum skew angle, such as in 9-slot/6-pole and 12-slot/8-pole machines. However, some motors will have an increase in torque ripple even after magnet skew if the magnet shape is not designed carefully.

FE analysis and test results were obtained for both 9-slot/6-pole and 12-slot/10-pole motors to validate the torque ripple analysis presented in this dissertation. Also extensive simulations were carried out for 27-slot/6-pole and 12-slot/8-pole motors. The analysis is complicated due to machine saturation induced nonlinearities at higher torque levels. FE analysis is useful in the design stage to study the torque ripple for different PMSM designs.

CHAPTER V

RADIAL FORCE AND VIBRATION ANALYSIS

5.1 Radial Force, Stator Vibration, and Acoustic Noise

The acoustic noise in PM machines is lower compared to switched reluctance and induction machines; yet quieter performance is desired in automotive and robotics applications. Noise and vibration of the electromagnetic origin dominates in low to medium power PM machines. The electromechanical energy conversion due to an interaction between the magnetic fields of PMs and armature conductors takes place in the airgap of these machines. As a result of this interaction a strong electromagnetic force field exists between the rotor magnets and the stator teeth. This force field can be decomposed into tangential and radial force components at any point in the airgap. The tangential or the circumferential component (F_{tan}) is responsible for the electromagnetic torque acting on the rotor and the stator frame simultaneously. Whereas the normal or the radial force component (F_{rad}), known as radial force, causes the radial vibration of the stator structure (Fig. 5.1). This stator vibration along with pulsation of electromagnetic torque is the main source of acoustic noise in PM machines. The radial force is undesirable especially when it leads to unbalanced pull on the stator.

As mentioned previously in chapter I, the noise and vibration in PMSMs can be caused by electromagnetic, mechanical or aerodynamic sources. The relative contribution of noise and vibration from all these sources are explained in chapter II (Fig. 2.1). The vibration of electromagnetic origin is the main focus of this research. Proper selection of slots and poles number, together with the winding arrangement is the key to minimize the noise and vibration levels. This research is focused to find the root cause of electromagnetic noise and vibration in 9-slot/6-pole, 12-slot/10-pole, 12-slot/8-pole and 27-slot/6-pole motors.

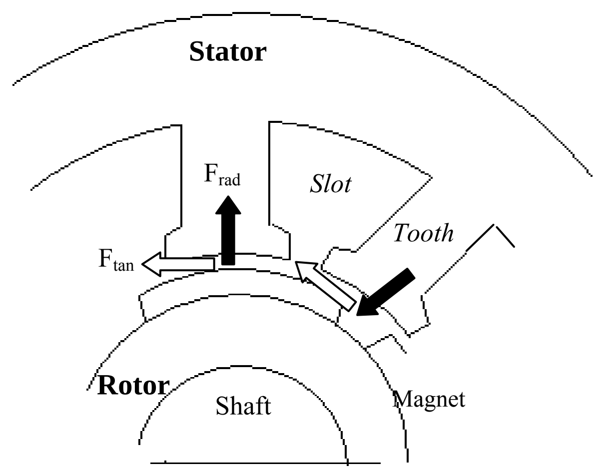

Figure 5.1: Radial and tangential component of electromagnetic forces in a PMSM structure.

This chapter analyses the electromagnetic vibration in PMSMs mostly used in servo type applications such as in the power steering of an automobile. A procedure for calculating the magnetic radial forces on the stator teeth based on the 2D finite element method is presented first. The radial force density or pressure is the radial force per unit area of the stator tooth and can be calculated both by Maxwell's stress equation and by finite element analysis. An analytical model of the motor is then developed to predict the radial displacement on the stator teeth due to the radial forces. The radial displacement of the stator tooth is a direct indication of the vibration. The noise caused due to this vibration is strongly influenced by the dominant order of modes excited in a particular motor configuration. Four types of motor configurations are analyzed in this research for comparative performance evaluation with regards to noise and vibration.

5.2 Unbalanced Radial Forces in Modular Machines

The attraction between the rotor permanent magnets and the stator iron causes radial stator forces that excite the stator structural modes and radiate unwanted acoustic noise. A perfect rotor motor with balanced stator windings should have a net zero radial force on the stator structure. However, unbalanced radial force can be present in machines having diametrically asymmetric disposition of slots and phase windings [13, 36, and 37]. This force is significant in permanent magnet brushless AC and DC machines having a fractional ratio of slot number to pole number, especially when the electric loading is high. Typical 3-phase machines with fractional ratios can have the slot/pole combinations of 3-slot/2-pole, 3-slot/4-pole; 9-slot/8-pole, 9-slot/10-pole; 15-slot/14-pole, 15-slot/16-pole, and so on.

The unbalanced magnetic force acts on the stator of these machine configurations due to an asymmetric magnetic field distribution in the air gap. The authors in [13] have calculated the unbalanced force components analytically and validated the results with FEA using Maxwell's stress tensor method; the analysis was carried out for 3-slot/2-pole and 9-slot/8-pole PMSM and PMBLDC motors. Each phase of the 9-slot/8-pole machine comprises of three adjacent coils connected in series, the middle coil being of opposite polarity to the other two coils (Fig. 5.2a). Although the windings of phases A, B and C are displaced by 120^0 Elec. and their BEMFs are symmetrical and phase shifted by 120^0 Elec., the disposition of the phase windings about the diameter of the machine is asymmetrical. This results in an unbalanced magnetic force between the rotor and the stator. Machines with slot-pole combinations of 6-slot/8-pole, 12-slot/10-pole, and 12-slot/14-pole can also have an asymmetrical distribution of winding. However, a symmetry can be achieved (Fig. 5.2b) with a rearrangement of the windings. The special type of winding configuration needed to make it symmetrical is called 'modular' winding where the coils of the same phases are located in diametrically opposite slots. On the other hand, the winding distribution is symmetrical for 3-phase machines like 9-slot/6-pole, 12-slot/8-pole, 15-slot/10-pole, 27-slot/6-pole, 18-slot/12-pole and few others; one such configuration is shown in Fig. 5.2c.

The PMSMs with fractional ratio of slot number to pole number can be classified into the following three types based on their slot/pole combinations: (a) Type I having asymmetric distribution of slots and windings (b) Type II having the same phases in diametrically opposite slots and called "modular" winding and (c) Type III having the phases with symmetrically wound and referred to as "non-modular" winding. The above naming convention will be used in this dissertation. In the ideal case, none of the Type II and Type III motors should have any unbalanced radial forces on the stator. In reality, Type II motors have unbalanced forces like Type I motors. The non-modular winding configurations in 12-slot/8-pole and 27-slot/6-pole motors are given in Appendix-B.

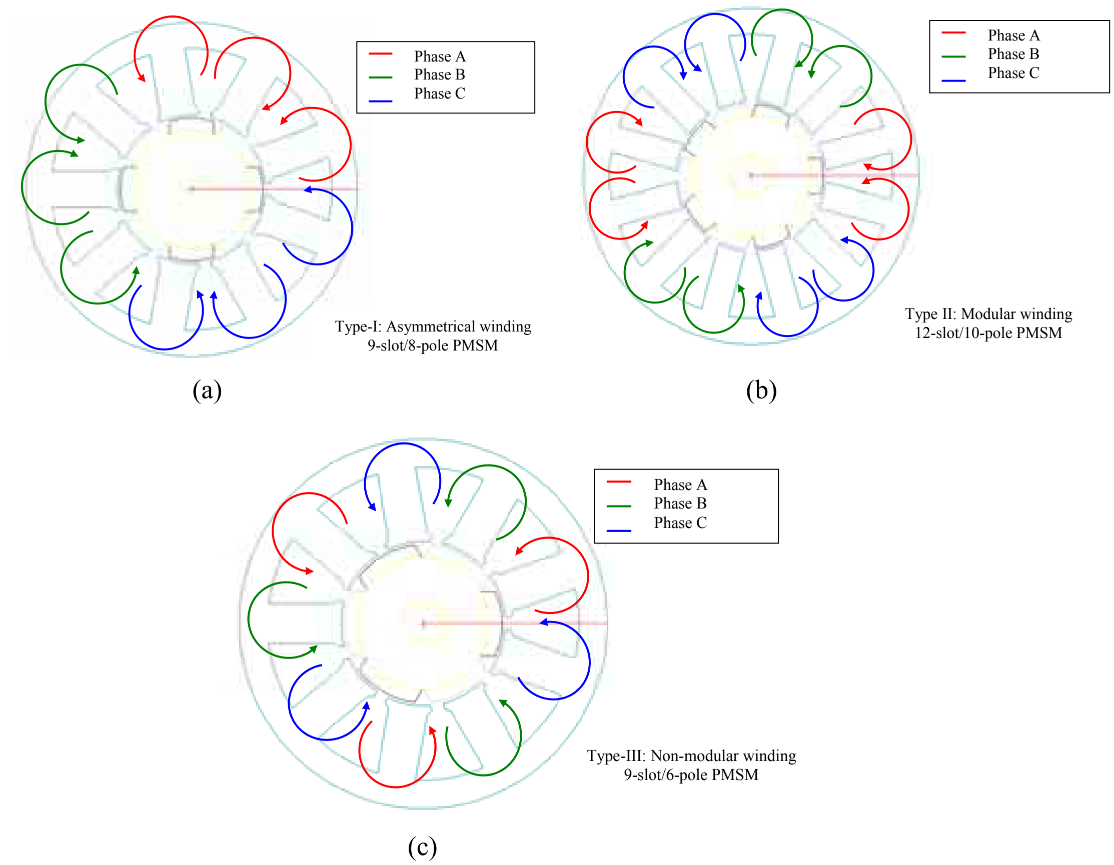

Figure 5.2 Different PMSM configurations from winding point of view (a) Asymmetrical (b) Modular (c) Non-modular or symmetrical.

5.3 Radial Force Density

The stress of the PM magnetic field and the stator mmf field is measured as radial force density which is more commonly known as the radial pressure. Maxwell's stress tensor method is generally used to calculate this electromagnetic force acting on an object. In case of a 2D FE analysis, a surface containing the object is selected as a line (say *l*) and then the tangential and the radial components of the force are calculated [13]. The forces are given by

$$F_{\tan} = \frac{L_{stk}}{\mu_0} \oint_l B_t B_n dl \tag{5.1}$$

$$F_{rad} = \frac{L_{stk}}{2\mu_0} \oint_l (B_n^2 - B_t^2) dl \tag{5.2}$$

Here B_t and B_n represent the tangential and normal component of the flux density in the airgap, L_{stk} is the stack length of the motor and l represents the line containing the object where force is to be computed. The presence of excessive radial force on the stator tooth can lead to stator vibration, and therefore, can produce noise. The composition of radial pressure is analyzed in the following.

The space and time distribution of the rotor and stator MMF of a polyphase electrical machine fed with balanced sinusoidal currents can be expressed by the following equations [11]:

For the stator

$$\overrightarrow{\Im_1}(\alpha, t) = \sum_{\nu=0}^{\infty} F_{m\nu} \cos(\nu p \alpha \pm \omega_\nu t) \tag{5.3}$$

For the rotor

$$\overrightarrow{\Im_2}(\alpha, t) = \sum_{\mu=0}^{\infty} F_{m\mu} \cos(\mu p \alpha \pm \omega_\mu t + \phi_\mu) \tag{5.4}$$

where α is the angular distance from a given axis, p is the number of rotor pole pairs, ϕ_μ is the angle between vectors of the stator and rotor harmonics of equal order, ν and μ are the numbers of harmonics of the stator and rotor, respectively, and $F_{m\nu}$ and $F_{m\mu}$ are the peak values of the ν^{th} and μ^{th} harmonics, respectively. The product $p\alpha = \pi x/\tau$ where τ is the pole pitch and x is the linear distance from a given axis. The instantaneous value of normal component of the magnetic flux density in the air gap at a point α can be calculated as the product of airgap permeance and the total airgap mmf produced by the rotor and stator

$$B_n(\alpha,t) = [\Im_1(\alpha,t) + \Im_2(\alpha,t)]G(\alpha,t) = B_1(\alpha,t) + B_2(\alpha,t) \tag{5.5}$$

where $B_1(\alpha,t) = \sum_{\nu=0}^{\infty} B_{m\nu} \cos(\nu p\alpha \pm \omega_\nu t)$ is the normal component of flux density of the stator and $B_2(\alpha,t) = \sum_{\mu=0}^{\infty} B_{m\mu} \cos(\mu p\alpha \pm \omega_\mu t + \phi_\mu)$ is the normal component of flux density of the rotor. Also, the air gap relative permeance variation *G(α)* can be expressed with the aid of Fourier series as an even function to model the air gap variation bounded by the stator and rotor active surfaces

$$G(\alpha) = \frac{A_0}{2} + \sum_{k=1,2,3,..}^{\infty} A_k \cos(k\alpha) \quad \text{H/m}^2 \tag{5.6}$$

where k is the number of harmonics. Once the airgap flux distribution is known, the magnitude of the radial force per unit area at any point of the air gap can then be calculated according to Maxwell stress tensor in (5.2). This force per unit area is called radial pressure $P_r(\alpha,t)$ given by [11]

$$P_r(\alpha,t) = \frac{1}{2\mu_0}[B_n^2(\alpha,t) - B_t^2(\alpha,t)] \tag{5.7}$$

Since the magnetic permeability of the ferromagnetic core is much higher than that of the airgap, the magnetic flux lines are practically perpendicular to the stator and rotor cores. This means the tangential component of flux is much smaller than the normal component and can be neglected. Therefore, the expression for radial pressure simplified to

$$P_r(\alpha,t) \approx \frac{B_n^2(\alpha,t)}{2\mu_0} = \frac{1}{2\mu_0}[\Im_1(\alpha,t) + \Im_2(\alpha,t)]^2 G^2(\alpha)$$

$$= \frac{1}{2\mu_0}[\Im_1^2(\alpha,t) + 2\Im_1(\alpha,t)\Im_2(\alpha,t) + \Im_2^2(\alpha,t)]^2 G^2(\alpha)$$

$$= \frac{1}{2\mu_0}[\{B_1(\alpha,t)\}^2 + 2B_1(\alpha,t)B_2(\alpha,t) + \{B_2(\alpha,t)\}^2]$$

$$= \frac{1}{4\mu_0}[B_{m\nu}^2\{1+\cos(2\nu p\alpha \mp 2\omega_\nu t)\} + 4B_{m\nu}B_{m\mu}\{\cos[p\alpha(\nu-\mu)\mp(\omega_\nu-\omega_\mu)t-\phi_\mu] + \cos[p\alpha(\nu+\mu)\mp(\omega_\nu+\omega_\mu)t+\phi_\mu]\} + B_{m\mu}^2\{1+\cos(2\varpi_\nu p\alpha \mp 2\omega_\mu t + 2\phi_\mu)\}]$$

(5.8)

There are three groups of the infinite number of radial force waves. The first and the third term in (5.8), called the square terms, are the constant stress due to stator mmf and rotor field respectively. The second term represents the pulsating force waves as a product of both the rotor and stator mmfs. The square terms produce constant stresses and radial force waves with double the number of pole pairs and double the pulsation of the source wave magnetic flux density. This constant stress term represent the static magnetic pressure uniformly distributed along the airgap and is not important with regards to noise and vibration. Only the interaction of the rotor and stator waves (second term in 5.8) produce low mode and high amplitude of force waves, which are important from the acoustic point of view. The radial pressure with the above assumptions can further be simplified to

$$P_{r\nu\mu}(\alpha,t) = \frac{2B_{m\nu}\cos(\nu p\alpha \mp \omega_\nu t)B_{m\mu}\cos(\mu p\alpha \mp \omega_\mu t + \phi_\mu)}{2\mu_0}$$
$$= \frac{B_{m\nu}B_{m\mu}}{2\mu_0}\{\cos[p\alpha(\nu-\mu)\mp(\omega_\nu-\omega_\mu)t-\phi_\mu] + \cos[p\alpha(\nu+\mu)\mp(\omega_\nu+\omega_\mu)t+\phi_\mu]\}$$
$$= P_{r,\max}\cos(r\alpha - \omega_r t)$$

(5.9)

where $r = (\nu \pm \mu)p = 0,1,2,3,....$ is the mode number of the force wave and $\omega_r = \omega_\nu \pm \omega_\mu$ is the angular frequency of the force of the r^{th} order. The radial force circulate around the stator bore with the angular speed ω_r/r and frequency $f_r = \omega_r/(2\pi r)$. The amplitude of the radial pressure is

$$P_{r,\max} = \frac{B_{m\nu} B_{m\mu}}{2\mu_0} N/m^2 . \tag{5.10}$$

Clearly the amplitude of pressure on the stator surface depends on the maximum value of rotor and stator contributed airgap flux density; this pressure variation is sinusoidal. The amplitude of the radial force on any tooth can be calculated by multiplying the pressure amplitude P_r with the area of that tooth which is $\pi D_{in} L_{stk}/N_p$, where D_{in} is the stator core inner diameter and N_p ($N_p = 2p$) is the number of rotor poles.

5.3.1. Calculation of Radial Pressure

The maximum value of radial force on a stator tooth or the radial pressure distribution on the tooth surface can be calculated by the analytical equation in (5.7) or by FEA tool. Both the amplitude and the frequency of radial pressure are important in relation to acoustic behavior of the machines and they vary significantly from no-load to full-load conditions. The issues will be addressed separately in this chapter. A set of typical values of radial pressures and tooth forces under no-load for several motor configurations are given in Table 5.1. Here, the airgap flux is only due to the permanent magnet and rotates at the pole-pair frequency. The radial pressure varies with the square of the flux density and should be rotating at pole frequency around the tooth periphery. Therefore, the main pressure component other than the DC will be the pole order component. The radial pressure wave acts directly on the tooth tips. The stator bore surface is not smooth but is covered with alternating slots and teeth. These waves are present also in the slotted zones. Thus the actual total force exerted on the teeth is given by the integral sum of the force over the area within the tooth pitch.

The analytical calculation of pressure is a crude approximation as it is based on the average flux density in the airgap rather than the distribution of the airgap flux. The FEA tool can capture this distribution and predict the stress due to this flux around the stator teeth that might lead to possible deformations. Therefore, a difference can be seen between the analytical and the FE results in Table 5.1. Also, the radial pressure is higher in 12-slot/10-pole motor compared to 9-slot/6-pole motor whereas the total force on a tooth of the former is less than the latter. It is the magnitude of pressure on the tooth and its frequency that determines the amount of vibration, and not the magnitude of force.

Table 5.1: Calculated Radial Pressure @ no-load Condition (FEA vs. Analytical)

Motor configuration	Max. air-gap flux density, B_g (T)	Radial pressure, $P_{r,max}$ (max), N/m^2		Tooth area, A_{tooth} (m^2)	Radial force (max) on a tooth, N ($P_{r,max} \cdot A_{tooth}$)	
		Analytical	FEA		Analytical	FEA
9-slot/6-pole	0.819	2.67E+05	3.77E+05	0.000867	231.4	327.1
12-slot/8-pole	0.863	2.89E+05	4.07E+05	0.000651	188.2	265.0
12-slot/10-pole	0.853	2.96E+05	4.27E+05	0.000651	192.6	277.8
27-slot/6-pole	0.882	3.10E+05	3.36E+05	0.000257	79.6	86.3

These will be explained in the next section with relation to dominant mode orders in each motor under different loading conditions.

5.4 Radial Vibration and Dominant Mode Shapes

The radial forces are transmitted through the teeth from the air gap to the yoke which can cause deformation on the stator rings. This deformation is the largest when the vibrating frequency of the stator f_r is close to the natural mechanical frequency [53] of the stator ($f_{m=r}$ in 5.11). From airborne noise point of view, the most important frequencies are those of low mode numbers, i.e., frequencies at r = 0, 2, and 4. Deformations of the stator core for different vibration modes commonly called "mode shapes" are shown in Fig. 5.3 [43]. For r = 0 the radial force is distributed uniformly around the stator periphery and changes periodically with time [36, 43, and 53]. For r = 1, the radial pressure produces a single-sided magnetic pull on the motor and a pull rotation with certain angular velocity. A heavy vibration of the machine occurs at resonance when pull rotation speed matches the natural frequency of the stator. In most cases, the second order cylindrical mode or fundamental mode with r = 2 is the predominant mode. The mode with r = 4 is the fourth order mode causing double ovalization on the yoke circumference. All the mode shapes have their own natural mode frequencies. Any particular mode shape is excited when its natural mode frequency matches with any of the harmonics of the magnetic radial force.

The natural frequency of the stator of the r^{th} order can be expressed as

$$f_{m=r} = \frac{1}{2\pi}\sqrt{\frac{K_r}{M_r}} \tag{5.11}$$

where K_r and M_r are the lumped stiffness and lumped mass of the stator, respectively. Analytical equations for calculation of K_r and M_r can be found in [11, 22].

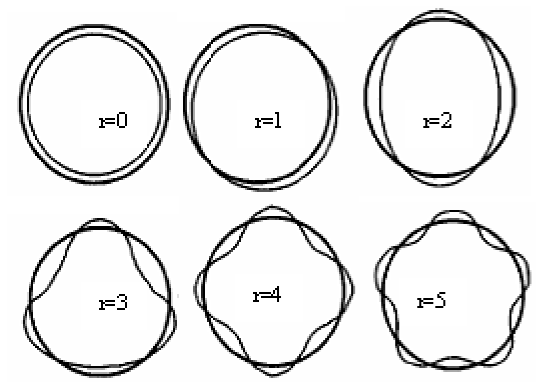

Figure 5.3: Circumferential vibration modes with different mode numbers.

For a stator core with thickness w_{bi}, mass M_{st}, and the mean diameter D_m , the lumped stiffness and lumped mass in the circumferential vibration mode $r = 0$ is

$$K_0 = 4\pi \frac{E w_{bi} L_{stk}}{D_m} \text{ and } M_0 = M_{st} k_{md} \tag{5.12}$$

where $k_{md} = 1 + \frac{M_t + M_w + M_i}{M_{st}}$ is the mass addition factor, M_t is the mass of all teeth, M_w is the mass of stator windings, and M_i is the mass of insulation. The lumped stiffness and mass for other mode shapes are calculated in a similar fashion to find the natural mode frequencies. The details of the mode frequency calculation can be found later in this chapter.

5.4.1. Radial Pressure and Mode Shapes under No-load Conditions

The FEA results for radial pressure distribution around the stator tooth periphery without stator excitation are given in Fig. 5.4 for 9-slot/6-pole, 12-slot/10-pole, 12-slot/8-pole, and 27-slot/6-pole motors. These results show a sinusoidal variation of tooth pressure with a constant value; the constant values of pressures are different in different motor topologies. In most cases, other than the modular type of motors (for instance, 12-slot/10-pole PMSM), the dominant modes of the pressure waves are equal to the number of poles. This is why the pressure distribution in 1-mechanical cycle shows 6, 6, and 8 cycles with equal amplitudes in a 9-slot/6-pole, 27-slot/6-pole, and 12-slot/8-pole PMSMs, respectively (Fig. 5.4 a, b, and c). All of these PMSMs are non-modular type of machines. In a modular machine of 12-slot/10-pole topology as in Fig 5.4(d), in one mechanical cycle there are 5 cycles of pressure distribution with slightly different amplitudes and the pattern is repeated twice. Therefore, modes 2 and 10 exist in this machine in addition to the sub-orders of 2 and 10. These FE results contain some glitches of very high frequency and are not of interest from the vibration perspective. These are caused due to mesh of the FE model and its misalignment between adjacent layers as one layer rotates with respect to the other.

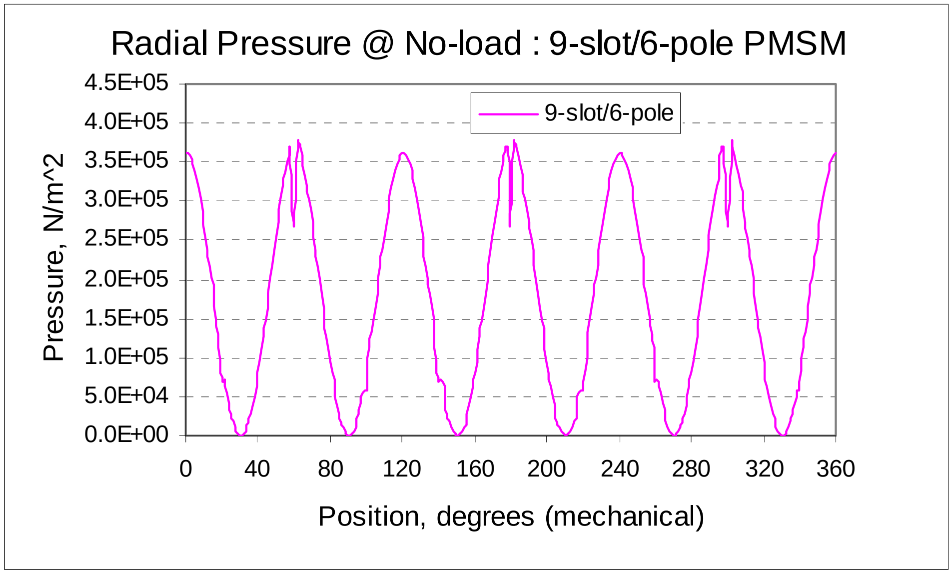

(a)

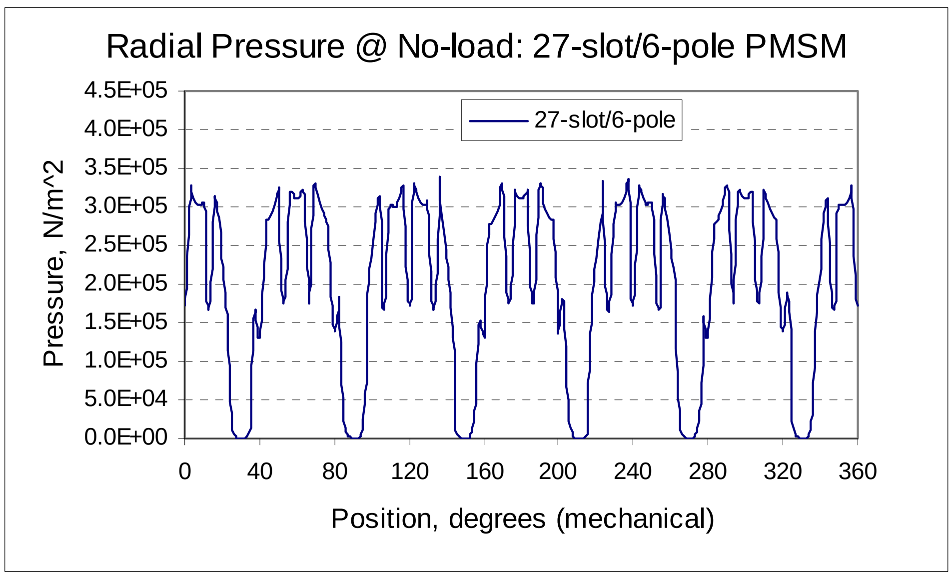

(b)

Figure 5.4: Radial pressure variation without stator excitation obtained from FEA as space distribution (a) 9-slot/6-pole (b) 27-slot/6-pole (c) 12-slot/10-pole (d) 12-slot/8-pole PMSM.

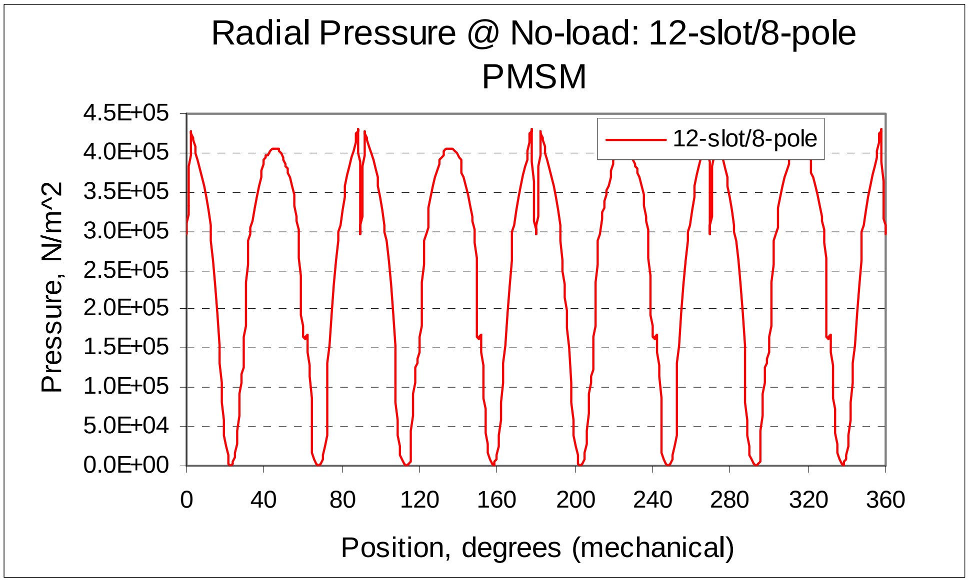

(c)

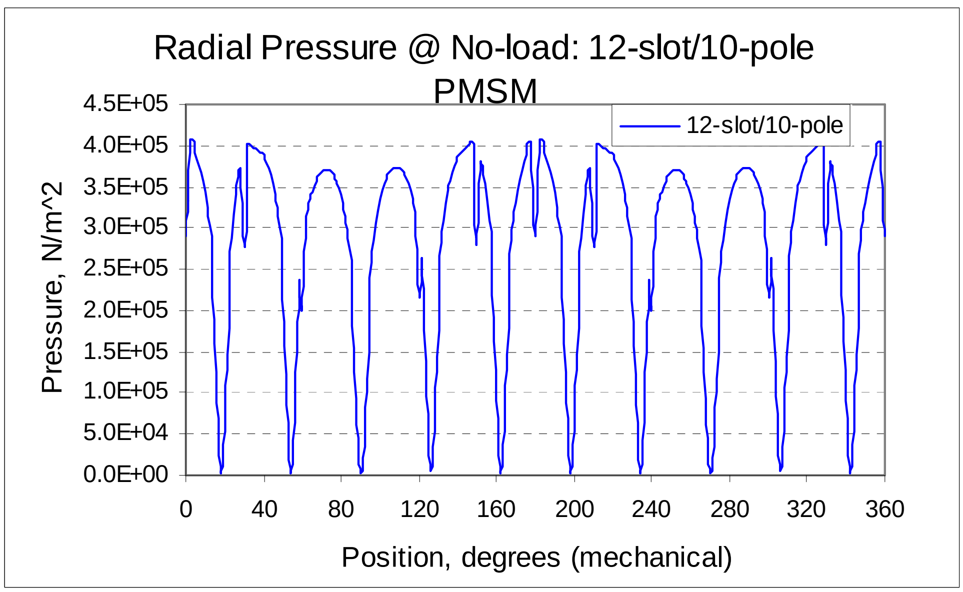

(d)

Figure 5.4: Radial pressure variation without stator excitation obtained from FEA as space distribution (a) 9-slot/6-pole (b) 27-slot/6-pole (c) 12-slot/10-pole and (d) 12-slot/8-pole PMSM.(continued)

The FFT analysis of the pressure variations clearly identifies all the mode orders in the motors (Fig. 5.5). The orders in a 12-slot/10-pole motor are 2, 4, 6, 8, 10, 12 etc. and in a 12-slot/8-pole motor are 8, 16, 24 and so on. The lower the order of the frequency of this radial pressure, the more is the likelihood of the motor to run into resonance. For instance, the 12-slot/10-pole motor shows order 2 components compared to orders 8, 6, and 6 in 12-slot/8-pole, 9-slot/6-pole, and 27-slot/6-pole motors, respectively. This means a 12-slot/10-pole motor has more chance to run into resonance compared to any of the 12-slot/8-pole, 9-slot/6-pole, or 27-slot/6-pole motors. In conclusion, modular type machines could be more prone to vibration than the non-modular type machines.

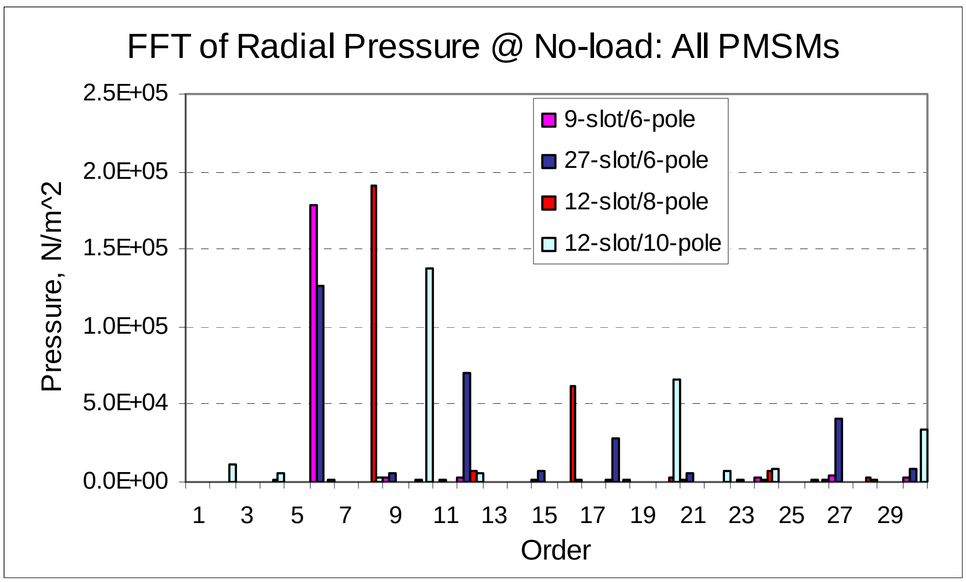

Figure 5.5: Radial pressure variation without stator excitation: FFT analysis.

5.4.2. Radial Pressure and Mode Shapes under Full-load Conditions

The mechanics of the radial pressure distribution and its frequency contents change with stator excitation. The lower mode frequency appears in the machine with excitation compared to without excitation. For instance, a 12-slot/8-pole motor sees mode 4 under stator excitation whereas the lowest mode under no excitation was 8. The mode shapes under stator excitation are marked in FE plots of radial flux vectors given in Fig. 5.6 for all four PMSM configurations.

The difference in radial pressure distribution for modular and non-modular machines can also be analyzed by considering the candidate 12-slot/10-pole and 9-slot/6-pole motors, respectively. The changes in radial pressure distribution for no-load and full-

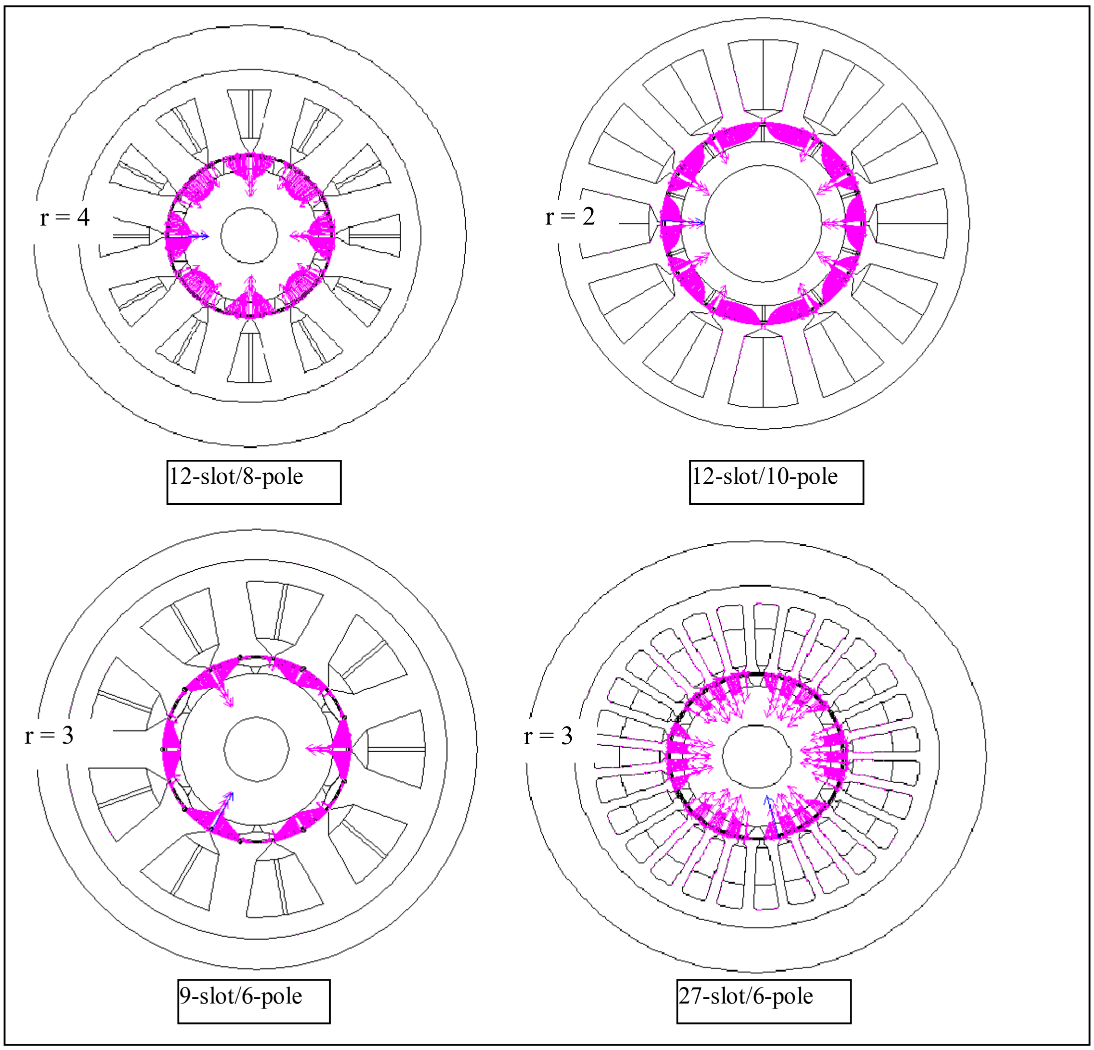

Figure 5.6: Radial pressure distribution on the stator tooth showing the dominant order of modes in different motor topology with stator excited.

load conditions are shown in Fig. 5.7 for each of these motor configurations. Fig. 5.7c shows the change of lower order mode from 6 to 3 for a change of no-load to full-load in a non-modular PMSM with 9-slot/6-pole configuration. On the other hand, for a modular PMSM with 12-slot/10-pole configuration the low order mode 2 prevails and amplified

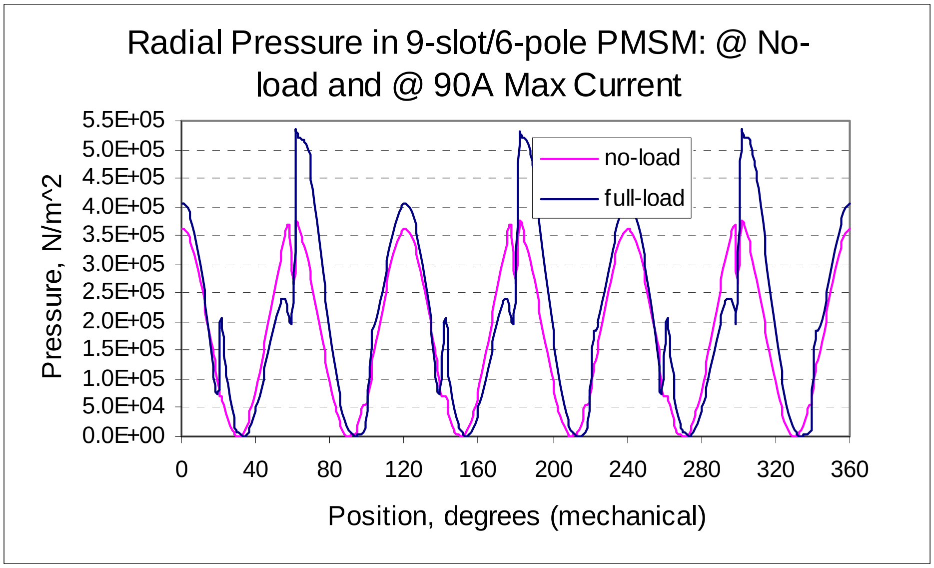

(a)

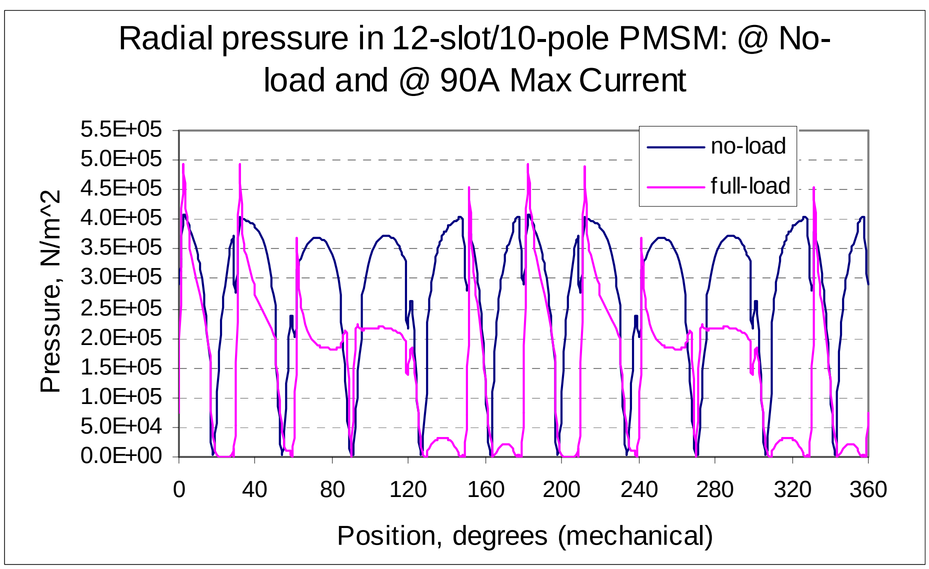

(b)

Figure 5.7: Radial pressure (a) variation at full-load vs. no-load in a 9-slot/6-pole (b) variation at full-load vs. no-load in a 12-slot/10-pole PMSM (c) FFT of radial pressure for 9-slot/6-pole (d) FFT of radial pressure for 12-slot/10-pole.

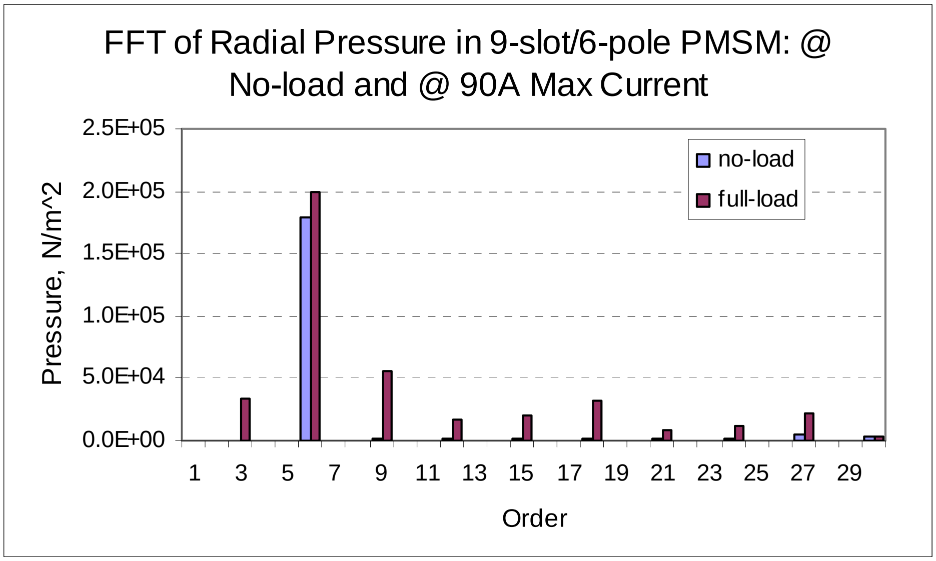

(c)

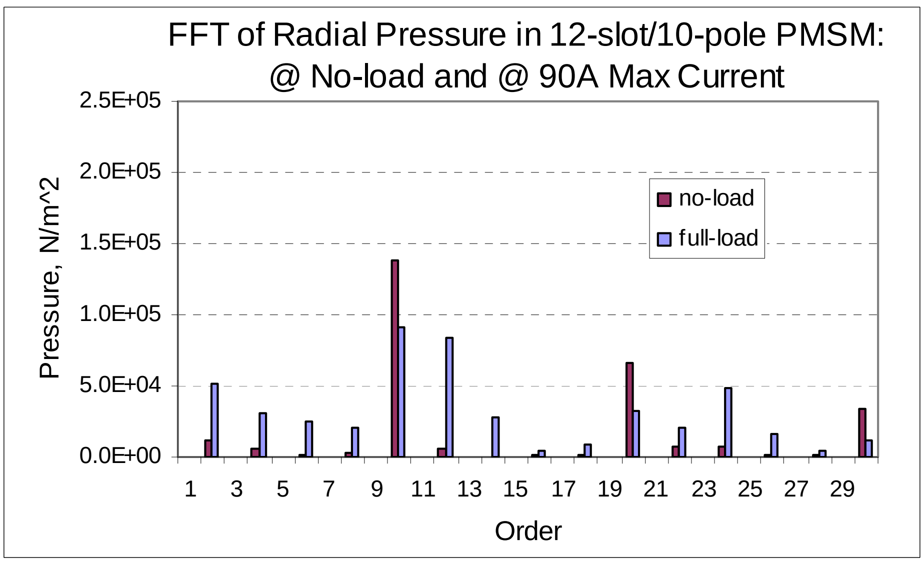

(d)

Figure 5.7: Radial pressure (a) variation at full-load vs. no-load in a 9-slot/6-pole (b) variation at full-load vs. no-load in a 12-slot/10-pole PMSM (c) FFT of radial pressure for 9-slot/6-pole (d) FFT of radial pressure for 12-slot/10-pole. (continued)

under full-load along with other even orders like 4th, 6th, 8th etc. (Fig. 5.7d). In the other non-modular PMSMs with 12-slot/8-pole, and 27-slot/6-pole configurations, the lowest order of mode becomes the 4th, and 3rd orders, respectively. In general, the low order modes in non-modular types are higher than the low order modes in modular type machines. This means the corresponding resonance frequencies in the former type will be much higher than the resonance frequency for the latter types. In addition, the radial pressure amplitudes for the 3rd and 4th order frequencies are smaller than the amplitude for the 2nd order. Both phenomena lead towards less vibration in the non-modular type machines. The distinguishing outcome of these results is the presence of the lowest order of frequency in radial pressure for certain slot/pole combination in PMSMs. These results also identify how the mode orders are affected in full-load than in no-load. The lower order mode in modular machines with full-load remains the same as compared to no-load. Whereas the lower order mode reduced to pole-pair frequency with full-load from pole frequency at no-load in non-modular machines. The next section discusses the displacement of the stator ring and vibration of the motor due to radial pressure.

The analytical equation in (5.8) contains two constant stress terms; one due to stator mmf and the other due to rotor field. There is a also variable stress term due to the product of stator mmf and rotor field. Under no-load conditions, the stator excitation is zero and the constant stress due to stator mmf as well as the variable stress is zero. Under load conditions, both the constant stress and the variable stress have non zero values. Therefore, the DC component of stress under no-load should be less than the DC component of stress with stator excitation.

The alternating component of the stress is due to the interaction of rotor and stator fields. In a PMSM, both the stator and the rotor field variations are assumed to be sinusoids with fundamental frequencies equal to the number of stator poles and the number of rotor poles, respectively. Therefore, the stress terms contains a fundamental mode frequency equal to the differences between the stator and the rotor poles and several other sub-harmonics of the fundamental. This explains the harmonics in radial pressure under full-load as given in Figs. 5.7(c) and (d).

The glitches in the FE results (Fig. 5.7) are due to finite element mesh and are of very high frequency. The frequencies of interest from noise point of view are very low frequencies and those high frequency glitches have no influences at all.

5.4.3. Mode Shapes and Radial Force under No-load and Full-load Conditions

The magnetic radial force, circumferential mode frequencies, radial deflections, stator vibration, and noise power level are all functions of machine geometry, configuration and material properties. The radial force distribution on the stator teeth for a modular and two non-modular machines under no-load condition are shown in the radar plots of Fig. 5.8. All the tooth forces of a machine are assumed as vectors acting along the tooth centre lines with corresponding force magnitudes at any instant and the tip of the vectors are connected to create the radar plots. The force distribution thus obtained should be moving in space as the motor rotates. The distribution clearly shows a mode frequency of 2 in the modular machine without the stator being excited and mode frequencies of 6 and 8 in the non-modular machines.

The radar plots given in Fig. 5.9 explain the radial force variation for all four motor configurations under full load condition. These clearly show how the frequency of the force waves change from no-load to full-load conditions in relation to modular and non-modular machines. Clearly, the force waves resemble with the pressure waves as explained in the previous section with regards to the frequency contents.

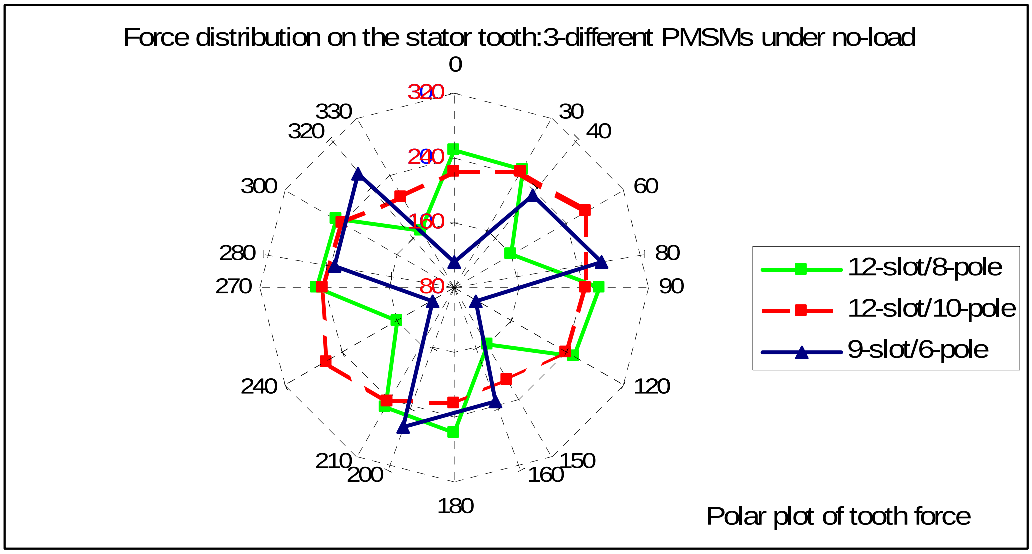

Figure 5.8: Space distribution of Radial force on stator teeth for a Modular machine (12-slot/10-pole) and two Non-modular machines (12-slot/8-pole and 9-slot/6-pole).

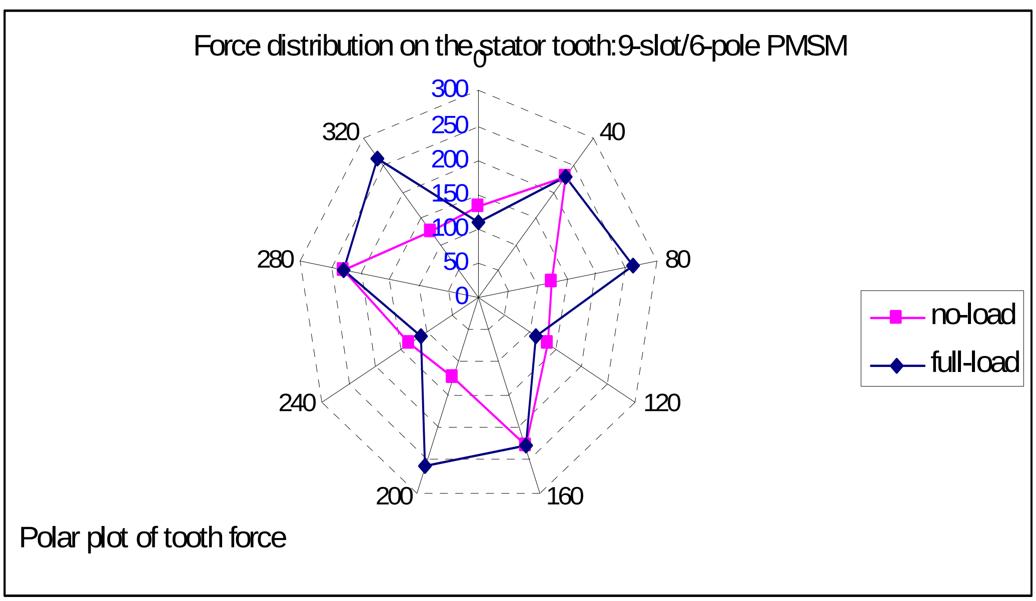

a(i)

Figure 5.9: Radial force distribution on stator teeth (a) non-Modular machines like (i) 9-slot/6-pole with mode ‘3’ (ii) 12-slot/8-pole with mode ‘4’ (iii) 27-slot/6-pole with mode ‘3’ (b) Modular machine like 12-slot/10-pole with mode ‘2’.

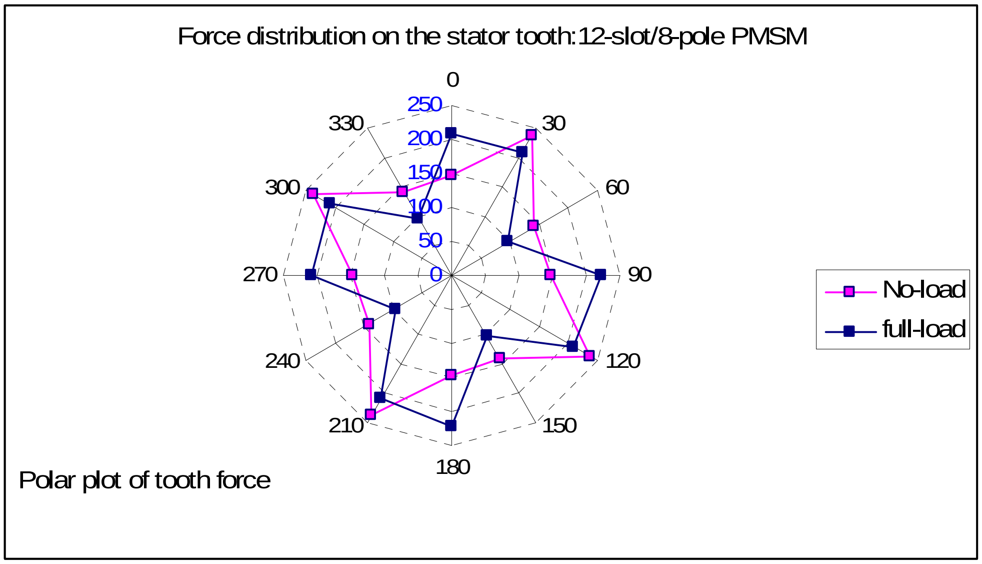

a(ii)

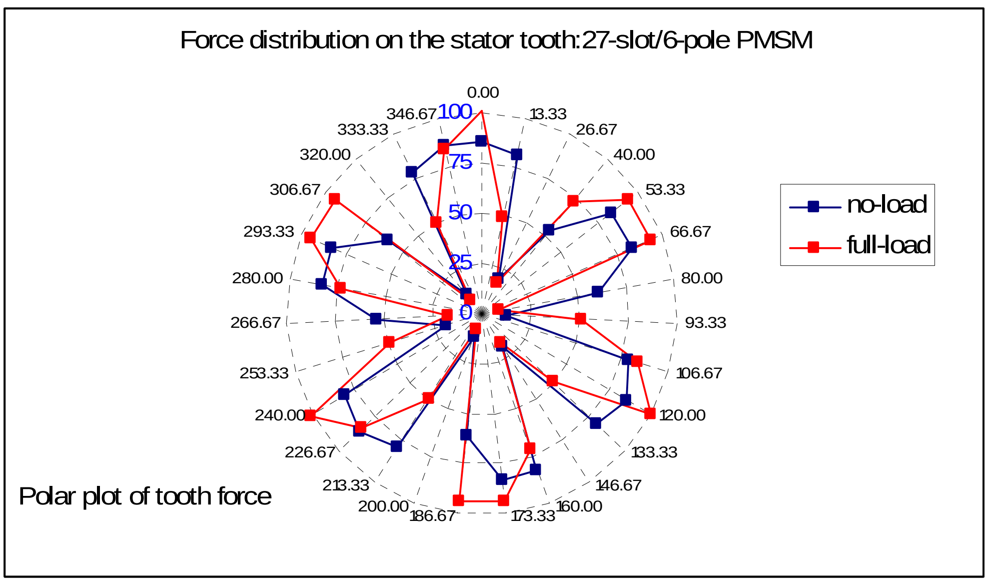

a(iii)

Figure 5.9: Radial force distribution on stator teeth (a) non-Modular machines like (i) 9-slot/6-pole with mode ‘3’ (ii) 12-slot/8-pole with mode ‘4’ (iii) 27-slot/6-pole with mode ‘3’ (b) Modular machine like 12-slot/10-pole with mode ‘2’.(continued)

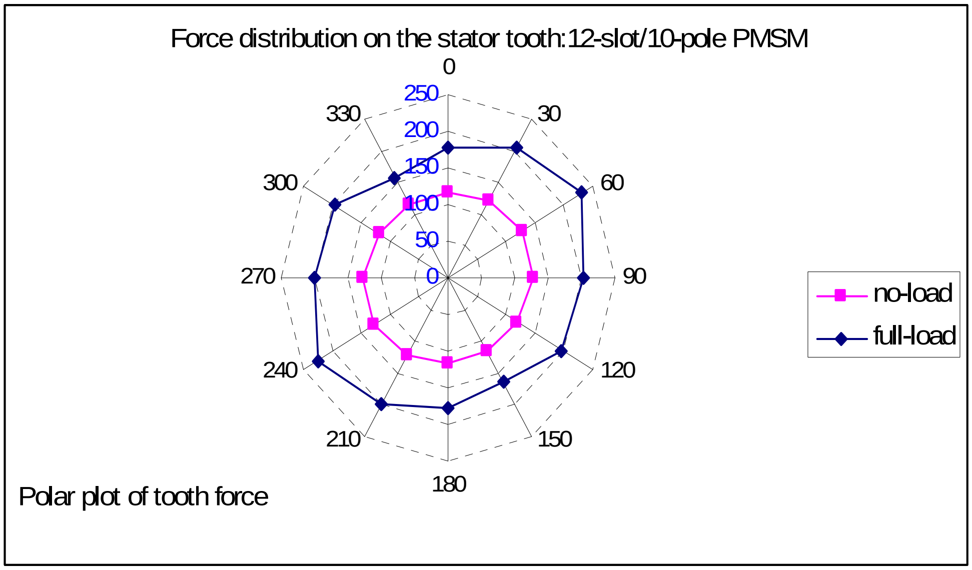

(b)

Figure 5.9: Radial force distribution on stator teeth (a) non-Modular machines like (i) 9-slot/6-pole with mode '3' (ii) 12-slot/8-pole with mode '4' (iii) 27-slot/6-pole with mode '3' (b) Modular machine like 12-slot/10-pole with mode '2'.(continued)

5.5 Radial Displacement

An analytical model of the motor structure will be developed in this section. The results of radial forces by FEA tool will be used in the analytical model to determine the displacement on the outer periphery of the stator. The results of the analytical model will be validated by comparing displacement results obtained from structural finite element analysis software.

5.5.1 Analytical Model

The stator can be considered as a cylinder body with restrained ends. The cross sectional dimensions of the devices are shown in Fig. 5.10(a). The inside radius (stator airgap) of the cylinder is R_{gs} , and the outside radius is R_{out}. Let the internal pressure in the cylinder be P_i which is equal to the radial force per unit stator area (P_r) developed in section 5.3 (equations 5.8 through 5.10); the outside or external pressure is P_0. The problem can be solved using cylindrical coordinates. Every ring of unit thickness measured perpendicular to the plane of the paper is stressed alike. A typical infinitesimal element of unit thickness is defined by two radii, r and $r+dr$, and angle θ, as shown in Fig. 5.10(b). Normal radial and tangential stresses acting on the infinitesimal element is also shown in the same figure. The assumptions made in developing this model are as follows:

- If every element at the same radial distance from the centre is stressed alike, no shear stresses act on the element. One exception to this is that slot might not be stressed alike.
- The axial stresses σ_x on the two faces of the element are equal and opposite. They act normal to the plane of the paper and cancel each other.

The stress and strain equations applied to this problem are [51],

$$\begin{aligned}
\sigma_r &= \frac{E}{(1+v)(1-2v)}[(1-v)\varepsilon_r + v\varepsilon_t]. \\
\sigma_t &= \frac{E}{(1+v)(1-2v)}[v\varepsilon_r + (1-v)\varepsilon_t] \\
\varepsilon_r &= \frac{1}{E}(\sigma_r - v\sigma_t - v\sigma_x) \\
\varepsilon_t &= \frac{1}{E}(-v\sigma_r + \sigma_t - v\sigma_x) \\
\varepsilon_x &= \frac{1}{E}(\sigma_x - v\sigma_r - v\sigma_t)
\end{aligned} \tag{5.13}$$

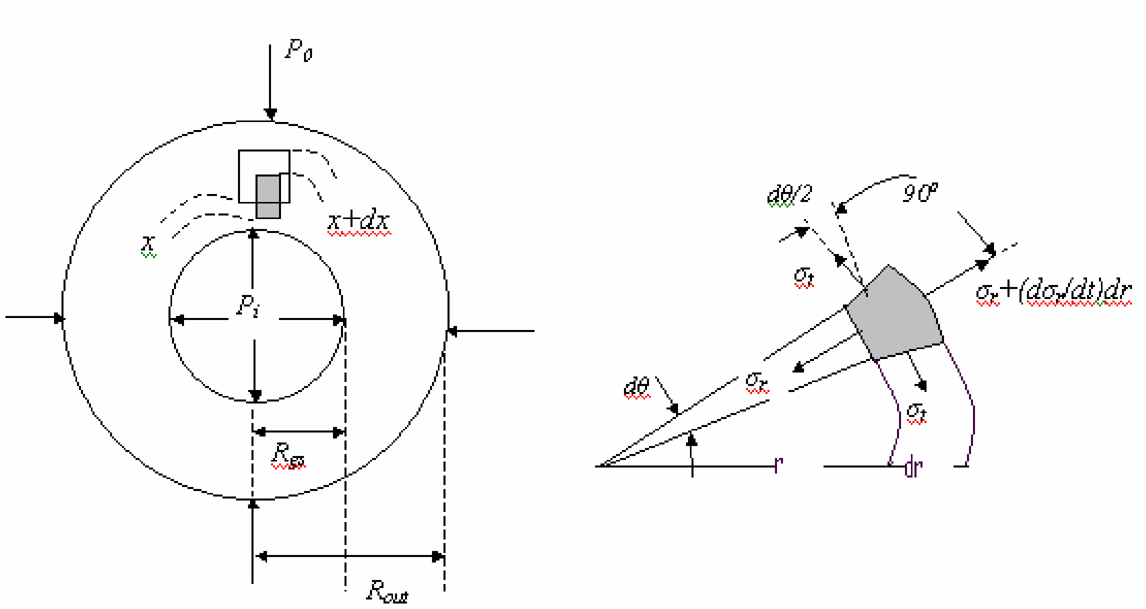

(a) (b)

Figure 5.10: Cylindrical shape of stator with a cross sectional view.

According to the assumption that the ends are restrained, the axial strain can be neglected. With $\varepsilon_x = 0$ and combining the expressions in (5.13) with the strain relationships along the radial and tangential directions $\varepsilon_r = \frac{dx}{dr}$ and $\varepsilon_t = \frac{x}{r}$, the stress equations can be simplified as

$$\sigma_r = \frac{E}{(1+v)(1-2v)}[(1-v)\frac{dx}{dr} + v\frac{x}{r}] \tag{5.14a}$$

$$\sigma_t = \frac{E}{(1+v)(1-2v)}[v\frac{dx}{dr} + (1-v)\frac{x}{r}] \tag{5.14b}$$

Our interest is on the normal radial stress σ_r and the radial displacement x due to this stress for estimating vibration and noise. The condition of static equilibrium is then applied by summing the forces along a radial line and setting it equal to zero,

$$\sum F_r = 0 \tag{5.15}$$

The force on the element of unit thickness is calculated as the product of stress and area of the element cross section. Therefore, the equilibrium condition in (5.15) can be simplified as

$$\sigma_r.r.d\theta + 2.\sigma_t.dr.(\frac{d\theta}{2}) - (\sigma_r + \frac{d\sigma_r}{dr}.dr)(r+dr).d\theta = 0$$

$$\Rightarrow \frac{d\sigma_r}{dr} + \frac{\sigma_r - \sigma_t}{r} = 0 \tag{5.16}$$

Combining the relationships in (5.14) and (5.16) and after simplification the following differential equation can be obtained to estimate radial displacement x:

$$\frac{d^2x}{dr^2} + \frac{1}{r}\frac{dx}{dr} - \frac{x}{r^2} = 0 \tag{5.17}$$

The details of this derivation can be found in Appendix-E. The general form of solution to the differential equation in (5.17) for radial displacement at any point on the cylinder is

$$x = A_1 r + \frac{A_2}{r} \tag{5.18}$$

where the constants A_1 and A_2 can be determined by applying the boundary conditions of the body

$$\sigma_r(R_i) = -P_i \quad \text{and} \quad \sigma_r(R_o) = -P_o \ .$$

For simplicity the outside pressure on the cylinder, P_o is considered negligible compared to the pressure on the inside cylinder. The final form of the constants are found to be

$$A_1 = \frac{(1+\nu).(1-2\nu)}{E}.\frac{P_i.R_i^2}{(R_o^2 - R_i^2)} \quad \text{and} \quad A_2 = \frac{(1+\nu)}{E}.\frac{P_i.R_i^2.R_o^2}{(R_o^2 - R_i^2)} \tag{5.19}$$

Here, P_i is the maximum internal pressure on the tooth given as $P_{r,max}$ in (5.8). The constants A_1 and A_2 when used in (5.18) give the radial displacement of any point on the elastic cylinder subjected to the specified pressure.

5.5.2. Estimation and Validation of Radial Displacement

Separate calculations are carried out to find the displacements on the inner surface of the tooth and the outer surface of the stator cylinder on a radial line according to (5.18). If the displacement on the inside edge of a tooth is x_{in} and the displacement on the outer edge of the stator ring along that tooth is x_{out}, then the differences between these two are the estimate for net displacement along that line. Any displacement due to stator vibration from the end caps, bearings, gears etc. are not considered in this model.

$$x = x_{in} - x_{out} \tag{5.20}$$

Estimation by Analytical Model

The radial pressure obtained from FE analysis (using Flux 2D) is used in the analytical model to calculate the radial displacement x. Here, the radial pressure at the low order mode is used as the maximum value of tooth pressure for a particular motor topology. The displacement results for the four PMSMs with different slot/pole combinations are given in Table 5.2.

Table 5.2 Analytical calculation of radial displacement

12-slot/10-pole		9-slot/6-pole		27-slot/6-pole		12-slot/8-pole	
P_{max}, N/m^2	Disp, µm	P_{max}, N/m^2	Disp, µm	P_{max}, N/m^2	Disp, µm	P_{max}, N/m^2	Disp, µm
4.07x10^5	4.1	3.77x10^5	1.9	3.36x10^5	1.8	4.27x10^5	2.1

Validation by Structural FEA Model

The displacement data shown in Table 5.2 is calculated based on the maximum pressure experienced by any tooth at an instant of time. However, structural FE analysis can be carried out to estimate displacements on the stator outer periphery at several node points under various cases. The structural finite element analysis (using ANSYS) is done at several locations on the stator housing of a 12-slot/10-pole machine to compare with the analytical data. The nodes are taken along the centre line of each tooth as demonstrated in Fig. 5.11 where F1 through F12 represent the tooth forces that varies with phase currents. These tooth forces are the oscillating portion of radial forces acting on each tooth in one complete cycle. There are only 6 variations for 12 tooth forces (Fig. 5.12) as the diagonally opposite tooth pair (such as F1-F7 and F2-F8) forces go through the same magnetic stress. The FEA results of forces and pressures for the six set of tooth forces under six different cases are given in Table 5.3. The pressure values for any particular case when used as input to a structural FEA model in ANSYS can determine the displacements (in mm) at the 12 node points on the stator outer periphery (as marked in Fig. 5.11). All six columns (case I through case VI) in Table 5.4 are completed with

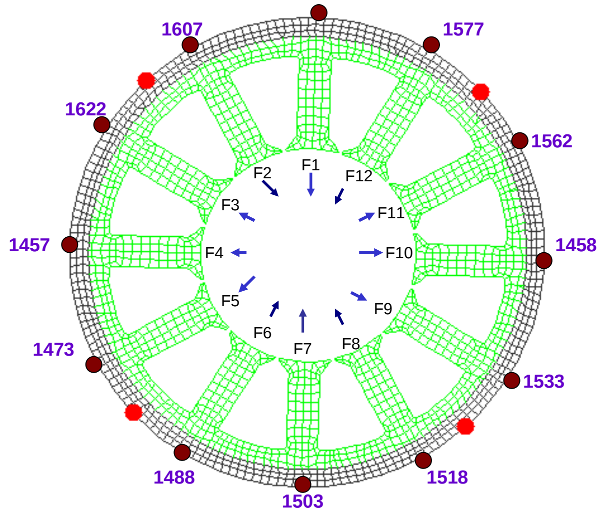

Figure 5.11: Structural analysis model showing tooth forces and test nodes for displacement measurement.

Table 5.3: Six different cases of tooth forces and corresponding tooth pressures

		F1-F7	F2-F8	F3-F9	F4-F10	F5-F11	F6-F12
	AVG	171.607	186.627	173.194	187.676	171.932	186.589
Case-1	Force(N)	247.391	244.719	126.599	98.815	143.604	218.571
	Force-AVG	75.784	58.092	-46.595	-88.861	-28.328	31.982
	Pressure(N/mm^2)	0.1146	0.0879	-0.0705	-0.1345	-0.0429	0.0484
Case-2	Force(N)	219.3025	277.161	189.5802	132.036	106.612	147.687
	Force-AVG	47.695	90.534	16.386	-55.64	-65.32	-38.902
	Pressure(N/mm^2)	0.0722	0.137	0.0248	-0.0842	-0.0988	-0.0589
Case-3	Force(N)	146.604	218.571	247.391	244.719	126.599	98.815
	Force-AVG	-25.003	31.944	74.197	57.043	-45.333	-87.774
	Pressure(N/mm^2)	-0.0378	0.0483	0.1123	0.0863	-0.0686	-0.1328
Case-4	Force(N)	106.612	147.687	219.302	277.161	189.58	132.036
	Force-AVG	-64.995	-38.94	46.108	89.485	17.648	-54.553
	Pressure(N/mm^2)	-0.0984	-0.0589	0.0698	0.1354	0.0267	-0.0826
Case-5	Force(N)	126.599	98.815	143.604	218.571	247.391	244.719
	Force-AVG	-45.008	-87.812	-29.59	30.895	75.459	58.13
	Pressure(N/mm^2)	-0.0681	-0.1329	-0.0448	0.0468	0.1142	0.0879
Case-6	Force(N)	189.58	132.036	106.612	147.687	219.302	277.161
	Force-AVG	17.973	-54.591	-66.582	-39.989	47.37	90.572
	Pressure(N/mm^2)	0.0272	-0.0826	-0.1008	-0.0605	0.0717	0.1371

displacement values from this structural FEA. The displacement results from this FEA are comparable to the displacement result obtained from analytical model in a 12-slot/10-pole machine.

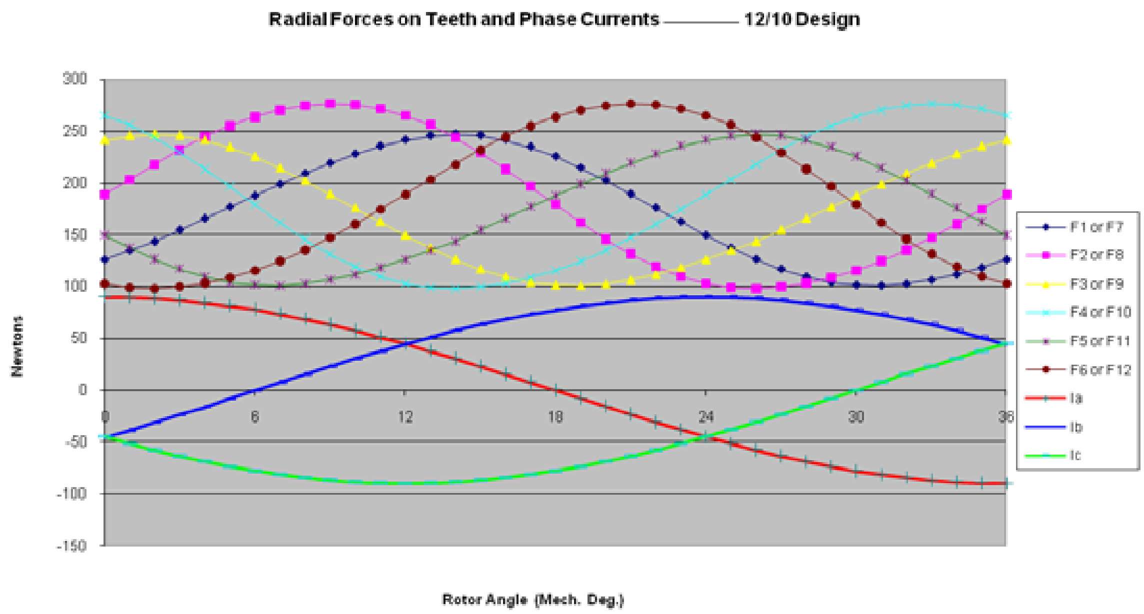

Figure 5.12: Variation in tooth forces with respect to phase currents.

Validation by Experimental Results

Four accelerometers are mounted at 4-different nodes 90˚ apart on the outer periphery of a 12-slot/10-pole motor in a dyno stand. These nodes are marked as 1592, 1457, 1503, and 1458 respectively (Fig. 5.13) to replicate some of the nodes in the structural model in Fig. 5.11. As the analysis showed that the lower mode in 12-slot/10-pole motor is to be 2, the stator will go through some form of ovulation. Thus, the maximum displacement or stator deformation will be along the perpendicular axis of the stator ring. Therefore, the accelerometers at those points can capture the maximum displacement at all time.

Table 5.4: Radial displacement on 12 distinct nodes on the housing surface @ 6-different instants for a 12-slot/10-pole PMSM @ full-load

	Displacement-Magnitude (mm)					
Node	Case1	Case2	Case3	Case4	Case5	Case6
1592	4.72E-03	1.31E-03	5.59E-03	5.34E-03	1.78E-03	5.32E-03
1607	2.80E-03	2.83E-03	3.16E-03	2.85E-03	3.04E-03	3.07E-03
1622	3.19E-03	7.51E-04	4.67E-03	3.53E-03	1.71E-03	4.31E-03
1457	5.34E-03	3.58E-03	3.03E-03	5.06E-03	2.87E-03	2.42E-03
1473	2.99E-03	4.46E-03	1.58E-03	2.26E-03	4.52E-03	2.19E-03
1488	3.47E-03	3.03E-03	3.39E-03	3.20E-03	3.09E-03	3.09E-03
1503	6.01E-03	6.36E-03	1.83E-03	4.77E-03	5.97E-03	2.20E-03
1518	4.08E-03	7.91E-03	4.87E-03	2.31E-03	8.34E-03	6.12E-03
1533	3.47E-03	5.43E-03	6.87E-03	3.69E-03	6.30E-03	7.40E-03
1458	5.55E-03	5.62E-03	4.82E-03	5.17E-03	5.58E-03	5.25E-03
1562	3.23E-03	6.99E-03	5.30E-03	2.46E-03	7.59E-03	6.42E-03
1577	2.18E-03	4.38E-03	7.63E-03	3.76E-03	5.77E-03	8.08E-03

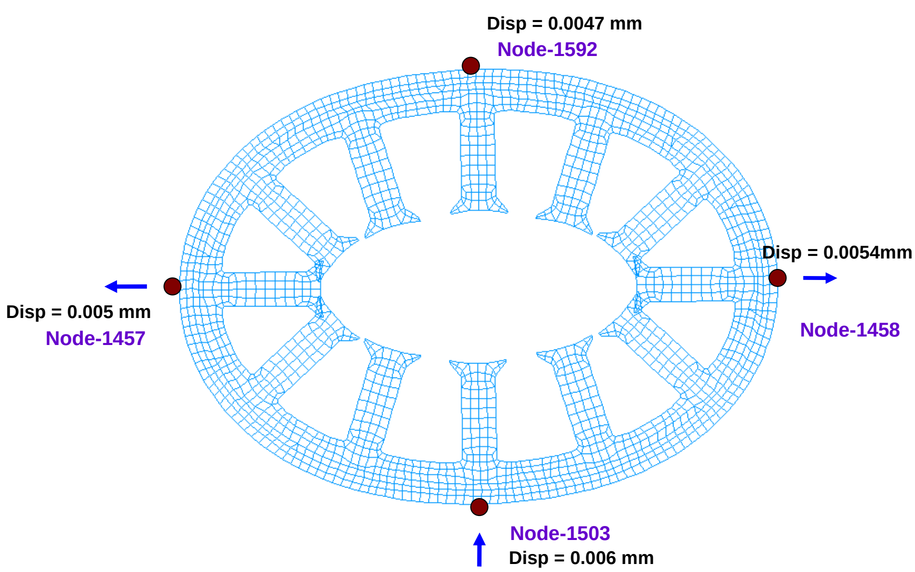

Figure 5.13: Radial displacement measured at 4-orthogonal locations on the stator housing.

The accelerometer test results (at 4 node points marked in Fig. 5.13) match very closely with the structural FE data given in Table 5.4 for the same nodes. Again, the structural FE data matches the analytical data. Therefore, the analytical method developed in this chapter gives a valid approach of estimating radial force and pressure and displacements through modeling, and hence, avoiding experiments.

5.6 Vibration and Noise due to Radial Displacement

Magnetic stress under faulty conditions or due to unbalances can cause deflections on the structure of a PMSM. As the ends of these machines are restrained, the bending or the torsion can be neglected. It is then the circumferential mode that dictates the mode frequency and vibration due to this stress. Following statements are true in relation to noise and vibration in these machines.

- Bending, torsional and other out-of-plane modes contribute to vibrations under unbalanced or faulty situations.
- The vibrations in torsional, radial and bending modes can be considered unlikely to occur assuming that the ends of the stator structure are stiffly supported and clamped to the legs.
- Circumferential modes are important in the electromagnetic vibration.
- Frequency content of the magnetic radial force is essentially the excitation frequency.

Based on the assumptions made above, the natural mode frequency, the excitation frequency and the condition of resonance are calculated.

Vibration due to the magnetic forces is a natural phenomenon of machine operation. The radial vibration of stator of a PMSM is initiated when the magnetic radial pressure causes radial displacement of the stator structure. As a matter of fact, radial displacement is a direct measure of machine vibration.

The motor shaft is also deflected by the magnetic force in the motor. The deflection produces a corresponding increase in the magnetic forces between rotor and stator, which in turn is applied to the motor bearings. The deflection of the shaft produces an eccentricity between the rotor center of mass and the rotating centerline. The rotor eccentricity causes unbalanced forces that increase bearing loading and machine vibration.

5.6.1 Condition of Maximum Vibration

The maximum vibration occurs at the condition of resonance when the machine excitation frequency matches with its natural mode frequency. The excitation frequency (f_{exc}) is an integer multiple of the machines rotational frequency (f_p) given by [47]

$$f_{exc}(n) = nf_p = \frac{n\omega_r N_p}{120} \; ; n = 1, 2, 3 \ldots\ldots \qquad (5.21)$$

where N_p is the number of rotor poles. On the other hand, the natural mode frequencies (f_m) are mainly a function of stator dimensions [22]. Natural mode frequencies for several modes can be calculated using the equations given in the following section.

5.6.2 Calculation of Natural Mode Frequency

Several basic methods of calculating the natural mode frequencies (f_m) can be found in [25, 43-47, and 52]. First, the stator is considered as a freely vibrating ring and then masses of the teeth and winding were considered to account for the stator structure. Finally, the effects of shear and rotary inertia were considered to develop formulas for the crude approximation of the mechanical mode frequencies [22]. The mode zero frequency is given by

$$f_{(m=0)} = \frac{1}{2\pi R_m} \cdot \sqrt{\frac{E}{\rho_s . \Delta}} \tag{5.22}$$

Here $R_m = \dfrac{R_{out} + (R_{out} - w_{bi})}{2}$; $\Delta = 1 + \dfrac{W_t}{W_y}$; $W_t = W_P + W_w + W_i$.

E is the young's modulus of elasticity of stator material in N/m^2 , ρ_s is the density of the material in Kg/m^3, W_t is the total weight of the stator comprised of tooth, windings and insulation weights.

The frequency of mode 1 is given by

$$f_{(m=1)} = f_{(m=0)} \cdot \sqrt{\frac{2}{1 + i^2 . \Delta / \Delta_m}} \tag{5.23}$$

Here $\Delta_m = 1 + \dfrac{1.91.N_S . A_{SP} . d_s^3 . W_t}{R_m . L_{stk} . y_s^3 . W_P} [\frac{1}{3} + (\frac{y_s}{2.d_s}) + (\frac{y_s}{2.d_s})^2]$; $i = \dfrac{1}{2.\sqrt{3}} \cdot \dfrac{y_s}{R_m}$

The frequencies for mode 2 and higher can be calculated by the following

$$f_{(m \geq 2)} = \frac{f_{(m=0)} . i . m(m^2 - 1)}{\sqrt{\{(m^2 + 1) + i^2 . (m^2 - 1)(4m^2 + m^2 . \Delta_m / \Delta + 3)\}}} \tag{5.24}$$

where m represents the mode number. The nomenclatures of equations (5.22) through (5.24) are given in the "Glossary of Symbols" at the beginning of this dissertation.

The natural mode frequencies for all four motor configurations have been calculated at several rotational speeds of the rotor and listed in Table 5.5. The dominant mode numbers are 3, 2, 4, and 3 for a 9-slot/6-pole, 12-slot/10-pole, 12-slot/8-pole, and 27-slot/6-pole motors, respectively. The corresponding mode frequencies are determined by (5.22) and tabulated in Table 5.6. For the 12-slot/10-pole motor, the mode frequency (393.47 Hz) matches with about 5 times the excitation frequency at 1000 rpm (83.33 Hz). Whereas,

Table 5.5: Excitation frequency calculation at different rotational speed

Rotational speed, rpm	Rotational freq for different Motor configurations (f_p),Hz				Excitation freq., Hz ($n.f_p$) in mechanical
	9s6p	12s10p	12s8p	27s6p	
500	Elect.: 25	41.66	33.33	25	8.33, 16.67, 25, 33.33, 41.66, 50, 58.33, 66.64, 75, 83.33, 91.63, 100,……
	Mech.: 8.33	8.33	8.33	8.33	
1000	Elect.: 50	83.33	66.67	50	16.67, 33.33, 50, 66.64, 83.33, 100, 116.62, 133.28,…
	Mech.: 16.66	16.66	16.66	16.66	
2000	Elect.: 100	176.64	133.34	100	33.33, 66.64, 100, 133.33, 166.67, 200, 233.33,……
	Mech.: 33.33	33.33	33.33	33.33	
4000	Elect.: 200	353.28	266.68	200	66.64, 133.33, 200, 266.64, 333.2, 400, 466.67,……
	Mech.: 66.67	66.67	66.67	66.67	

for 9-slot/6-pole, 27-slot/6-pole and 12-slot/8-pole motors, the mode frequencies are too high to match with the excitation frequency. This is a direct indication of how a machine with lower order mode enters into resonance easily and becomes noisy.

Table 5.6: Mode frequency calculation

Mode number of interest	Mode frequency for several motor configuration, Hz			
	9s6p	12s10p	12s8p	27s6p
0		4911.7		
1				
2		393.47		
3	1027.95			1027.95
4			1801.53	

5.6.3 Acoustic Noise and Sound Power Level

The analytical values of radial displacements for all the motors of interest in this research are given in Table 5.2 when the corresponding lower order modes are excited. Radiated noise can be estimated from these displacement results using their relationship with sound energy. The sound power in watts and dB can be obtained from the following equations [25 and 52];

$$L_w = 10.\log\{\frac{2.P_s}{P_{sref}}\} \tag{5.25}$$

$$P_s = 4.\sigma_{rel}.\rho.c.\pi^3.f_{exc}^2 x^2.R_{out}.L_{stk}$$
$$\sigma_{rel} = \frac{k^2}{1+k^2} \tag{5.26}$$
$$k = \frac{2\pi R_{out} f_{exc}}{c}$$

Here, P_s is the sound power in watts radiated by an electric machine for a particular excitation frequency, L_w is the value of the sound power converted in dB with a reference sound level of P_{sref}, and σ_{rel} is the relative sound intensity.

The radial displacements are higher in a 12-slot/10-pole motor compared to other candidate motors of this research. The radiated acoustic noise will follow the same trend. The values of sound power level due to radial vibration are listed in Table 5.7. The decibel level for average conversation is around 60 dB and for the average radio and vacuum cleaner is around 75 dB. The sound power levels listed in the following table can be compared with these phenomena. A brief listing of sound intensity levels of some familiar sources can be found in Appendix-F.

Table 5.7: Sound power level due to radial displacement in 4-different PMSMs

Quantity	9-slot/6-pole	12-slot/10-pole	12-slot/8-pole	27-slot/6-pole
Radial displacement, μm	1.9	4.1	2.1	1.8
Sound level, dB	65.13	76.25	68.50	61.7

5.7 Conclusions

A few researchers have identified the electromagnetic radial force as the main cause of vibration in PM machines and experimentally determined the mechanical deformation and vibration without developing a machine model [13]. This research developed an analytical machine model to determine radial deformation using radial pressure as an input to the model. The radial deformation thus calculated can be used to estimate noise and vibration in different PMSM configurations.

Several researchers show that the reduction of cogging torque and mutual torque ripple ultimately reduce the unacceptable speed ripple, and hence, the vibration and acoustic noise [1-7, 15-17]. These works did not establish any fundamental relationship between torque ripple or cogging torque with noise and vibration. This research showed that the root cause of noise and vibration is the radial forces not the torque ripples. This dissertation contributed to both theoretical and numerical analysis of vibrations of magnetic origin in a PMSM. First, the exciting magnetic forces are studied with respect to their distribution in time and space by determining the time harmonic and spatial orders of the forces in relation to 12-slot/10-pole and 9-slot/6-pole motor topologies. Furthermore, a 2D FE tool is used to calculate the radial forces on the stator teeth. Then the analytical model of the machine describing vibration behavior has been developed. A static solution by the analytical model for that radial force value gives the radial displacement of a tooth pair. Finally, the radial displacement or vibration is converted to audible noise using sound energy equations [15, 52].

There are several ways to reduce radial forces. Flux can be decreased, air gap area can be increased, air gap symmetry can be improved, and the stator's lateral stiffness can be increased. The flux reduction method will also reduce the average output torque; the increased air gap will require a stronger or larger magnet to maintain the same torque level. This research investigated the root cause of radial force variation with variation in slot-pole combinations; some motor topologies were found to be better than others in terms of radial force and lower vibration.

In modular machines, the flux-linkage per coil and the torque density are high, since the coil-pitch is approximately equal to the pole-pitch. Also the cogging torque is very small because of the fractional ratio of slot number to pole number and the fact that the least common multiple (LCM) between the number of slots and poles is large. The higher the value of LCM, the higher is the frequency of cogging; consequently, the lower is the amplitude of cogging torque. However, one disadvantage is that such machines exhibit an unbalanced magnetic force and result in excessive acoustic noise and vibration [21]. In spite of the manufacturing advantages, and low cogging torque and torque ripple shown by the modular PM machines, they are not an attractive candidate due to the increased unbalanced radial forces and acoustic noise. On the other hand, non-modular machines with symmetrical stator windings are not as good as modular ones in terms of cogging torque, torque density, and torque ripple. However, they are the better candidates for applications requiring less noise and vibration.

CHAPTER VI

SUMMARY AND FUTURE WORK

This chapter summarizes the advances on permanent magnet machines accomplished through this research along with suggested future works. The summary section 6.1 gives a brief description of the research presented in this dissertation and section 6.2 discusses the relevant issues that still need to be addressed in the future.

6.1 Summary

The permanent magnet machines are an attractive solution for compact machines with higher efficiency and higher torque-to-volume ratio. Such machines are now in great demand in many applications including the automotive steering application. These applications also require quiet machine operations, which mean a lower level of cogging torque and torque ripple and reduced noise and vibration.

The geometry, operation, brief classification, and few applications of PMSMs were presented in chapter I. The key requirements for quiet operation have been identified as cogging torque, torque ripple, and unbalanced radial forces; the research objectives to address these issues have been outlined in the introductory chapter.

An extended literature review on torque ripple, cogging torque, and magnetic stress is presented in chapter II. The existing literature regarding the reduction of cogging torque, torque ripple, and radial vibration in PMSMs both by design methods and control techniques have been presented. The design based methods for improving cogging torque, torque ripple and radial vibration were discussed in detail identifying the shortcomings in the existing literature. A brief organization of the dissertation is also included in this chapter.

Chapter III laid out a comprehensive design procedure for PM machines. The design methodology was utilized to develop analytical designs for four different motor topologies with different slot/pole combinations. Analytical design obtained for these motor configurations were for a given common set of performances and design constraints. FE analysis was also carried to validate the results of the analytical models. An example design showed the effectiveness of these analytical models in predicting the performance of the machines.

Chapter IV discusses the effects of pole shaping and skewing on cogging torque and torque ripple of PM machines. Both FEA and test results are included to show the comparison for several PMSM configurations. The effect of slot/pole combinations and magnet shapes on the magnitude and harmonic content of torque waveforms in a PMSM drive have been studied. Finite element analysis (FEA) and experimental results show that for certain magnet designs and a configuration skewing does not necessarily reduce the ripple in the electromagnetic torque, but may cause it to increase.

Low acoustic noise and high efficiency operation is quite normal for PM machines; the vibration behavior of such a machine is mostly dependent on its slot-pole configuration. The vibration also depends on the winding arrangement in some cases. However, vibrations can be reduced by adjusting the internal dimensions of the machine. A vibration model for PMSM to predict the radial displacement in different motor configurations is developed in Chapter V. The characteristics predicted from the vibration model helps adjust the internal dimensions to design a motor with low acoustic noise.

Careful considerations of all the design parameters are needed during the design iterations to ensure that all the design requirements are satisfied. Motor topology selection is an important step. There are motor topologies with slot-pole combinations that reduce torque ripple but generate higher radial force. For instance, 12-slot/10-pole motor has less cogging torque and torque ripple compared to 9-slot/6-pole motor, but the unbalanced radial forces are higher in 12-slot/10-pole motors than in 9-slot/6-pole motors.

6.1.1 Research Contributions

This dissertation research contributes towards the advancement and knowledge in the area of noise and vibration in PM machines. The particular contributions can be summarized as:

- *The use of non-traditional arc magnets for a surface mounted PMSM:* The concept of pole shaping to create non-traditional arc magnet has been introduced. The magnet pole shaping resulted in cogging torque improvements.

- *Adopting appropriate skew scheme based on the PMSM configuration:* The research revealed that some of the motor configurations have strong influence on cogging torque and torque ripple with step-skew. Some motor configurations have an increase in torque ripple even after skew if the skew scheme and/or the motor topology are not selected appropriately.

- *Slot-pole combination selection to reduce vibration.* For certain PMSM slot/pole combinations the scope of reducing vibration is limited due to their low order mode frequencies. Certain slot/pole combinations in PMSMs demonstrate better acoustic performance due to less likelihood of having unbalanced radial forces and smaller tooth displacement caused by these forces. The tooth displacement calculated by the analytical model developed for vibration shows that a tooth in a 12-slot/10-pole motor is displaced more than a tooth in a 9-slot/6-pole motor.

- *Design techniques to modify mode frequencies.* A design technique to modify the mode frequency for a particular motor has been developed. The comprehensive design method explains how the stator back iron, when dimensioned appropriately, can modify the mode frequency. Increase in the frequency levels of the lower order modes help reducing vibrations.

- *Modular, non-modular, and asymmetrical winding.* Certain mode frequencies can be modulated by adopting different winding techniques (e.g. non-modular type distributed winding replacing modular type concentrated winding). However, this doesn't guarantee the elimination of vibration in motor topologies like 12-slot/10-pole or 6-slot/4-pole, as these motors have mode '2' even without the motor being excited. The FE calculation of radial pressure and its frequency with and without load for a 12-slot/10-pole motor clearly showed this phenomenon.

6.2 Future Works

The following research works are suggested to be carried out in the future in this area of PMSM design:

- *Tooth shaping rather than pole shaping.* The concept of pole shaping has been presented in this dissertation to reduce torque ripple in fractional slot machines. The method works well especially when the slot-to-pole ratio is 1.5 (for example, 9-slot/6-pole, 12-slot/8-pole). The implementation of the proposed method may be challenging and costly from a manufacturing point of view. Therefore, tooth shaping technique in PMSMs can be studied to examine if it offers the same advantages as that of pole shaping.
- *Continuous skew rather than step-skew.* The step-skew technique discussed throughout the dissertation is limited in its ability to cancel certain frequency components of the cogging torque for a given skew angle. The continuous skew scheme can reduce a particular harmonics as well as all higher order harmonics that are integer multiples of that harmonic. This would be a more effective approach of reducing cogging torque and torque ripple.

- *Structural FEA to capture different mode frequencies at design variations.* The mode frequencies have been calculated by an analytical equation with estimation of the masses of tooth, yoke, insulation, winding etc. for all four PMSM configurations. A structural analysis tool can compute all these masses precisely by dividing the motor geometry into infinitesimal volumes. For a given geometry and given material properties for different parts of the geometry, the structural FE tool would predict those frequencies more accurately.
- *Tests in an anechoic chamber to identify noise: amplitude as well as frequency.* The noise and vibration in PMSMs covered in this research is based on the prediction of dominant mode order and frequency. The developed analytical vibration model was used to determine the radial displacement due to radial vibration. The displacement data was converted into sound energy using analytical equations. Direct noise tests in an *anechoic* chamber can be utilized to validate and improve the analytical model.

REFERENCES

[1] N. Bianchi and S. Bolognani, "Design techniques for reducing cogging torque in surface-mounted PM motors," *IEEE Transactions on Industry Application Society,* issue 5, vol. 38, pp. 1259-1265, Sept-Oct. 2002.

[2] S. M. Hwang and D. K. Lieu, "Reduction of torque ripple in brushless dc motors," *IEEE Transactions on Magnetics*, pt. 2, vol. 31, pp. 3737-3739, Nov. 1995.

[3] S. M. Hwang, et. al., "Various design techniques to reduce cogging torque by controlling energy variation in permanent magnet motors," *IEEE Transactions on Magnetics*, pt. 1, vol. 37, pp. 2806-2809, Jul. 2001.

[4] V. Petrovic, et. al., "Design and implementation of an adaptive controller for torque ripple minimization in PM synchronous motors," *IEEE Transactions on Power Electronics*, vol. 5, pp. 871-880, Sept. 2000.

[5] B. Grcar, P. Cafuta, G. Stumberger, A. M. Stankovic, "Control based reduction of pulsating torque for PMAC machines," *IEEE Transactions on Energy Conversions*, vol. 17, no. 2, Jun. 2002.

[6] G. Jiao, C. D. Rahn, " Field weakening for radial force reduction in brushless permanent-magnet DC motors," *IEEE Transactions on Magnetics*, issue 5, vol. 40, pp. 3286-3292, Sept. 2004.

[7] M. Brackley and C. Pollock, "Analysis and reduction of acoustic noise from a brushless DC drive," *IEEE Transactions on Industry Applications*, issue 3, vol. 36, pp. 772-777, May-Jun. 2000.

[8] P. Vas, *Sensorless Vector and Direct Torque Control*, Oxford university press, New York, 1998.

[9] D. W. Novotny and T.A. Lipo, *Vector Control and Dynamics of AC Drives*, Clarendon press, Oxford, 1997.

[10] M. Joran, "Modeling and control design of VSI-fed PMSM drive systems with active load," *12th Annual Conference Proceedings of APEC*, vol.2, pp. 728-735, Feb. 1997.

[11] J. F. Gieras, C. Wang, J. C. Lao, *Noise of Polyphase Electric Motors*, Taylor & Rancis group, Boca Raton, FL, 2006.

[12] C. Breton, J. Bartolome, J. A. Benito, G. Tassinario, I. Flotats, C. W. Lu, B. J. Chalmers , "Influence of machine symmetry on reduction of cogging torque in permanent-magnet brushless motors," *IEEE Transactions on Magnetics*, vol. 36, pp. 3819-3823, Sept. 2000.

[13] D. Ishak, Z. Q. Zhu, D. Howe, "Unbalanced magnetic forces in permanent magnet brushless machines with diametrically asymmetric phase windings," 40th *IEEE Industry Application Conference*, vol. 2, pp. 1037-1043, Oct. 2005.

[14] S. Huang, M. Aydin, T. A. Lipo, "Electromagnetic vibration and noise assessment for surface mounted PM machines," *IEEE Power Engineering Society*, vol.3, pp. 14127-1426, Jul. 2001.

[15] N. Boules, H. Rassem, N. Chandra, T. W. Nehl, L. Bruno, C. Shaotang., "Torque ripple free electric power steering motor," US Patent No. 6,498,451 , 1995.

[16] R. Carlson, A. A. Tavares, J. P. Bastos, M. L. Mazenc, "Torque ripple attenuation in permanent magnet synchronous motors," *IEEE Industry Application Society*, vol. 1, pp. 57-62, Oct. 1989.

[17] A. Murray, "Torque and EMF ripple reduction in brushless machines," *IEEE Colloquium on Permanent Magnet Machines and Drives*, vol. 1, pp. 8/1-8/4, Feb. 1993.

[18] D. C. Hanselman, *Brushless Permanent Magnet Motor Design*, Writers' collective, Cranston, Rhode Island, 2003.

[19] J. F. Gieras and M. Wing, *Permanent Magnet Motor Technology*, Marcel Dekker, Inc., New York, 2002.

[20] S. Huang, M. Aydin, T. A. Lipo, "Torque quality assessment and sizing optimizing for surface mounted permanent magnet machines," *IEEE Industry Application Society*, Sept. 2001.

[21] F. Magnussen and H. Lendenmann, "Parasitic effects in PM machine with concentrated windings," *40th Industry Application Society Annual Meeting*, vol. 2, pp. 1044-1049, Oct. 2005.

[22] M. N. Anwar, *Design of switched reluctance machines for low-acoustic noise and wide speed range operation*, Dissertation presented to the graduate faculty of the University of akron, 2001.

[23] M. Dai, A. Keyhani, and T. Sebastian, "Torque ripple analysis of a PM brushless DC motor using finite element method," *IEEE Transaction on Energy Conversion,* vol.19, pp. 40-45, Mar. 2004.

[24] Y. Asano,, Y. Honda, H. Murakami, Y.Takeda, S. Morimoto, "Novel noise improvement techniques for a PMSM with concentrated winding," *in Proceedings of the Power Conversion Conference,* vol. 2, pp 460-465, Apr. 2002.

[25] P.L. Timar, *Noise and Vibration of Electrical Machines*, Elsevier, Sept. 2004.

[26] I. Husain, *Electric and Hybrid Vehicles: Design Fundamentals*, CRC press, Boca Raton, FL 2003.

[27] F. Taegen and J. Kolbe, "Vibrations and noise produced by special purpose permanent-magnet synchronous motors in variable frequency operation," *IEEE International Conference on Power Electronics and Drive Systems,* vol. 2, pp. 583-588, Oct. 2001.

[28] D. C. Hamselman, "Minimum torque ripple, maximum efficiency excitation of brushless permanent magnet motors," *IEEE Transactions on Industrial Electronics,* vol. 41, pp. 292-300, June 1994.

[29] D. A. Staton and S. Eric, "Computer aided design of brushless servo motors," *UK Magnetic Society Seminar*, Nov. 2000.

[30] Y. K Chin, W. M. Arshad, T. Backstrom, C. Sadarangani, "Design of a compact BLDC motor for transient applications," *IEEE Electric Machines and Drive Conference, IEMDC,* pp. 743-747, June 2001.

[31] Y. Keno, N. Matsui, "A design approach for direct-drive permanent magnet motors," 40th *IEEE Industry Application Conference*, vol. 1, pp. 245-252, Oct. 2005.

[32] J. R. Handershot and T. J. E. Miller, *Design of Brushless Permanent Magnet Motors.*, Magna physics publishing and Clarendon press, Oxford, 1994.

[33] K. Dong-Hun, P. Il-Han, L. Joon-Ho, K. Cheng-Eob, "Optimal shape design of iron core to reduce cogging torque of IPM motor", *IEEE Transaction on Magnetics*, issue 3, pt. 1, vol. 39, pp. 1456-1459, May 2003.

[34] A. Carlo, C. Domeniko, A. Cristofolini, M. Fabbri, G. Serra, "Application of a multi-objective minimization technique for reducing the torque ripple in permanent-magnet motors," *IEEE Transaction on Magnetics*, vol. 35, no. 5, Sept 1999.

[35] L. Yong, J. Zou, L. Youngping, "Optimum design of magnet shape in permanent-magnet synchronous motors," *IEEE Transaction on Magnetics*, vol. 39, no. 6, Nov 2003.

[36] C. Bi, Z. J. Liu, and T. S. Low, "Analysis of unbalanced magnetic pull in hard disk drive spindle motors using a hybrid model," *IEEE Transaction on Magnetics*, vol.32, no.5, pp. 4308-4310, Sept. 1996.

[37] G. H. Jang, and J. W. Yoon, "Torque and unbalanced magnetic force in a rotational unsymmetric brushless DC motors," *IEEE Transaction on Magnetics*, vol.32, no. 5, pp. 5157-5159, Sept. 1996.

[38] C. S. Koh, "New cogging torque reduction method for brushless permanent magnet motors," *IEEE Transaction on Magnetics*, vol. 39, no. 6, Nov. 2003.

[39] M. F. Momen, *Thermal analysis and design of switched reluctance and brushless permanent magnet machines*, Dissertation presented to the graduate faculty of the University of Akron, 2004.

[40] H. Cho, H. R. Cho, H. Lee, "Effect of pole to slot number ratio on back-emf constant of BLDC motor with non-overlapping stator winding," *International Electric Machines & Drives Conf.*, pp. 54-56, 1999.

[41] H. C. Lovatt and J. M. Stephenson, "Influence of the number of poles per-phase in switched reluctance motors," *IEE Proc*. of *Electric Power Appl.*, pt. B, vol. 139, no. 4, pp. 307-314, July 1992.

[42] K. Han, C. Han-Sam, C. Dong-Hyeok, J. Hyun-Kyo, "Optimal Core Shape Design for Cogging Torque Reduction of Brushless DC Motor Using Genetic Algorithm," *IEEE Transactions on Magnetics*, vol. 36, no. 4, pp. 1927-1931, July 2000.

[43] D. E. Cameron, J. H. Lang, S. D. Umans, "The origin of acoustic noise in variable-reluctance motors," *IEEE Trans. on Industry Applications*, vol. 28, no. 6, pp.1250-1255, Nov./Dec. 1992.

[44] R. Belmans, K. J. Binns, W. Geysen and A. Vandenput, *Vibrations and audible noise in alternating current machines*, Kluwer Academic Publishers, NATO ASI series, 1988.

[45] P. Vijayraghavan and R. Krishnan, “Noise in electric machines: A review,” *IEEE Transactions on Industry Applications*, vol. 35, no.5, pp. 1007-13, Sept.-Oct., 1999.

[46] A. J. Ellison and S. J. Yang, “Natural frequencies of stators of small electric machines,” *IEE Proc. of Elect. Power Contr. and Science*, v. 118, n. 1, pp. 185-190, 1971.

[47] R. S. Girgis, S. P. Verma, “Methods for Accurate Determination of Resonant Frequencies and Vibration Behavior of Stators of Electric Machines,” *IEE Proc.*, vol. 128, Pt. B, no. 1, pp- 1-11, January 1981.

[48] R. K. Singal, K. Williams and S. P. Verma, “Vibration behavior of stators of electrical machines, Part II: Experimental study,” *Journal of Sound and Vibration*, vol. 115, no. 1, pp. 13-23, 1987.

[49] S. C. Chang, “Electrical noise in small electrical motors,” *IEE-EMD Conference Publication*, no. 444, pp. 391-395, September, 1997.

[50] Z. Q. Zhu and Y. X. Chen, “On the calculation of acoustic power radiated by an electrical machine,” *IEE Conference Publication on Electrical Machines and Drives*, no. 282, pp. 118-121, 1987.

[51] S. Timoshenko and H. MacCullough, *Elements of strength of materials* D. Van Nostrand Company, 1949.

[52] S. J. Yang, *Low-Noise Electrical Motors*, Clarendon Press, Oxford, 1981.

[53] Nathan Ida and J. P. A. Bastos, *Electromagnetics and calculation of fields*, New York: Springer, 1997.

[54] M. N. Anwar, I. Husain, A. V. Radun, “A comprehensive design methodology for switched reluctance machines,” *IEEE Transaction on Industrial Applications*, vol. 36, no. 6, pp. 1684-1692, Nov. 2001.

[55] Magsoft Corp., *User’s Guide, Flux2D*, 1998.

APPENDICES

APPENDIX A

GLOSSARY OF SYMBOLS

Machine Geometries:

α_{lmrg}, α_{routrg}, α_{lmds}	Ratios of l_m/R_g, R_{out}/R_g, and l_m/d_s respectively.
α_{yrys}, α_{sd}	Ratios of y_r/y_s and $(d_{1+} d_2)/w_{tb}$, respectively.
A_{slot}	Copper area for each coil side (m^2).
A_{pe}, A_{pm}	Electrical and mechanical area product (m^4), respectively.
g	Airgap between stator and rotor poles in face to face (m).
y_s, y_r	Stator and rotor pole height (m), respectively.
L_{stk}	Stator stack length (m).
N_p	Number of rotor poles.
N_s	Number of stator slots.
N_{ph}, N_{rep}	Number of phases and repetitions, respectively.
n_{ser}, n_{par}	Number of series and parallel paths in the winding.
R_{shaft}, R_{gs}	Shaft radius and radius to stator tooth tip (m), respectively.
R_g, R_{sy}	Radius to rotor pole tips and the radius to stator yoke (m), respectively.
R_{out}, R_m	Outer and mean radius of stator yoke (m), respectively.
τ_c, τ_p	Stator coil pitch and rotor pole pitch (rad), respectively.
Stf	Stator stacking factor.

w_s, w_{sb}, w_{tb} — Slot width at airgap end and yoke end ,and thickness of the tooth (m), respectively.

d_s, w_{bi} — Radial depth of slot and stator back iron (m), respectively.

W_p — Total weight of all the stator poles (kg).

W_y — Total weight of the stator yoke (kg).

W_w — Total weight of the phase windings (kg).

W_i — Total weight of the copper winding insulation (kg).

W_t — Total weight of the machine (kg).

W_{rotor} — Total weight of the rotor (kg).

Machine Parameters:

J_{rms} — Rms current density (A/m^2).

L_d, L_q — *d*- and *q*- axes phase inductance (henry), respectively.

P_{max} — Maximum rated power (watt).

R_{ph} — Resistance of phase winding (ohm).

τ_{rated}, τ_{mean} — Rated output torque and mean output torque (N.m), respectively.

ω — Instantaneous rotor angular speed (rad/sec).

ω_b — Base speed of the machine (rad/sec).

ω_{mrated} — Maximum rated speed of the machine (rad/sec).

η — Core loss dependent parameter of the machine.

V_{dc} — Dc bus voltage (Volt).

Material Properties:

B_{sat} — Saturation flux density of the machine material (Tesla).

E — Young's modulus of elasticity of stator material (N/m^2).

μ_r	Relative permeability of the machine material.
μ_0	Absolute permeability of the air = $4.\pi.10^{-7}$.
Φ_g	Air gap flux (weber).
ρ_m, ρ_s	Density of rotor and stator material (kg/m^3), respectively.
ρ_c	Density of copper wire used in the windings (kg/m^3).
ρ_{res}	Resistivity of the copper (ohm-m).
$T_{e\rho}$	Maximum rotor torque density (N.m/m^3).
T_s	Hoop stress of rotor material (N/m^2).

Various Factors:

K_e	Back-emf constant (V/rad/sec).
K_{cu}	Copper factor = A_{cu}/A_{wn}.
Pf	Power factor.
$f_{m(=1)}$	Circumferential mode frequency for mode $m = 1$.
$f_{m(=2)}$	Circumferential mode frequency for mode $m = 2$.

Vibration Parameters:

σ_r	Radial component of stress on the stator (N/m^2).
σ_t	Tangential component of stress on the stator (N/m^2).
v	Poisson's ratio for steel material used in stator lamination.
P_s	Sound power radiated (watt),
σ_{rel}	Relative sound intensity = $k^2/(1+k^2)$,
c	Traveling speed of sound in the medium (m/s).

P_{sref}	Reference of sound power level (10^{-12} watt).
f_{exc}	Excitation frequencies of the magnetic radial force (Hz) = $n.f_p$.
n	Harmonic number = 1, 2, 3, …. ….., n.
K	Equivalent stiffness.
M	Equivalent mass.
m	Circumferential mode number.

(All the units are in MKS standard.)

APPENDIX B

SEVERAL WINDING TOPOLOGIES

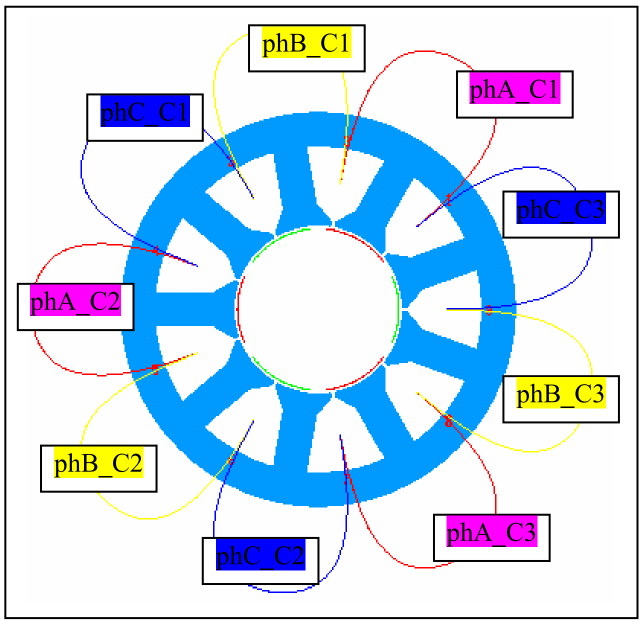

1. Concentrated winding (double layer) in a 9-slot/6-pole PMSM.

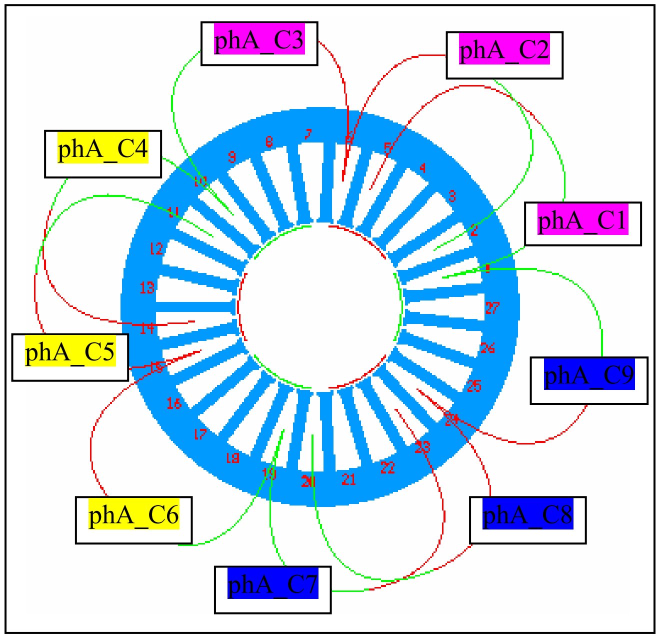

2. Distributed winding (double layer) in a 27-slot/6-pole PMSM showing 1-phase only.

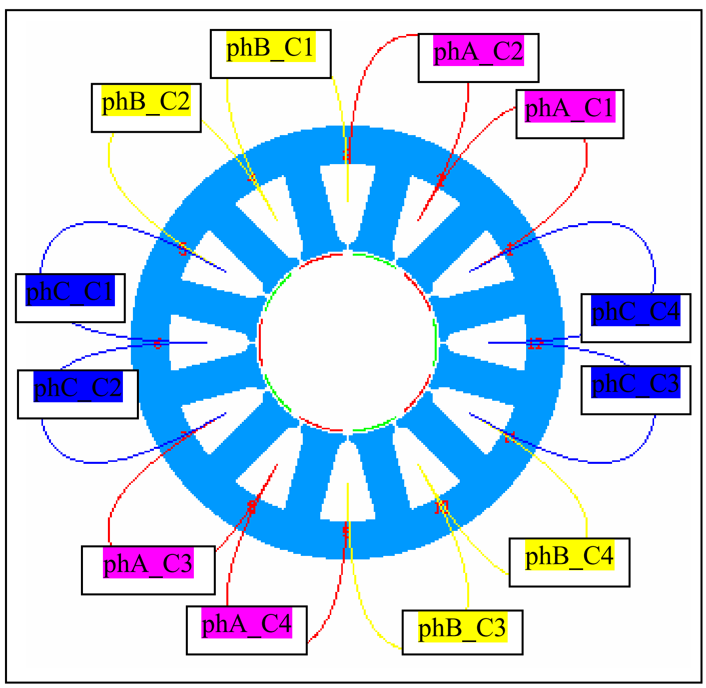

3. Modular winding (double layer) in a 12-slot/10-pole PMSM.

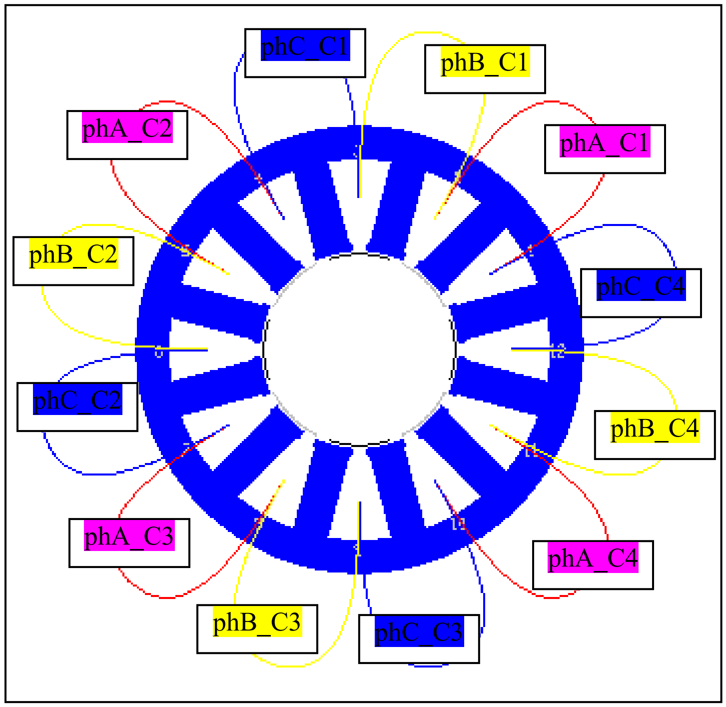

4. Concentrated winding (double layer) in a 12-slot/8-pole PMSM

APPENDIX C

CANCELLATION OF EVEN HARMONICS IN TORQUE FOR A 3-PHASE PMSM

The 3-phase BEMFs with 5th, 7th, 11th, and 13th order harmonics and the ideal currents with fundamental component only with a phase advance angle γ is given as

$$e_a = E_1 \cos(\omega t) + E_5 \cos(5\omega t) + E_7 \cos(7\omega t) + E_{11} \cos(11\omega t) + E_{13} \cos(13\omega t)$$
$$i_a = I_1 \cos(\omega t - \gamma)$$

$$e_b = E_1 \cos(\omega t - \frac{2\pi}{3}) + E_5 \cos\{5(\omega t - \frac{2\pi}{3})\} + E_7 \cos\{7(\omega t - \frac{2\pi}{3})\} + E_{11} \cos\{11(\omega t - \frac{2\pi}{3})\} + E_{13} \cos\{13(\omega t - \frac{2\pi}{3})\}$$
$$i_b = I_1 \cos(\omega t - \gamma - \frac{2\pi}{3})$$
$$e_c = E_1 \cos(\omega t + \frac{2\pi}{3}) + E_5 \cos\{5(\omega t + \frac{2\pi}{3})\} + E_7 \cos\{7(\omega t + \frac{2\pi}{3})\} + E_{11} \cos\{11(\omega t + \frac{2\pi}{3})\} + E_{13} \cos\{13(\omega t + \frac{2\pi}{3})\}$$
$$i_c = I_1 \cos(\omega t - \gamma + \frac{2\pi}{3})$$

All three phases are assumed to be balanced and all harmonics of the same orders in all phases are of the same magnitudes. Also, the phase currents are assumed to be pure sinusoids for simplicity. The instantaneous torque is then given by

$$T_e = \frac{(e_a i_a + e_b i_b + e_c i_c)}{\omega_r}$$

Here,

$$e_a i_a = \frac{E_1 I_1}{2}[\cos(2\omega t - \gamma) + \cos\gamma] + \frac{E_5 I_1}{2}[\cos(6\omega t - \gamma) + \cos(4\omega t + \gamma)] + \frac{E_7 I_1}{2}[\cos(8\omega t - \gamma) + \cos(6\omega t + \gamma)] + \frac{E_{11} I_1}{2}[\cos(12\omega t - \gamma) + \cos(10\omega t + \gamma)] + \frac{E_{13} I_1}{2}[\cos(14\omega t - \gamma) + \cos(12\omega t + \gamma)]$$

$$e_b i_b = \frac{E_1 I_1}{2}[\cos(2\omega t - \gamma + \frac{2\pi}{3}) + \cos\gamma] + \frac{E_5 I_1}{2}[\cos(6\omega t - \gamma) + \cos(4\omega t + \gamma + \frac{2\pi}{3})] + \frac{E_7 I_1}{2}[\cos(8\omega t - \gamma - \frac{2\pi}{3}) + \cos(6\omega t + \gamma)] + \frac{E_{11} I_1}{2}[\cos(12\omega t - \gamma) + \cos(10\omega t + \gamma - \frac{2\pi}{3})] + \frac{E_{13} I_1}{2}[\cos(14\omega t - \gamma + \frac{2\pi}{3}) + \cos(12\omega t + \gamma)]$$

$$e_c i_c = \frac{E_1 I_1}{2}[\cos(2\omega t - \gamma - \frac{2\pi}{3}) + \cos\gamma] + \frac{E_5 I_1}{2}[\cos(6\omega t - \gamma) + \cos(4\omega t + \gamma - \frac{2\pi}{3})] + \frac{E_7 I_1}{2}[\cos(8\omega t - \gamma + \frac{2\pi}{3}) + \cos(6\omega t + \gamma)] + \frac{E_{11} I_1}{2}[\cos(12\omega t - \gamma) + \cos(10\omega t + \gamma + \frac{2\pi}{3})] + \frac{E_{13} I_1}{2}[\cos(14\omega t - \gamma - \frac{2\pi}{3}) + \cos(12\omega t + \gamma)]$$

Therefore, the torque equation simplifies to

$$\begin{aligned} T_e = \frac{1}{\omega_r}[&\frac{E_1 I_1}{2}\{\cos(2\omega t - \gamma) + \cos(2\omega t - \gamma + \frac{2\pi}{3}) + \cos(2\omega t - \gamma - \frac{2\pi}{3})\} + \frac{3E_1 I_1}{2}\cos\gamma + \\ &\frac{E_5 I_1}{2}\{\cos(4\omega t + \gamma) + \cos(4\omega t + \gamma + \frac{2\pi}{3}) + \cos(4\omega t + \gamma - \frac{2\pi}{3})\} + \frac{3E_5 I_1}{2}\cos(6\omega t - \gamma) + \\ &\frac{E_7 I_1}{2}\{\cos(8\omega t - \gamma) + \cos(8\omega t - \gamma - \frac{2\pi}{3}) + \cos(8\omega t - \gamma + \frac{2\pi}{3})\} + \frac{3E_7 I_1}{2}\cos(6\omega t + \gamma) + \\ &\frac{E_{11} I_1}{2}\{\cos(10\omega t + \gamma) + \cos(10\omega t + \gamma - \frac{2\pi}{3}) + \cos(10\omega t + \gamma + \frac{2\pi}{3})\} + \frac{3E_{11} I_1}{2}\cos(12\omega t - \gamma) + \\ &\frac{E_{13} I_1}{2}\{\cos(14\omega t - \gamma) + \cos(14\omega t - \gamma + \frac{2\pi}{3}) + \cos(14\omega t - \gamma - \frac{2\pi}{3})\} + \frac{3E_{13} I_1}{2}\cos(12\omega t + \gamma) \\ = &\frac{3E_1 I_1}{2\omega_r}\cos\gamma + \frac{3E_5 I_1}{2\omega_r}\cos(6\omega t - \gamma) + \frac{3E_7 I_1}{2\omega_r}\cos(6\omega t + \gamma) + \frac{3E_{11} I_1}{2\omega_r}\cos(12\omega t - \gamma) + \\ &\frac{3E_{13} I_1}{2\omega_r}\cos(12\omega t + \gamma) \end{aligned}$$

For simplicity the torque is composed of the following components

T_e = DC or average torque + 6th order component + 12th order component + integer multiple of 6th order components.

Here, the average torque is given by $\frac{3E_1 I_1}{2\omega_r}\cos\gamma$, the 6th order components composed of contribution from 5th and 7th order harmonics of BEMF when interacting with fundamental component of current. These can also be as a result of current harmonics interacting the same way with fundamentals of BEMF. Similarly the 12th and other higher order torque ripples (multiple of 6th order) can be explained. Also, it is clearly seen that the even harmonics of 2nd, 4th, 8th, 10th, 14th etc. are cancelled out in a balanced 3-phase system.

APPENDIX D

TYPICAL B-H CHARACTERISTICS OF LAMINATION STEEL

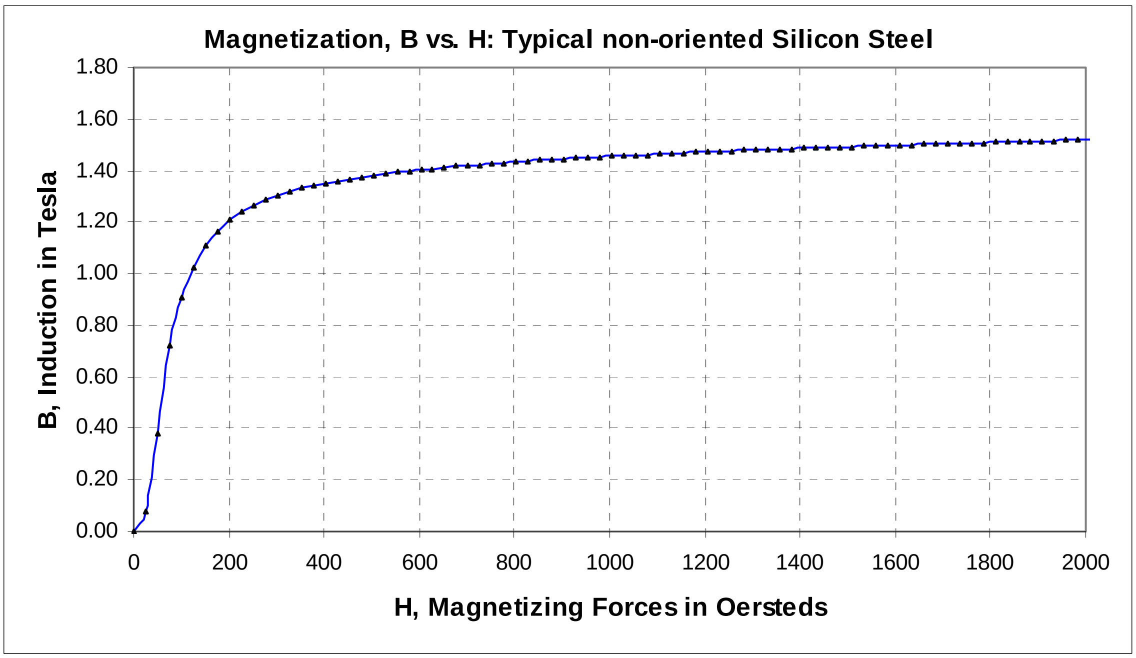

APPENDIX E

DIFFERENTIAL EQUATION OF VIBRATION MODEL

From static equilibrium we have

$$\frac{d\sigma_r}{dr} + \frac{\sigma_r - \sigma_t}{r} = 0 \tag{D1}$$

As $\varepsilon_x = 0$, $\sigma_x = \nu(\sigma_r + \sigma_t)$

$$\varepsilon_r = \frac{1}{E}(\sigma_r - \nu\sigma_t - \nu\sigma_x) = \frac{1}{E}[\sigma_r - \nu\sigma_t - \nu^2(\sigma_r + \sigma_t)] = \frac{dx}{dr} \tag{D2}$$

$$\varepsilon_t = \frac{1}{E}(-\nu\sigma_r + \sigma_t - \nu\sigma_x) = \frac{1}{E}[-\nu\sigma_r + \sigma_t - \nu^2(\sigma_r + \sigma_t)] = \frac{x}{r} \tag{D3}$$

From (D2) and (D3) we have

$$(1-\nu)\sigma_r - \nu\sigma_t = \frac{E}{(1+\nu)}\frac{dx}{dr} \tag{D4}$$

$$-\nu\sigma_r + (1-\nu)\sigma_t = \frac{E}{(1+\nu)}\frac{x}{r} \tag{D5}$$

Solving the above equations for σ_r and σ_t

$$\sigma_r = \frac{E}{(1+\nu)(1-2\nu)}[(1-\nu)\frac{dx}{dr} + \nu\frac{x}{r}]$$, and

$$\sigma_t = \frac{E}{(1+\nu)(1-2\nu)}[\nu\frac{dx}{dr} + (1-\nu)\frac{x}{r}]$$

Therefore,

$$\frac{d\sigma_r}{dr} = \frac{E(1-\nu)}{(1+\nu)(1-2\nu)}\frac{d^2x}{dr^2} + \frac{E\nu}{r(1+\nu)(1-2\nu)}\frac{dx}{dr} - \frac{E\nu}{r^2(1+\nu)(1-2\nu)}x \ , \tag{D6}$$

and

$$\frac{\sigma_r - \sigma_t}{r} = \frac{E}{r(1+\nu)}\frac{dx}{dr} - \frac{E}{r^2(1+\nu)}x \tag{D7}$$

Combining (D6) and (D7) in (D1)

$$\frac{E(1-\nu)}{(1+\nu)(1-2\nu)}.\frac{d^2x}{dr^2} + \frac{E(\nu+1-2\nu)}{r(1+\nu)(1-2\nu)}.\frac{dx}{dr} - \frac{E(1-\nu)}{(1+\nu)(1-2\nu)}.\frac{x}{r^2} = 0$$

Or,

$$\frac{d^2x}{dr^2} + \frac{1}{r}.\frac{dx}{dr} - \frac{1}{r^2}.x = 0 \tag{D8}$$

Again, the solution to the above differential equation (D8) can be written as

$$x = A_1 r + \frac{A_2}{r}$$

The constants are determined using the boundary conditions

$$\sigma_r |_{R_i} = -P_i = \frac{E}{(1+\nu)(1-2\nu)}[A_1 - (1-2\nu)\frac{A_2}{R_i^2}] \text{ , and}$$

$$\sigma_r |_{R_o} = -P_o = \frac{E}{(1+\nu)(1-2\nu)}[A_1 - (1-2\nu)\frac{A_2}{R_o^2}]$$

The final form of expressions for A_1 and A_2 in terms of known quantities is as follows

$$A_1 = \frac{(1+\nu).(1-2\nu)}{E}.\frac{P_i.R_i^2}{(R_o^2 - R_i^2)} \quad \text{and} \quad A_2 = \frac{(1+\nu)}{E}.\frac{P_i.R_i^2.R_o^2}{(R_o^2 - R_i^2)}$$

APPENDIX F

SOUND POWER LEVELS IN dB FOR SOME COMMON NOISE SOURCES

Noise Sources	**Sound Level (dB)**
Threshold of hearing	15
Whispering sound	30
Rustling leaves, soft music	45
Normal conversation	60
Average radio, vacuum cleaner	75
Inside acoustically insulated tractor cab	85
Tractor, farm equipment, power saw	100

APPENDIX G

SCHEMATICS OF A TYPICAL ELECTRIC POWER STEERING SYSTEM